UNIVERSITÀ DEGLI STUDI
DI TRENTO

DEPARTMENT OF INFORMATION ENGINEERING AND COMPUTER SCIENCE
ICT International Doctoral School

Advanced Methods for the Analysis of Radar Sounder Data Acquired at the Ice Sheets

Ana-Maria Ilisei

Advisor:

Prof. Lorenzo Bruzzone

Università degli Studi di Trento

April 2016

To my guides

Abstract

The World Climate Research Programme (WCRP) has recently reconfirmed the importance of a better understanding of the Cryosphere for advancing the analysis, modeling and prediction of climate change and its impact on the environment and society. One of the most complete collection of information about the ice sheets and glaciated areas is contained in the data (radargrams) acquired by Radar Sounder (RS) instruments. The need to better understand the structure of the ice sheets and the availability of enourmous quantities of radargrams call for the development of automatic techniques for an efficient extraction of information from RS data. This topic has been only marginally addressed in the literature. Thus, in this thesis we address this challenge by contributing with four novel automatic techniques for the analysis of radargrams acquired at the ice sheets.

The first contribution of this thesis presents a system for the automatic classification of ice subsurface targets in RS data. The core of the system is represented by the extraction of a set of features for target discrimination. The features are based on both the specific statistical properties of the RS signal and the spatial distribution of the ice subsurface targets. The second contribution is an unsupervised model-based technique for the automatic detection and property estimation of ice subsurface targets. This is done by using the parameters of the RS system combined with the output of an automatic image segmentation algorithm. The third contribution presents an automatic technique for the local 3D reconstruction of the ice sheet. It is based on the use of RS and altimeter (ALT) data, and relies on the use of a geostatistical interpolation method and on several statistical measures for validating the interpolation results and the quality of interpolation. The fourth contribution presents a technique for the automatic estimation of radar power losses in ice as a continuous non-linear function of depth, by using RS and ice core data. The technique relies on the detection of ice layers in the RS data, the computation of their reflectivity from the ice core data and the use of the radar equation for loss estimation. Qualitative and quantitative experimental results obtained on real RS data confirm the effectiveness of the first three techniques. Also, preliminary results have been obtained by applying the fourth technique to real RS and ice core data acquired in Greenland.

Due to their advantages over the traditional manual approach, e.g., efficiency, objectivity, possibility of jointly analyzing multisensor data (e.g., RS, ALT), the proposed methods can support the scientific community to enhance the data usage for a better modeling and understanding of the ice sheets. Moreover, they will become even more important in the near future, since the volume of data is expected to grow from the increase in airborne and possible Earth Observation spaceborne RS missions.

Keywords: Radar sounder, remote sensing, cryosphere, ice subsurface target identification, feature extraction, classification, interpolation, multisensor data processing.

Contents

List of Figures

List of Tables

List of Abbreviations

2WTT	two way travel time
AA	Average accuracy
ALT	Altimeter
APA	Average producer accuracy
AUA	Average user accuracy
bs	Binsize
bw	Binwidth
cpus	Computers
CReSIS	Center for Remote Sensing of Ice Sheets
DEM	Digital Elevation Model
DEP	Dielectric permittivity profile
EFZ	Echo-Free Zone
EO	Earth Observation
ESA	European Space Agency
GLACIES	GLACiers and Icy Environments Sounding
GLAS	Geoscience Laser Altimeter System
GPR	Ground Penetrating Radar
GPS	Global Positioning System
HGC	High gain channel
HiCARS	High CApability Radar Sounder
JUICE	JUpiter ICy moon Explorer
KL	Kullback-Leibler distance
LGC	Low gain channel
LRS	Lunar Radar Sounder
MARSIS	Mars Advanced Radar for Subsurface and Ionosphere Sounding
MCoRDS	MultiChannel Coherent Radar Depth Sounder
MEO	Mars Express Orbiter
MF	Medium Frequency

MIMOSA	Mapping of antarctic Ice and MOnitoring of SubArctic
MLE	Maximum Likelihood Estimation
MRO	Mars Reconnaissance Orbiter
MVDR	Minimum variance distortionless response
NASA	National Aeronautics and Space Administration
NN	Neural Network
OA	Overall accuracy
OAA	One against all
OAO	One against one
OK	Ordinary Kriging
PA	Producer accuracy
pdf	Probability density function
POLARIS	POLarimetric Airborne Radar Ice Sounder
RADAR	RAdio Detection and Ranging
RAR	Real Aperture Radar
RBF	Radial Basis Function
RCS	Radar cross-section
RIME	Radar for Icy Moon Exploration
RMSH	Root mean square height
RS	Radar Sounder
SAR	Synthetic Aperture Radar
SHARAD	SHAllow RADar
STDEV	Standard deviation
SV	Support Vector
SVA	Spatial variability analysis
SVM	Support Vector Machine
TO	Twin Otter
UA	User accuracy
UHF	Ultra High Frequency
WCRP	World Climate Research Programme
wpl	Waveform playlist

List of Symbols

f_c	Central frequency
B_w	Bandwidth
G	Antenna gain
Z_{st}	Range sensor-target
χ	RCS
c	Speed of light in free space
Λ	Two way travel time (2WTT)
P_{rx}	Received power
P_{tx}	Transmitted power
λ	Wavelength
L	One way power loss
σ_h	Root mean square height
τ	Pulse duration
A_{tx}	Amplitude of the transmitted radar pulse
ϕ_{tx}	Phase of the transmitted radar pulse
ρ_z	Range resolution
E_{tx}	Energy of the transmitted pulse
ρ_z^{RS}	RS range resolution with pulse compression
k_t	Windowing factor
$\delta_x^{RS,RAR}$	Azimuth resolution of a real aperture radar sounder
H	Platform height
l_x	Antenna length in the azimuth direction
l_s	Synthetic antenna aperture
$\delta_x^{RS,SAR}$	RS along-track resolution with SAR processing
δ_x^{RS,SAR^f}	RS along-track resolution with focused SAR processing
$\delta_x^{RS,SAR^{uf}}$	RS along-track resolution with unfocused SAR processing
$\delta_y^{RS,Bl}$	RS resolution in the across-track direction in the beam-limited case
l_y	Antenna length in the across-track direction

$\delta_y^{RS,Pl}$	RS resolution in the across-track direction in the pulse-limited case
$\delta_y^{RS,Fl}$	RS resolution in the across-track direction in the Fresnel-limited case
DF	Diameter of the first Fresnel zone
BRP	Bedrock returned power
R_{pdf}	Rayleigh pdf
N_{pdf}	Nakagami pdf
K_{pdf}	K pdf
G_{pdf}	Gamma pdf
θ	Vector of parameters of a theoretical model
I	Intensity domain
A	Amplitude domain
$KL(\mathcal{H}, \mathcal{M})$	Kullbak-Leibler distance between two pdfs $\mathcal{H}$ and $\mathcal{M}$
$\mathcal{H}$	Real histogram
$\mathcal{M}$	Theoretical model pdf
R_{ss}	Subsurface region of a radargram containing returns from all target classes
R_{noise}	Subsurface region of a radargram containing only noise measurements
θ_{best}	Vector of parameters of the best fitting theoretical model
$W_z \times W_x$	Sliding window size in the range and azimuth directions
Ent	Entropy feature
$Q\{\cdot\}$	Quantization operation
n_q	Number of quantization levels
$\wp(a)$	Probability of appearance of a
$\mathrm{KL}_{R_{ss}}$	KL distance feature/map of the subsurface region
$Dist_z$	Distance feature in number of pixels from the surface to the subsurface targets in the range direction
$surf$	Detected surface samples in the radargram
Rel	Relational feature
KL_{bin}	Binary version of the $\mathrm{KL}_{R_{ss}}$ map
$\mu_{\mathrm{KL}_{R_{noise}}}$	Mean value of the $\mathrm{KL}_{R_{noise}}$ map
$\mathrm{KL}_{R_{noise}}$	KL distance of the R_{noise} region
thr_{KL}	User defined value for thresholding the $\mathrm{KL}_{R_{ss}}$ map
t'	Generic trace of a radargram
n_Ψ	Number of training (cross-validation) samples
$\mathbf{v}$	Feature vector
κ_i	Class label associated to sample i

$\pounds_i$	Lagrange multiplier of the i-th training sample
ς	Error penalization (cost) term
$\mathcal{K}(\cdot)$	Kernel function
$\mathcal{D}$	SVM decision boundary
b	Bias term of SVM
n_T	Number of traces/columns of the radargram
n_S	Number of samples/rows of the radargram
τ_{ps}	Duration of the pulse used for shallow sounding
τ_{pd}	Duration of the pulse used for deep sounding
N^{tiles}	Number of vertical tiles of the radargram
N_{Ψ}^{tiles}	Number of tiles used in the SVM training (cross-validation) phase
ϑ	Gamma parameter of the RBF kernel
ϱ	Average distance between each pair of classes
ς_{Ω}	Cost for obtaining the highest overall classification accuracy on the test samples
ϑ_{Ω}	Gamma parameter of the RBF kernel that provides the highest overall classification accuracy on the test samples
kf	Number of folds used in the cross-validation
N_{Ω}^{tiles}	Number of tiles used in the SVM test phase
n_T^{tile}	Number of traces per tile
n_{Ω}	Number of test samples
$E\{\cdot\}$	Expectation operation
$\aleph(\cdot)$	Gamma function
$B_{\beta_K-1}(\cdot)$	Modified Bessel function of the second kind of order $\beta_K - 1$
$\ln(a)$	Natural logarithm of a
$\Xi(\cdot)$	Di-gamma function
t_{nbr}	Trace with no bedrock returns
$thick_{layers}$	Layer thickness zone in the radargram
$thick_{ice}$	Ice thickness zone in the radargram
$thick_{bedrock}$	Bedrock thickness zone in the radargram
d_{ss}	Length of the pixel in the range direction in the subsurface region
f_r	Range sampling frequency of the RS
$last_{layers}$	Last return of the layered scattering area
$first_{bedrock}$	First returns of the bedrock scattering area
$last_{bedrock}$	Last returns of the bedrock scattering area
KL_{layers}	Binary version of the KL map highlighting only the ice layer area

$\mathrm{KL}_{bedrock}$	Binary version of the KL map highlighting only the bedrock area
d_x^{RS}	Spacing between two adjacent RS measurements in the azimuth direction
d_y^{RS}	Spacing between two adjacent RS flightlines/tracks
δ^{ALT}	Horizontal resolution of ALT data
d^{ALT}	Spacing between two adjacent ALT measurements
δ_z^{ALT}	Vertical resolution of ALT data
x_0	Coordinates of a query sample
N_0	Number of neighbors of query sample at coordinate x_0
$e(x_n)$	Random variable e at coordinate x_n
$\hat{\gamma}(\mathbf{h})$	Empirical semivariogram
$\mathbf{h}$	Vector of point pair distances h_k
$\bar{k}$	Maximum number of bins of the empirical semivariogram
γ^{Can}	Candidate semivariogram model
γ^{Sph}	Spherical model of the empirical semivariogram
γ^{Exp}	Exponential model of the empirical semivariogram
γ^{Gau}	Gaussian model of the empirical semivariogram
γ^{Lin}	Linear model of the empirical semivariogram
R^2	R^2 indicator
$\gamma^*(\mathbf{h};\tilde{\theta})$	Empirical semivariogram best fitting model with the associated vector of parameters
$u(x_0)$	Uncertainty value at query sample coordinate x_0
e_{N_0}	Vector of N_0 observed values surrounding x_0
1_{N_0}	Column vector of N_0 ones
c_0, V_0	Elements of the full covariance matrix in x_0
C_0	Full covariance matrix in x_0
$\mathcal{C}(\mathbf{h})$	Covariogram
P	Number of parameter sets considered in the OK method
$\mathbf{W}1, \mathbf{W}2, \mathbf{W}3, \mathbf{W}4, \mathbf{W}5$	Weighting functions
s^*	Most reliable scale for interpolation
s_0^{RS}	Original scale of the RS data
S^{RS}	Ice surface elevation extracted from the RS data
B^{RS}	Bedrock elevation extracted from the RS data
s_0^{ALT}	Original scale of the ALT data
$\mathbf{S}^{ALT}$	Ice surface elevation map from the ALT data
J	Number of scales for interpolation
s_j	Scale for interpolation

$p^{*\mathbf{S}}$	Best OK parameter set for interpolating the surface samples
$\mathbf{S}^{RS}_{p^{*\mathbf{S}}}(s^*)$	Ice surface elevation map obtained with the best OK parameter set at the most reliable scale
$\mathbf{U}^{\mathbf{S}}_{p^{*\mathbf{S}}}(s^*)$	Uncertainty map of the surface obtained with the best OK parameter set at the most reliable scale
$\mathbf{D}$	Absolute error map
$p^{*\mathbf{B}}$	Best OK parameter set for interpolating the bedrock samples
$\mathbf{B}^{RS}_{p^{*\mathbf{B}}}(s^*)$	Bedrock elevation map obtained with the best OK parameter set at the most reliable scale
$\mathbf{U}^{\mathbf{B}}_{p^{*\mathbf{B}}}(s^*)$	Uncertainty map of the bedrock obtained with the best OK parameter set at the most reliable scale
$\Delta^{RS}(s^*)$	Ice thickness map at the most reliable scale
ρ	Range of the semivariogram
ξ	Sill of the semivariogram
η	Nugget of the semivariogram
$\flat$	Slope of the linear model of the semivariogram
t^c	Ice core position/trace
P_k	Received power from layer k
Z_k	Depth of layer k
ε_k	Dielectric permittivity at layer k
L_k	One way power loss at layer k
Γ_k	Reflectivity of the layer k
$\varepsilon_{k^-}, \varepsilon_{k^+}$	Dielectric permittivities before and after layer k
Υ_s	Transmission coefficient of the surface
ρ_s	Reflection reduction due to surface roughness
Γ_s	Reflectivity of the surface
P_s	Ice surface power
$\mathcal{L}$	One way power loss as a continuous function of depth
K	Number of continuous specular layers visible in the radargram
LC	Correlation length
Φ	Phase variation due to surface roughness
δ_z^{DEP}	Vertical resolution of the DEP profile

Introduction

This Chapter introduces the PhD thesis work. In particular, it presents the context in which Radar Sounders (RS) are employed and an overview of the existing RS systems for ice subsurface sensing. Afterwards, it describes the challenges related to the analysis of RS data. This allows us to state the aim of the thesis and to highlight its novel contributions. At the end of the chapter, the structure of the whole document is outlined.

Background and motivation

The World Climate Research Programme (WCRP) has recently reconfirmed the importance of a better understanding of the Cryosphere for advancing the analysis, modeling and prediction of climate change and its impact on the environment and society. In particular, "the potential for accelerated melting of various parts of the Greenland and Antarctic Ice Sheets, which could lead to several meters of sea-level rise, is a matter of great societal concern, and hence is a high priority research area" [2]. Therefore, the study of the ice subsurface is of crucial importance. In this thesis we aim to providing a contribution that can support the scientific community in the study of the ice sheet subsurface.

An effective way to study the ice subsurface on wide areas is by analysing the data (radargrams or echograms) acquired by Radar Sounder (RS) instruments [3]. RSs are airborne or satellite mounted nadir-looking active instruments that transmit a relatively low-frequency electromagnetic wave towards the surface and measure the reflected power at each coordinate of the platform. The nadir-looking configuration and the low frequencies employed by the RS ensure a deep penetration of the radar wave, e.g., even 4km in cold ice. The reflection of the radar wave takes place at interfaces in the subsurface created by thermal, dielectric and mechanical discontinuities. These interfaces, or targets for the radar, are highlighted in radargrams with increased amplitude in the direction of the wave propagation, at each position of the platform. Thus, at the end of the acquisition process, the radargram shows a representation of the cross-section of the subsurface. Moreover, the radargram provides information also on the position of the subsurface targets, which

can be estimated by using the time lapse between wave transmission and reception and the properties of the subsurface.

Regarding the coverage that can be achieved with a RS instrument, the wave deep penetation capability contributes to building the vertical coverage of the ice subsurface. The motion of the platform that carries the RS instrument contributes to building the ice surface coverage in the horizontal direction. Therefore, the amount of recorded RS data mainly depends on the RS instrument parameters and platform motion. So far, RSs for Earth Observation (EO) have been operated only during dedicated airborne campaigns at the Earth polar regions. Spaceborne RSs have been designed only for the observation of other planetary bodies, e.g., Moon (Lunar Radar Sounder (LRS) [4]), Mars (SHAllow RADar (SHARAD) [5], Mars Advanced Radar for Subsurface and Ionosphere Sounding (MARSIS) [6]), Jovian Icy Moons (Radar for Icy Moon Exploration (RIME) [7], currently under development). Although the design of Earth orbiting RS instruments is very challenging (mainly due to physical constraints and frequency allocation issues), the success of the existing planetary RS instruments have encouraged dedicated studies for defining EO RS missions from space (e.g., Mapping of antarctic Ice and MOnitoring of SubArctic (MIMOSA) [8], [9], GLACiers and Icy Environments Sounding (GLACIES) [10]). Once operative, such EO spacebased RS instruments will acquire data with homogeneous quality and uniform coverage, both spatially and temporally. This is not the case with the existing airborne RS data. Science requirements and technological constraints drive data acquisition strategy plans (e.g., location, coverage) and condition the data quality (e.g., maximum penetration, resolution). Therefore, the RS data acquired during different airborne campaigns have a limited coverage and heterogeneous quality. However, during the past decades a large amount of airborne RS data has been acquired and the volume of data is expected to increase during future airborne and forthcoming satellite EO RS missions.

Due to the coverage and different types of information that RS data convey (e.g., target reflected power, target position), the analysis of radargrams can lead to e great enhancement in the understanding of the ice sheets. However, during the past decades the analysis of RS data has been performed mainly by means of manual investigation and with a limited support of semi-automatic techniques.

Although it is still needed at least in a preliminary phase of the analysis, the traditional manual analysis of RS data features several problems.

- The manual analysis is time consuming, thus limiting the exploitation of data already available in archives and the efficient processing of incoming data.
- The manual analysis requires experts for the extraction of information from the data. This implies the use of experts as tools for extracting the information rather than

for interpreting the data. Moreover, the manual analysis is based on photointerpretation, which is an extremely subjective process. In fact, the same radargram can be interpreted in different ways by the same expert at different times. Also, different experts can interprete the same radargram in different ways. This makes the process dependent on several factors, resulting in different outputs given the same input.

– The manual analysis does not allow the integration, fusion and generally the joint analysis of data acquired with different sensors (e.g., altimeter (ALT) data, synthetic aperture radar (SAR) data). The aggregation of such data could highlight surface and subsurface features which are typically not visible in the RS data alone.

The abovementioned issues suggest that the manual analysis of RS data limits the scientific return that could be potentially achieved, thus leading to an insufficient understanding of the ice sheets.

Objectives and novel contributions of the thesis

The importance of studying the ice sheets, the availability of large archives of airborne RS data, the expected increase in data volume from both airborne and possible EO spaceborne RS missions, and the problems raised by the manual analysis call for the development of novel automatic techniques for the analysis of radargrams.

There are several advantages in using automatic techniques instead of the traditional manual analysis.

– The automatic techniques are fast since they rely on the use of computer power and repositories for the extraction of information, storage and retrieval of the obtained results. In this sense, one can take advantage of the latest technology, e.g., clusters of large-storage and high-power computers, for ensuring the resources needed for automatically proceesing the RS data. This is particularly important for a proper exploitation of the available data and an efficient processing of incoming data.

– The automatic techniques are objective. This ensures that by repeating the experiment with the same input, one will always obtain the same output. This is extremely important for a coherent and quantitative analysis of the ice subsurface.

– The automatic techniques allow the joint analysis of multisensor data acquired over the same region. This is particularly important for an efficient data usage for enhancing the knowledge of the ice subsurface.

So far, the development of automatic techniques for the analysis of ice sheet RS data has been addressed only to a limited extent by the scientific community. Such techniques

have been mostly designed for the analysis of the subsurface in radargrams acquired by terrestrial surface-mounted ground penetrating radars (GPR). Recently, increasing interest has been also shown in the development of automatic techniques for the analysis of the subsurface in planetary RS data acquired on Mars. The three mentioned types of radargrams (i.e., ice sheet RS data, terrestrial GPR data, and planetary RS data) have both common and different characteristics. The two main common properties of these radargrams are: i) they are acquired with the same nadir-looking geometry, and ii) they show measurements acquired in the subsurface. However, the instruments that acquire these radargrams are typically operated on different platforms (i.e., airborne, surface-mounted, satellite), have different parameters (e.g., central frequency, bandwidth) and are investigating different types of subsurface (i.e., ice sheet subsurface, ground subsurface, other planets subsurface). For these reasons, the coverage and resolution, both in the vertical and horizontal directions, and the patterns highlighted in the three types of data are different. Thus, the available automatic techniques for the analysis of terrestrial GPR and planetary RS data acquired on Mars cannot be directly applied to the analysis of the ice sheet subsurface acquired by airborne RS data. However, the successful application of automatic techniques to the analysis of GPR and planetary RS data encourage the development of such techniques specifically tuned to the peculiarities of RS ice sheet data. Indeed, automatic techniques can support a better usage of airborne RS data for a better understanding of the ice sheet subsurface.

In this thesis we provide four main novel contributions to fill the gap in the literature in the development of automatic techniques for the analysis of ice sheet RS data. Such techniques address three challenges of particular importance in the study of the ice sheets: i) *identification of ice sheet subsurface targets*, ii) *3D modeling of the ice sheet*, and iii) *understanding the interaction between the radar wave and the ice sheet*.

In the context of *identification of ice sheet subsurface targets*, we contribute with two automatic methods for the quantitative and large scale analysis of RS data:

1. A system for the automatic classification of ice subsurface targets in radar sounder data,

2. A model-based technique for the automatic detection of Earth continental ice subsurface targets in radar sounder data.

In the context of *3D modeling of the ice sheet*, we contribute with one method for the 3D reconstruction of the ice sheet:

3. An automatic technique for the local 3D reconstruction of the ice sheet by using radar sounder and altimeter data.

In the context of *understanding the interaction between the radar wave and the ice sheet*, we contribute with a technique for the estimation of power losses through ice:

4. Estimation of radar power losses in ice by using radar sounder and ice core data.

These techniques are briefly summarized below.

A system for the automatic classification of ice subsurface targets in RS data

The first contribution of the thesis addresses the problem of *identification of ice sheet subsurface targets*. In particular, the main objective of this contribution is the extraction from the radargrams of a set of features that can help an automatic classifier to accurately discriminate areas belonging to different subsurface classes, i.e., layers, noise and bedrock. The technique combines advanced image processing and machine learning techniques with the knowledge about the physical distribution of the targets and fundamentals on radar wave backscattering. The system is made up of two main components: i) feature extraction, and ii) automatic classification based on Support Vector Machine (SVM). In the first component, we propose a set of features that are able to model and correlate the backscattering properties of the radar signal with the spatial properties of the subsurface targets. The extraction of such features is done after a detailed study of the statistical properties of the radar signal and of the spatial distribution of the ice subsurface targets. The second component of the system uses the extracted features to perform the automatic classification of ice subsurface targets by using an SVM classifier. The main properties of the system are: a) robustness and/or adaptiveness to the heterogeneity of radargrams as a consequence of both the features used and the learning approach employed; b) capability to obtain objective quantitative results (i.e., exactly the same criteria are used for all radargrams, thus enabling the extraction of targets in a consistent and comparable way on all radargrams); and c) computational speed and efficiency due to the possibility of parallelizing the algorithm. For these reasons, the system is suitable for the analysis of the ice subsurface at large scale from radargrams acquired by RS sensors with different characteristics (e.g., central frequency, bandwidth).

A model-based technique for the automatic detection of Earth continental ice subsurface targets in radar sounder data

The second contribution of the thesis addresses again the problem of *ice subsurface target identification*. The aim of this contribution is the detection of the ice subsurface targets and the estimation of their properties (e.g., layered area thickness, bedrock scattering area). This is done in an unsupervised way by using the parameters of the RS acquisition system combined with the output of an automatic image segmentation algorithm. The

segmentation operation is applied to the radargrams after a preliminary processing phase aimed to emphasize the relevant subsurface targets. The segmentation criterion considers the radar signal backscattering properties and a model of the spatial distribution of the investigated targets that takes into account the effects of the wave propagation through the subsurface.

Automatic local 3D reconstruction of the ice sheet by using radar sounder and altimeter data

The third contribution of the thesis addresses the problem of *3D modeling of the ice sheet*. In particular, the aim of this contribution is the development of an automatic technique for the local 3D reconstruction of the ice sheets, by jointly using RS and ALT data. The technique aims to address two main challenges: i) the reconstruction should be performed by estimating 3D maps of the ice surface, ice/bedrock and ice thickness at the most reliable scale, derived automatically given the input RS and ALT data properties, and ii) the estimated maps should have the highest overall quality, i.e., the lowest overall uncertainty. To achieve this, the method relies on the ordinary kriging (OK) interpolation method and on the joint use of RS and ALT data for the optimization of the interpolation. The automatic identification of the most reliable scale for interpolation, the analysis and use of the uncertainty maps generated by the OK method, and the joint use of RS and ALT data are the main novel contributions of this work.

Estimation of Radar Power Losses in Ice by Using Radar Sounder and Ice Core Data

The fourth contribution of the thesis addresses the broad problem of *understanding the interaction between the radar wave and the ice sheet*. In particular, the objective of this contribution is the estimation of power losses through the ice as a continuous non-linear function of depth and location, rather than the estimation of ice power loss rate, as done in other works in the related literature. To this aim we use coincident RS and ice core data. The technique relies on the detection of layers in the radargram. The reflectivity of the layers is computed from the ice core data and is assumed constant along each layer. The ice losses at each layer depth are estimated by inverting the radar equation. Then, at each coordinate of the RS platform, the power losses through the ice column are estimated as a continuous non-linear function of depth by fitting a theoretical function to the losses estimated at the layer depths and extrapolating it to the bed. This results in a more reliable estimation of the power losses on wide areas, which is fundamental for a better understanding of the radar wave interaction with the ice subsurface and for a better modeling of the processes taking place within the ice sheet and at the basal interface (e.g., reduction of the uncertainties related to the boundary conditions).

Qualitative and quantitative experimental results obtained on real RS data acquired in Antarctica confirm the effectiveness of the methods described in the first three contributions. Also, preliminary results have been obtained by applying the method described in the fourth contribution to real RS and ice core data acquired in Greenland. Due to their advantages over the traditional manual approach, e.g., efficiency, objectivity, possibility of jointly analyzing multisensor data (i.e., RS, ALT, ice core), the proposed methods can support the scientific community to enhance the data usage for a better modeling and understanding of the ice sheet. Moreover, the proposed methods will become even more important in the near future, since the volume of data is expected to grow from the increase in airborne and possible EO spaceborne RS missions.

Structure of the thesis

This document is divided into 6 chapters. Chapter 1 presents fundamental concepts in radar and more specifically RS systems, which are needed for understanding the background notions of the thesis. Chapter 2 presents an overview of the State of the Art regarding the automatic analysis of radargrams. In particular, the literature on the identification of subsurface features, on the 3D reconstruction of the ice subsurface, and on the ice loss estimation are provided in Sec. 2.1, Sec. 2.2 and Sec. 2.3, respectively. In Chapter 3 and Chapter 4 we present two automatic techniques for the identification of ice sheet subsurface targets in radargrams, i.e., target classification and target detection, respectively. An automatic technique for the ice sheet 3D reconstruction by using RS and ALT data is presented in Chapter 5. Chapter 6 describes an automatic technique for the estimation of power losses through ice by fusing RS and ice core data. Each Chapter from 3 to 6 is made up of more sections, each presenting a detailed description of the methods used, experimental results obtained by applying the methods to real data acquired at the ice sheets and related conclusions. Finally, the conclusions of the thesis are drawn along with proposals for future research and developments.

Chapter 1

Fundamentals

This Chapter provides a description of fundamental concepts in radar with focus on specific aspects of RS systems, useful for understanding the thesis. First, the radar basic principles are given. Then, the acquisition process and geometry of RS is illustrated. Afterwards, the geometrical resolution of RS data and common signal processing techniques used for resolution enhancement are presented. Finally, some examples of RS systems are given.

1.1 Radar basic principles

The acronym "RADAR" stands for "RAdio Detection and Ranging". Indeed, radar instruments work by transmitting electromagnetic waves in the radio spectrum toward a target and are able to detect the presence and compute the range to the target. Moreover, they are able to measure the scattering properties of the targets, also called radar cross-section (RCS). Two of the main parameters of a radar system are the central frequency f_c, typically in the range between few MHz and tens of GHz, and the bandwidth B_w of the transmitted signal. These are design parameters of a radar system and depend on the type of radar (e.g., GPR, RS, SAR) and on the considered application (e.g., target detection, target characterisation). In the following, we illustrate general concepts of radar systems, which are related to the understanding of the thesis, i.e., i) the radar equation, and ii) the fundamentals of scattering and coherent nature of radar signals.

Radar equation

The simplest model of a radar system consists of the same antenna with gain G, both for transmission and reception (i.e., monostatic system) and a target at range Z_{st} with unknown RCS χ. By using this model, information about the range to the target Z_{st} is

obtained with the time-distance conversion equation, expressed as:

$$Z_{st} = \frac{c\Lambda}{2\sqrt{\varepsilon}}, \tag{1.1}$$

where c is the speed of light in free space, Λ is the time lapse between wave transmission and reception, or two way travel time (2WTT), and ε is the dielectric permittivity of the considered media. Also, one can retrieve partial information about χ, by inverting the radar equation, expressed by:

$$P_{rx} = P_{tx}\frac{\lambda^2 G^2 L^2}{(4\pi)^3 Z_{st}^4}\chi, \tag{1.2}$$

where P_{rx} is the power measured by the radar receiver, P_{tx} is the transmitted signal power, $\lambda = c/f_c$ is the wavelength, L is the one way power loss through the media. It is worth noting that (1.2) is a simplified form of the radar equation, which embodies the main parameters of the radar system. However, the radar equation can become more complex depending on the application and type of radar (e.g., subsurface radar, side-looking radar). Besides by using the radar equation, further information about χ can be retrieved by analysing the coherent nature of the radar signal.

Scattering and coherent nature of radar signals

The signals transmitted by modern radars are waveforms characterized by amplitude and phase. Their interaction with targets, i.e., scattering, changes both the amplitude and the phase of the signals. Therefore, the analysis of this interaction can provide information about the scattering properties of the target, i.e., χ.

The scattering is composed of a mix of specular and diffuse components, depending on the interface roughness in terms of root mean square height (RMSH) σ_h with respect to the wavelength λ. In particular, σ_h represents the vertical displacement of the surface with respect to its mean plane. For a smooth surface ($\sigma_h \ll \lambda$), the wave is entirely scattered in the specular direction. This situation, also called coherent scattering, is represented in Fig. 1.1(a). For a slightly rough surface ($\sigma_h < \lambda$) the scattering is characterized by a large specular component, and a diffused component with less power scattered in all directions. This situation, in which the wave starts losing coherency, is represented in Fig. 1.1(b). A very rough surface ($\sigma_h \gg \lambda$) scatters the wave diffusely in all directions. This situation, called incoherent scattering, is represented in Fig. 1.1(c). As it can be seen, the rougher the surface, the weaker are the specular and the stronger are the diffused components.

One of the main effects due to the coherent nature of the radar signal is the speckle. The radar resolution cell is usually larger than the wavelength (see Sec. 1.3 for RS data resolution), thus more scatterers are present in each cell. Each scatterer contributes to the signal received from a resolution cell with its own amplitude and phase. Such contributions

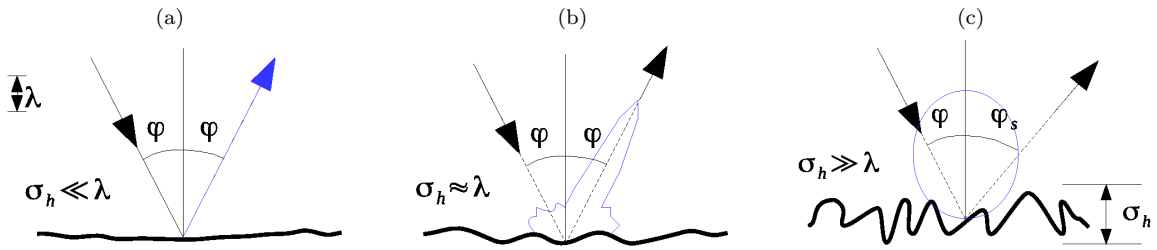

Figure 1.1: Surface scattering for (a) smooth surface, (b) slightly rough surface, and (c) very rough surface. In the figures φ is the angle of incidence and φ_s is the angle of the scattered wave.

sum up coherently, resulting in constructive and destructive interference, called speckle. This has a granular appearence in the radar data, similar to random noise. In reality, speckle is not random as it depends on the scatterers present in the scene. In the radar data, the speckle is normally treated as a noise-like quantity multiplying the underlying χ. Thus, the speckle is usually humpering the interpretation of the data. However, it can be reduced by means of multilooking techniques. Multilooking can be applied directly during acquisition of the data [11], or by averaging correlated samples, which in turn worsens the geometrical resolution by a factor equal to the number of looks.

The abovementioned principles are general to all types of radar systems. In the following we will focus only on RS systems, since they acquire ice subsurface data, which make the subject of the thesis.

1.2 Radar sounder acquisition geometry and process

Radar sounding is a well-known nonintrusive technique which allows the investigation of the structural and dielectric characteristics of the subsurface. RSs are nadir-looking radar systems, see Fig. 1.2, working at low frequencies, more precisely in the range of the frequency spectrum between few MHz to few hundreds of MHz (MF to UHF). These frequencies are particularly suitable for deep ice or desert subsurface sounding (e.g., as deep as 4km in cold ice) because of the transparency of these materials in this range [3]. In the following we will refer to the ice monitoring radar sounders, although the acquisition process is analogous for desert subsurface sounding.

As depicted in Fig. 1.2, the RS is mounted on a flying platform. At each position of the platform, the RS transmits a pulse with duration τ, amplitude A_{tx} and phase ϕ_{tx}, vertically (at nadir or in the range direction) towards the ice surface. The pulse travels from the sensor to the surface, penetrates the subsurface, is reflected by the ice subsurface targets and turns back through the ice and air to the sensor. During the two way prop-

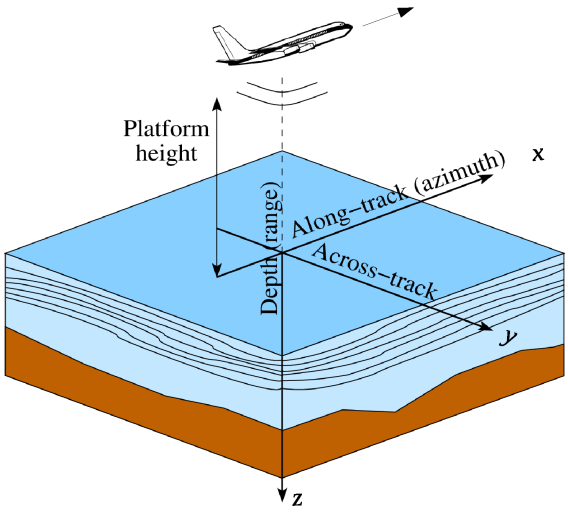

Figure 1.2: Acquisition geometry of a RS system.

agation (sensor-target-sensor), the pulse experiences geometric spherical losses both in air and ice, reflection or scatterring losses at the air/ice interface, reflection or scattering losses through ice, and reflection or scattering losses at the bedrock. The reflection or scattering takes place at interfaces in the subsurface created by thermal, dielectric and mechanical discontinuities. The reflected waves measured by the receiving antenna are recorded as complex signals (amplitude and phase) as a function of 2WTT. Such measurements are registered in the columns (or traces) of a 2D matrix, called radargram. Therefore, each trace of the radargram contains the information about the ice column below the platform. Successive traces are then generated by repeating this acquisition process at each platform position at determined time intervals, called pulse repetition intervals (PRI). The result is a radargram that represents the cross-section of the ice in terms of the wave received amplitude and phase for a given range position as a function of 2WTT (or distance) on the vertical axis, and as a function of the instrument along-track (or azimuth) position on the horizontal axis.

Due to the RS acquistion geometry and to the non-ideal directivity of the antenna, the received signals can also contain components coming from off-nadir directions at the same time with the subsurface nadir returns. These returns are called clutter. The amount of clutter depends on the antenna footprint width and on the surface characteristics. The wider the antenna footprint and the higher the surface topography, slope and/or roughness, the more relevant the effects of clutter. In the radargram, the clutter returns overlap on the returns coming from the subsurface, leading to partial or complete masking of the subsurface features. This can represent an issue for the interpretation of radar signals. In

the azimuth direction, the clutter can be reduced by using SAR techniques, whereas in the across-track direction, the clutter can be reduced by using suitable processing techniques, as explained in Sec. 1.3.

1.3 Geometrical resolution of radar rounder data

The geometrical resolution of a radar is its ability to distinguish between targets that are very close either in the range or in the along-track or across-track directions. In the following, we describe how the resolution of a RS system is computed in the three directions and additional signal processing techniques for resolution enhancement.

Range resolution

The range resolution ρ_z depends on the length of the transmitted pulse in time domain τ and on the dielectric properties of the media ε, as expressed by:

$$\rho_z = \frac{c\tau}{2\sqrt{\varepsilon}}. \tag{1.3}$$

The above equation states that in order to be resolved, two targets should be separated in the range direction by at least one-half the pulse length. Thus, the use of (1.3) implies that short pulses should be used in order to achieve better range resolution. However, the use of short pulses does not grant sufficient energy to detect small targets at long range. This is evident by looking at the equation of the transmitted pulse energy E_{tx}:

$$E_{tx} = P_{tx}\tau. \tag{1.4}$$

By decreasing τ, the power of the pulse should be increased in order to ensure sufficient energy. However, increasing the power in a very short time is not always technically possible. Therefore, in order to improve the range resolution and ensure sufficient energy, i.e., by keeping a relatively long pulse length, in most RSs range resolution is not achieved through the transmission of the shortest possible pulse, rather through the use of a chirp, i.e., a long pulse linearly modulated in frequency. In this case, thanks to range-compression techniques using matched filters [12], the vertical range resolution of RS can be calculated as:

$$\rho_z^{RS} = \frac{c}{2B_w\sqrt{\varepsilon}}k_t. \tag{1.5}$$

Therefore, ρ_z^{RS} depends on three main terms: the compressed signal bandwidth B_w, the properties of the media ε and the windowing coefficient k_t. As it can be inferred, the use of a large signal bandwidth can improve the range resolution of a radar system. However, depending on the application and frequency allocation limitations, there are constraints

on the bandwidth. For instance, the chosen central frequency along with the maximum data storage capacity impose limitations on the maximum possible signal bandwidth. ρ_z^{RS} also depends on the material in which the pulse is traveling. More precisely, the range resolution is always better in materials than in air, since $\varepsilon^{material} > \varepsilon^{air} = 1$ (e.g., $\varepsilon^{ice} = 3.15$). Furthermore, ρ_z^{RS} depends on the windowing coefficient k_t. The windowing is a signal processing technique applied to the compressed signal in order to suppress the sidelobe level generated through range-compression. As a result, the effective range resolution worsens by a factor $k_t > 1$ that depends on the applied windowing function (e.g., Hanning, Tuckey).

Along-track resolution

It is important first to make the distinction between a real aperture radar (RAR) system and a SAR system. In the case of a RAR system, the along-track resolution depends on the parameters of the system, whereas in the case of a SAR system, the along-track resolution is achieved by means of signal processing techniques. In more details, the azimuth resolution of a RAR sounder system $\delta_x^{RS,RAR}$ depends on the footprint of the main lobe of the radar beam on the ground in the flight direction, and is expressed by:

$$\delta_x^{RS,RAR} = \frac{\lambda H}{l_x}, \tag{1.6}$$

where H is the platform height with respect to the surface and l_x is the lenght of the antenna in the azimuth direction. The expression in (1.6) states that in order to be resolved, two targets in the azimuth direction should be spaced by at least the width of the antenna footprint in the flight direction, i.e., the real antenna azimuth aperture. Also, one can see that better azimuth resolution can be achieved by acquiring data at low altitude and using long antennas. However, in practical airborne and spaceborne missions, these requirements cannot be satisfied. Instead, the azimuth resolution can be considerably improved by processing the phase information of the complex signals with SAR techniques.

Fig. 1.3 shows the principle of SAR. SAR exploits the movement of the platform in the azimuth direction and the Doppler theory. A point target is illuminated by the SAR beam during a time interval that depends on the real antenna footprint and the velocity of the platform. During this time, which is called integration time, a synthetic antenna aperture l_s larger than the aperture of the real antenna is generated, i.e., $l_s > l_x$. Within the integration time, the SAR system records the phase history of the signal, by exploiting the Doppler shifts of the received complex signals. By processing this information, different targets can be resolved, even if they are located in the azimuth direction closer than the real azimuth aperture. For a RS system, the along-track resolution obtained with SAR

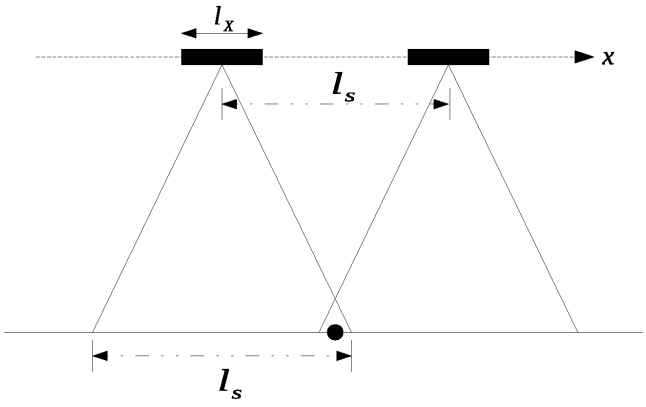

Figure 1.3: SAR principle. The target is illuminated during the time in which the real antenna travels a distance equal to l_s, which is the length of the synthetic antenna.

techniques is:

$$\delta_x^{RS,SAR} = \frac{\lambda H}{2l_s}. \tag{1.7}$$

The SAR Doppler processing can be *focused* or *unfocused* depending on the effective integration time in which the signals are processed. In the focused case the phase history of the signal is fully exploited over the whole integration time, and the maximum ideal along-track resolution that is achievable is given by:

$$\delta_x^{RS,SAR^f} = \frac{l_x}{2}. \tag{1.8}$$

On the other hand, the unfocused Doppler processing exploits the part of the integration time in which the signal phase variation is smaller than $\pi/4$. The final along-track resolution that can be obtained by processing the RS data with the unfocused Doppler processing is given by:

$$\delta_x^{RS,SAR^{uf}} = \sqrt{\frac{\lambda H}{2}}. \tag{1.9}$$

Although the resolution in the unfocused case is worse than the resolution in the focused case (since $\delta_x^{RS,SAR^{uf}} > \delta_x^{RS,SAR^f}$), the unfocused processing is simpler. This is because it requires only a linear phase compensation of the received echoes. For this reason the unfocused Doppler processing is the prefered SAR processing technique onboard airborne or satellite platforms, at the cost of reduced resolution.

Note that besides improving the resolution with respect to the real antenna aperture radar, a main advantage of using SAR techniques is the possibility to partially suppress the effect of clutter. This is because returns coming from the off-nadir in the azimuth direction are limited to the resolution cell of the SAR processed data, which is always

smaller than that of non-processed data, thus the amount of clutter reaching the antenna receiver is also smaller.

Across-track resolution

For the across-track direction, the SAR principle cannot be exploited since the Doppler theory is not applicable. This is because in the across-track direction there is no relative motion of the platform that carries the RS with respect to the targets and thus the backscattered signals have no Doppler shift. In this case, the across-track resolution mainly depends on the roughness of the surface σ_h with respect to the wavelength λ.

For a very rough surface ($\sigma_h \gg \lambda$), the across-track resolution of a RS is beam-limited, and given by:

$$\delta_y^{RS,Bl} = \frac{\lambda H}{l_y}, \tag{1.10}$$

where l_y is the antenna length in the across-track direction. From (1.10) it can be deduced that in the case of a very rough surface, the RS can resolve two targets in the across-track direction only if they are spaced by a distance at least equal to the antenna footprint in that direction.

For a slightly rough surface ($\sigma_h < \lambda$), the across-track resolution is pulse-limited , i.e., is given by the diameter of the circle centered in the nadir point, which intersects the ground at the moment when the transmitted wave has penetrated into the material to a depth equal to the range resolution δ_z^{RS}, thus is expressed by:

$$\delta_y^{RS,Pl} = 2\sqrt{\frac{Hc}{B_w}}. \tag{1.11}$$

For a smooth surface ($\sigma_h \ll \lambda$), the across-track resolution is given by the diameter of the first Fresnel zone DF:

$$\delta_y^{RS,Fl} = DF = \sqrt{2\lambda H}. \tag{1.12}$$

Fig. 1.4 shows a schematic representation of the resolution in the above-mentioned cases. As it can be seen, the smoother the surface, the better the resolution capabilities of the RS in the across-track direction, since $\delta_y^{Fl} < \delta_y^{Pl} < \delta_y^{Bl}$.

As already mentioned, the use of SAR techniques reduces the clutter coming from the along-track direction. In the across-track direction, the clutter can be reduced by increasing the directivity of the antenna, i.e., by increasing its dimension, as it can be deduced from (1.10). Since, because of physical constraints this is not always feasible, a common approach to the clutter reduction or identification is the use of suitable signal processing techniques, e.g., [1], [13]. As an example, Fig. 1.5 shows a SAR processed

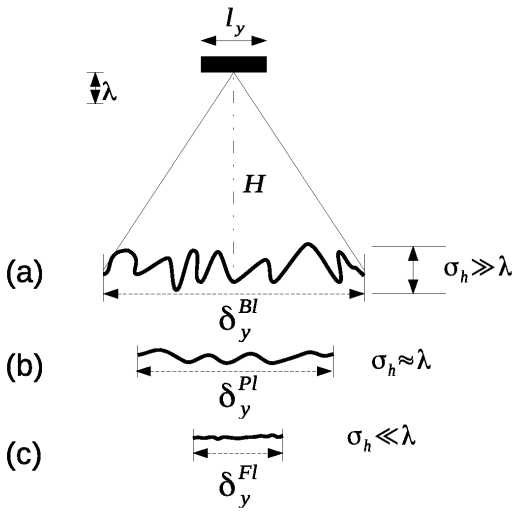

Figure 1.4: Schematic representation of the across-track resolution of a RS system. The across-track resolution cell is (a) Beam-limited for very rough surfaces, (b) Pulse-limited for slightly rough surfaces, and (c) Fresnel-limited for smooth surfaces.

radargram acquired by the MultiChannel Coherent Radar Depth Sounder (MCoRDS) in Antarctica, before (Fig. 1.5(a)) and after (Fig. 1.5(b)) clutter suppression achieved by using the algorithm presented in [1]. It is worth noting the improved quality of the processed radargram in Fig. 1.5(b), which highlights bedrock returns which are completely masked by clutter in Fig. 1.5(a).

1.4 Examples of radar sounder systems

As already mentioned, for the monitoring of the ice sheets and glaciers RSs are operated on airborne platforms, e.g., MultiChannel Coherent Radar Depth Sounder (MCoRDS) [14], High CApability Radar Sounder (HiCARS) [15], POLarimetric Airborne Radar Ice Sounder (POLARIS) [16]. Currently, spaceborne RSs have been used only for the exploration of other planets or moons. Examples are the Lunar Radar Sounder (LRS) of the Japanese orbiter Kaguya [4], the Mars Advanced Radar for Subsurface and Ionosphere Sounding (MARSIS) on the ESA's Mars Express Orbiter [6], and the Shallow Radar (SHARAD) of the Mars Reconnaissance Orbiter of NASA [5]. The latter two instruments are currently operating at Mars and are providing high quality data which allow a detailed study of the subsurface of the North Poles of Mars. The Radar for Icy Moon Exploration (RIME) [7] is another planetary RS instrument, currently under development. RIME is devoted to the sounding of the icy moons of Jupiter: Ganymede, Europa and Callisto. Studies for the definition of an Earth orbiting RS have been also carried out [8], [10], [17].

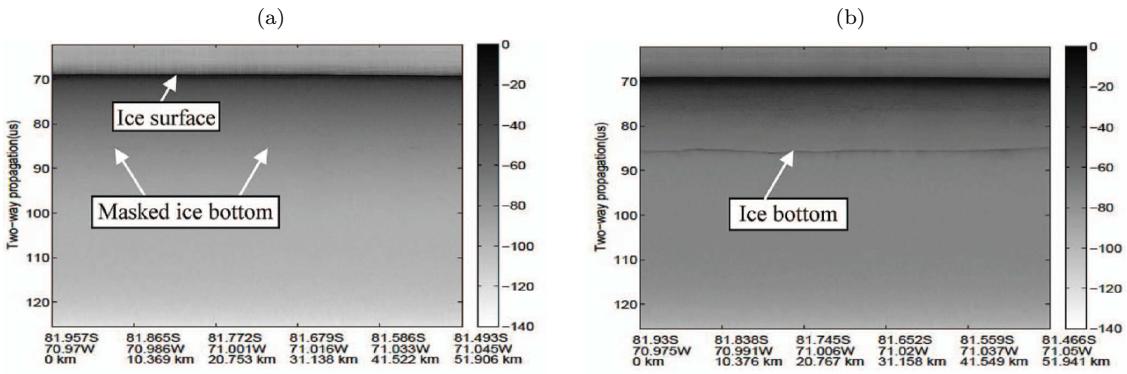

Figure 1.5: (a) Example of SAR processed radargram acquired by MCoRDS in Antarctica, and (b) The same radargram after applying clutter suppression processing [1]. Copyright: [1].

In order to better understand the relation between radar characteristics, platform height, subsurface penetration capability and geometrical resolution, in the following we provide some examples of both ice sheet and planetary RS systems.

Examples of airborne RSs

MultiChannel Coherent Radar Depth Sounder (MCoRDS) is a coherent ice depth sounder system developed at The University of Kansas, Lawrence, KS, USA [14]. MCoRDS is a flexible RS system, capable of operating over the frequency range 160-230MHz with a multichannel receiver and adjustable bandwidth of 10MHz to 60MHz. The system has been designed and optimized to sound fast-flowing glaciers and ice sheet margins and image an ice-bedrock interface covered with ice more than 3km thick in the interior. Thus, the main objective of MCoRDS is the measurement of ice sheet thickness. It has been operated in Antarctica and Greenland and integrated onboard three different platforms: i) the de Havilland DHC-6 Twin Otter (TO) at low altitude with two six element folded dipole subarray antenna, ii) the NASA DC-8 turbojet at high altitude with a collinear antenna array composed of five broad planar dipoles, and iii) the NASA P-3 aircraft at low altitude with an antenna composed of 15 dipoles. A simplified configuration of MCoRDS and the related system parameters are given in Tab. 1.1.
POLarimetric Airborne Radar Ice Sounder (POLARIS) is a polarimetric RS system developed by the University of Denmark [16]. POLARIS has quad polarisation capabilities which allow it to measure the anisotropic properties and crystal orientation fabrics to gain more insight about the stress and strain information of the polar ice sheets [18]. POLARIS has a dual-linear polarization wideband microstrip patch antenna that works at a central frequency of 435MHz (i.e., P-band) with 3 possible bandwidths (6MHz, 30MHz and 80MHz). Tab 1.1 reports an example of configuration of POLARIS and the related

Table 1.1: Examples of RS system parameters.

Parameter	Ice sheet RS		Planetary RS	
Name	MCoRDS [14]	POLARIS [16]	SHARAD [5] on Mars	RIME [7] on Jupiter Icy Moons
Platform	TO @ 500m	DHC6-TO @ 3500m	MRO @ 300km	JUICE @ <1000km
f_c [MHz]	195	435	20	9
B_w [MHz]	30	85	10	3
δ_z^{RS} [m]	4.3	1	10	50
Penetration depth [km]	4	3	1	9

parameters.

Examples of planetary RSs

SHAllow RADar (SHARAD) is a planetary RS on the MRO mission on Mars [5]. The scientific objective of SHARAD is to map dielectric interfaces to at least several hundred meters depth in the Martian subsurface and to interpret these results in terms of the occurrence and distribution of expected materials, including rock, soil, water, and ice. SHARAD has a 10m long dipole antenna which works at 20MHz central frequency, and a bandwidth of 10MHz. The instrument has a horizontal resolution of between 0.3 and 3km and a vertical resolution of 10m in the subsurface. A simplified configuration of SHARAD is provided in Tab. 1.1.

Radar for Icy Moon Exploration (RIME) is a planetary RS provided by ASI as a payload on the JUpiter ICy moon Explorer (JUICE) mission [7]. RIME is designed for studying the subsurface geology and geophysics of the Galilean icy moons (i.e., Ganymede, Europa and Callisto) and for detecting possible subsurface water. It uses a 16m dipole antenna that works at a central frequency of 9MHz. RIME is designed to achieve a penetration depth of 9km with a maximum resolution of 50m in the subsurface. A simplified configuration of RIME is provided in Tab. 1.1.

Chapter 2

State of the Art in the Development of Automatic Techniques for the Analysis of Radar Sounder Data Acquired at the Ice Sheets

This Chapter provides an overview of the State of the Art regarding the automatic analysis of RS data acquired at the ice sheet. First, we present a review of the literature regarding the automatic identification of subsurface targets. Afterwards, a review of the literature regarding the 3D reconstruction of the ice subsurface structure is given. Finally, we provide an overview of the literature on the estimation of ice subsurface power losses.

2.1 Automatic identification of ice subsurface targets

The analysis of radargrams is a very challenging task, since the amplitude of the reflections from the surface and subsurface is typically mixed with noise contributions, e.g., thermal noise, speckle, clutter, sidelobes. These noisy contributions may partially or even completely mask the useful signal, thus leading to wrong interpretation of the information contained in radargrams. Despite the advantages that the automatic techniques could provide, as mentioned in the introduction of this thesis, the related literature in the analysis of RS data is still limited. An attempt to automatically estimate the polar ice thickness from airborne data is presented in [19]. Here, the authors propose two techniques for the automatic detection of the ice surface and the bedrock interfaces, i.e., i) edge-based, and ii) active contour. In [20], a technique for tracing the depth of the Holocene in Greenland is presented. The technique is semi-automated and uses image

processing concepts based on histogram analysis and surface fitting to identify the transition region between the Holocene and Glacial ice. Besides these works, which deal with the segmentation of the ice sheet subsurface into different regions, there are a few works focused on understanding the ice stratigraphy, which is useful for ice flow modeling [21] or the isochronous characterization of the ice [22]. These objectives have motivated many efforts for developing automated or semi-automated methods (e.g., [23], [24], [25], [26], [27]). Other methods focus on the detection of water [28] or estimation of water extent at the ice/bedrock interface [29]. Other related works regard mainly the analysis of the targets visible in radargrams by comparison with ground truth data collected during drilling campaigns or using other sensors. As an example, in [30] the authors investigate how the structure of the ice subsurface affects the wave propagation and its impact on the radargram acquisition process. They compare RS data, ice core line-scan images (which display the stratigraphy of high-scattering zones for light), crystal orientation fabrics and dielectric properties of subsurface samples collected from an ice core for assessing the type of investigated targets in radargrams. This analysis is extremely useful, as its scientific output could act as reference knowledge that along with the radargrams allow for further automatic processing.

The literature regarding the analysis of RS data relevant to this thesis also includes works related to the study of the subsurface of planetary bodies. Indeed, patterns relatively similar to those characterizing the subsurface features of the Earth polar ice sheets are shown in radargrams acquired by RSs orbiting around other planetary bodies. For instance, the subsurface of the North Poles of Mars is characterized by layers of dry and wet ice. Therefore, the patterns shown in such radargrams are due to echoes coming from various ice layers interfaces and the underlying basement. Such features have been detected and investigated only recently by means of automatic analyses. As an example, [31] presents a technique for the detection of shallow linear features. Another work in which the goal is the detection and extraction of layered linear features is presented in [32]. Here, the authors propose the use of collaborative filtering in order to reduce the noise and highlight the returns of the target. The extraction of linear features is performed by exploiting the Steger filter. Another work regarding the analysis of the Martian subsurface, and in particular the detection of basal returns, is presented in [33]. Here, the authors propose the use of several theoretical models to characterize the statistical properties of the RS signals. In order to isolate the returns of the basement from other echoes, the algorithm exploits a region growing technique that combines the results of the statistical analysis with the geometrical properties of the subsurface features. A technique for the automatic detection of clutter returns is presented in [13]. Such studies prove a recent growth in interest in the development of automatic techniques for the analysis of

orbital RS data.

Automatic methods for the analysis of subsurface features have been also developed for terrestrial surface-mounted GPR data. Since decades, the aim of the GPR campaigns has been to provide meaningful information about the shallow underground, by non-intrusive means. In fact, their use has been devoted to the detection of buried objects (e.g., pipes, tanks, mines). These targets show specific signatures in radargrams, under the form of hyperbolas. In order to analyze them, several studies in the literature proposed the use of automatic techniques. For instance, in [34] after reducing the noise by means of a wavelet-based procedure, the authors use a fuzzy clustering algorithm for the identification of hyperbolas. In [35] the authors firstly enhance the useful signal by applying a sequence of preprocessing steps for noise removal. Afterwards, a buried target detector based on artificial Neural Networks (NN) is implemented. In [36], the potentiality of NNs is exploited for detecting hyperbola-like signatures in GPR radargrams affected by different levels of noise and clutter. Two fast detection algorithms for small underground targets, one based on NNs, the second based on a template-matching approach are presented in [37]. The SVM classifier is used in [38] for the recognition of the type of material of the subsurface target. Such goal is achieved after applying a sequence of operations to the radargram, i.e., preprocessing for noise removal, image segmentation to discriminate between background and target, and automatic object detection implemented by means of genetic algorithms.

Before going deeper into the investigation of the literature regarding the analysis of GPR radargrams and planetary RS radargrams, we recall some aspects pointed out in the introduction of the thesis. The three mentioned types of radargrams, i.e., ice sheet RS data, planetary RS data, and terrestrial GPR data, have both common and different characteristics. The common aspects regard the fact that these data are acquired with the same nadir-looking geometry, and that they show the subsurface. However, the coverage, resolution and the subsurface features typically shown in the three types of radargrams are different. Thus, the available automatic techniques for the analysis of terrestrial GPR and planetary RS data acquired on Mars cannot be directly applied to the analysis of the ice sheet subsurface acquired by airborne RS data. Nevertheless, such works along with recent advances in the processing of ice sheet RS data, represent a reliable starting point for the development of novel advanced methods for the investigation of radargrams of the ice sheets.

2.2 3D reconstruction of ice subsurface structure

Understanding the dynamics and processes taking place at the ice sheets requires improved 3D models of the ice sheet structure. An efficient way of achieving this is by using automatic techniques that integrate and/or exploit different types of data. However, the development of such techniques is still limited. Two methods to map the global 3D structure of the entire Antactica are presented in [39] and [40], whereas [41] and [42] present methods for mapping the ice subsurface of the entire Greenland. All these methods consider most of the available RS data acquired in Antarctica or Greenland at the time of their publication. Such data are extremely heterogeneous in terms of resolution and sample density, since they were acquired in different airborne campaigns conducted to meet different science requirements. However, the 3D maps are generated at a common single scale determined by empirically analyzing the global density of the data at hand. This choice has two potential drawbacks. In regions with high data sampling density, the use of a comparatively small scale results in the generation of a low resolution map, leading to possible loss of information. On the contrary, in regions with low data sampling density, the use of a too high scale determines the generation of elevation maps with artifacts or artificial features. In [43], the bedrock topography is estimated only locally, i.e., for the Jakobshavn Isbrae in Greenland and Byrd glacier in Antarctica. The work focuses on the description of a novel RS system used for data acquisition in these regions and emphasizes on its capability to reach the bedrock even under very thick ice ($\approx$ 3km) below the flightlines. However, it lacks a detailed description of the methods used to identify the scale and of the interpolation strategy used to reconstruct the 3D structure of the ice sheet. In [44], the authors propose a physically-based approach to calculate glacier ice thickness by using a dynamic model to obtain spatially distributed thickness of individual glaciers. The method uses two types of data, i.e., a complete inventory of glacier outlines and digital elevation models (DEM). It calculates glacier-specific distributed thickness based on the inversion of surface topography by using the principles of ice flow dynamics. The same method is further developed and adapted to glaciers on the Antarctic Peninsula in [45]. Another physically-based approach to the interpolation of ice thickness of the Aurora Subglacial Basin is proposed in [46]. The method is a development of those used in [39] and [47]. In [48], the basal topography of Bayley/Slessor region of East Antarctica is obtained by interpolating RS data with the kriging method. A mass conservation approach to mapping the glacier ice thickness, which exploits RS and interferometric synthetic aperture radar data, is presented in [49] and further improved and reused in [50] for the high-resolution ice thickness mapping in South Greenland.

This review of the related literature points out that there are several interpolation

methods used for the same purpose, i.e., 3D estimation of ice thickness and bedrock topography. However, it is worth noting that independently on the interpolation method used, all the above-mentioned techniques use empirically-derived scales for interpolation. For instance, in [48], [39], [45], the scales used are 20km, 5km, 100m, respectively. These values represent an acceptable compromise given the different characteristics of the data. However, none of them has been automatically identified on the basis of the specific properties of the data and of the characteristics of the investigated surfaces.

2.3 Ice power loss estimation

During the past decades, intensive studies have been carried out for a better estimation of the radar wave attenuation through ice and consequently for the estimation of ice power losses. The main goal of such studies is the ultimate unambiguous interpretation of the ice basal conditions and processes, which is still problematic due to the poor knowledge of radar power losses through the ice column.

The basic and widely used method for infering the radar attenuation is by using bedrock-driven approaches, i.e., the relationship between the ice thickness and the power returned from the bedrock. For instance, in [51] the pattern of reflected power from the bedrock (BRP) is used to infer the spatial pattern of basal properties. In [52], the authors improve the BRP concept which is then reused in [53]. Here, ice core data is used for modeling and estimating the englacial depth-averaged attenuation rate and the result is compared against radar-derived depth-averaged attenuation rate which is estimated by adjusting the method presented in [52]. The depth-averaged attenuation rate is also estimated in [54] by assuming constant reflectivity of the bedrock along the radargram. This assumption is the main weakness of the method, since it is unlikely to hold in a large scale context. A recent work [55] accounts for this weakness by proposing an improved empirical attenuation correction by fitting linearly variable attenuation rates along the radargram. This method also corrects for propagation losses due to rough ice surfaces. Another recent bedrock-driven approach is presented in [56]. The main advantage of this technique over most of the previous techniques, which assume either constant bedrock reflectivity or stationarity in the attenuation rate, is the use of a sliding target window approach for the local derivation of the depth-averaged attenuation rate.

Another approach to the estimation of ice losses is based on layer-driven methods. The main advantage of such approaches is that they do not rely on the bedrock reflections to estimate the radar attenuation rate, since the reflections of the bedrock are more complex and proven to be spatially variable, e.g., [52], [55]. The layer-driven methods rely on the assumption that the internal layers visible in the radargrams are isochonous,

as firstly hypothesized in [57]. The study carried out in [58] investigates the internal echo reflections by using RS data, ice core data, and two models of subsurface reflections (i.e., one of which considers only primary reflections, the other one that considers both primary and multiple reflections). This study reconfirms the hypothesis of the isochronous character of the internal layers and concludes that such layers can be used to aid studies of ice sheet dynamics. This has been also established in [53], in which it is stated that the radar-derived attenuation rates to several reflectors could constrain the depth-averaged attenuation rate profile and provide additional tests for the attenuation models. Recently, a method based on this approach has been presented in [59]. The method uses a linear regression technique to estimate the depth-averaged attenuation rate and relies on the assumption that the internal layers highlighted in radargrams are specular and that the reflectivity of the layers is uniform in the range direction. The layer-driven approach and the assumption of uniform vertical reflectiviy have been also used in [60] to study the spatial uniformity of the attenuation. As noted in [59], the assumption of uniform vertical reflectivity does not hold along the entire vertical profile since there are several radar bright reflections due to higher variations in layer reflectivity.

As it can be seen, there are several methods for the estimation of the radar depth-averaged attenuation rate and consequently for the ice power loss estimation. However, most of such methods assume a linear trend of power attenuation along the entire ice column, although it is well-known that the attenuation depends on the ice temperature which is variable within the ice sheet. The linear approximation of the power attenuation is the main weakness of the available techniques. This calls for novel techniques that can take into account ice temperature variations for estimating the power losses through ice.

Chapter 3

A System for the Automatic Classification of Ice Subsurface Targets in Radar Sounder Data

This Chapter[1] *provides the first contribution of the thesis in the context of the identification of ice sheet subsurface targets in RS data. In particular, it presents a novel and efficient system for the automatic classification of ice subsurface targets present in radargrams. The core of the system is represented by the extraction of a set of features for target discrimination. The features are based on both the specific statistical properties of the RS signal and the spatial distribution of the ice subsurface targets. Such features are then given as input to an automatic classifier based on Support Vector Machine (SVM). Experimental results obtained on two datasets acquired by airborne-mounted RSs in large regions of Antarctica confirm the robustness and effectiveness of the proposed classification system.*

3.1 Introduction

Exhaustive investigations of the ice sheet subsurface can be carried out by analyzing the information contained in the huge archives of RS data. In this Chapter we present an advanced and effective system for the automatic classification of the whole backscattering area of the ice subsurface targets visible in the RS data. In brief, from a physical point of view, the ice subsurface is composed by layers of ice and the underlying bedrock [3].

[1] Part of this chapter appears in:

[61] Ilisei, A.-M. and Bruzzone, L., "A System for the Automatic Classification of Ice Sheet Subsurface Targets in Radar Sounder Data," in *IEEE Transactions on Geoscience and Remote Sensing*, Vol. 53, No. 6, pp. 3260-3277, 2015.

In radargrams, they appear as different patterns that can be recognized by their structure, continuity, depth location and reflected wave amplitude and phase. Another pattern present in radargrams corresponds to the measurements of pure noise. Therefore, *layers*, *bedrock* and *noise* are the targets that we aim to automatically classify (a detailed description of the ice sheet subsurface targets is given in Sec. 3.2). Identifying these ice subsurface targets represents a first fundamental step for a subsequent more complete understanding of the ice sheets, e.g., the computation of the ice thickness, the study of archeological changes (see Sec. 3.2 for details). The complexity and the large amount of radargrams call for the development of automatic techniques for the identification of such targets. However, automatic approaches to the identification of the ice sheet subsurface targets have not been sufficiently addressed by the scientific community (see Sec. 2.1). Also, it is worth noting that the few existing techniques only focus on either the detection of linear features in the ice stratigraphy or the detection of the ice/bedrock interface or the identification of the basal scattering area. Moreover, they are not designed for addressing the problem of the heterogeneity of radargrams. The existing RS datasets are often made up of radargrams characterized by different attributes (e.g., resolution) as they are typically acquired during several airborne campaigns with different sensors or with the same sensor operated at different modes (e.g., bandwidth). In this context, it is important to develop automatic systems that can accurately identify the above-mentioned targets all together and can be used in a flexible way on different types of radargrams.

The proposed automatic classification system combines advanced image processing and machine learning techniques with the knowledge about the physical distribution of the targets and fundamentals on radar wave backscattering. After an initial elevation correction step applied to the radargrams for removing the effect of fluctuating aircraft altitude, they are given as input to the system, which is made up of two main components: i) feature extraction, and ii) automatic classification based on Support Vector Machine (SVM). The feature extraction is the core of the system and also the main novel contribution of this work. The objective at this stage is to extract from the radargrams effective parameters for target discrimination (in this work we call such parameters "features", in accordance with the pattern recognition literature; it is worth to note that a conventional term used in the glaciological and ice radar communities for "ice subsurface targets" is "ice subsurface features". However, we use the term "ice subsurface targets" to avoid possible confusion caused by the same word "feature" associated with two different fundamental concepts). We propose a set of features that are able to model and correlate the backscattering properties of the radar signal with the spatial properties of the subsurface targets. The extraction of such features is done after a detailed study of the statistical properties of the radar signal and of the spatial distribution of the ice subsurface targets.

The second component of the system uses the extracted features to perform the automatic classification of ice subsurface targets by using the SVM classifier. The main advantages of the system are: i) robustness and/or adaptiveness to the heterogeneity of radargrams as a consequence of both the features used and the learning approach employed; ii) capability to obtain objective quantitative results (i.e., exactly the same criteria are used for all radargrams, thus enabling the extraction of targets in a consistent and comparable way on all radargrams); and iii) computational speed and efficiency due to the possibility of parallelizing the algorithm. For these reasons, the system is suitable for the analysis of the ice subsurface at large scale from radargrams acquired by RS sensors with different characteristics (e.g., central frequency, bandwidth), as it will be proven in the following. The system has been validated on two real-world datasets [62]: i) a dataset made up of 8 radargrams acquired in sequence off $\approx$ 400 line-km in Central Antarctica by the airborne-mounted MCoRDS instrument [63], and ii) a dataset made up of 14 radargrams acquired in parallel- and cross-track configurations over an area of about 1000 km^2 in SE Antarctica (Byrd Glacier) by MCoRDS2 [64].

The rest of this Chapter is organized as follows. A complete description of the ice sheet subsurface targets is given in Sec. 3.2. Sec. 3.3 and Sec. 3.4 present the main components of the automatic classification system, i.e., the feature extraction technique and the classification method based on SVM. Experimental results obtained on the two RS datasets acquired in Antarctica are reported in Sec. 3.5. Finally, Sec. 3.6 discusses the capabilities and limitations of the system and proposes future developments of this work.

3.2 Proposed system: definition of target classes in RS data and general architecture

The classification of target backscattering behavior in RS data requires a very good understanding of the structural properties of the ice subsurface and radar wave propagation [65]. As briefly introduced in the previous section, studies of the ice sheets (e.g., [3], [66]) reveal that the ice column is made up of a sequence of ice layers, characterized by different dielectric properties. They have been generated over millennia by snow accumulation (on the underlying bedrock) alternated by depositions of impurities from volcanic explosions [67], and ice flow dynamics [68], therefore have an isochronous character [57]. In radargrams they appear as spatially coherent surfaces that generate quasilinear patterns. The brightness of such patterns (which is related to the amplitude of the received wave) decreases with depth due to the attenuation through the subsurface [65]. Another physical component of the ice sheet subsurface, which is located below the layers, is the

bedrock. In radargrams, the bedrock can be identified as the deepest scattering area. Note that, contrary to the real scenario in which the bedrock interface is expected to be contiguous, the bedrock scattering area visible in radargrams can be composed of disjunct regions, i.e., on some traces of the radargram the bedrock returns can be completely absent. The discontinuities are likely to be due to the loss of transmitted power through the ice column, to the wave total reflection caused by the supraglacial or englacial water [69], or to acquisition issues (e.g., clutter returns that can completely mask the return from nadir [3]). Therefore, the quality of the bedrock scattering area mainly depends on the type of material, the topography, the conditions at the basal interface and the processing applied to the radar data. The bedrock completely attenuates the transmitted wave. This implies that at a depth larger than that of the bedrock the radar receiver measures only noise. This is visible in the bottom part of the radargrams as a homogeneous region characterized by the absence of relevant reflections. Another noise-like pattern, visible for a few hundred of meters above the bedrock is called echo-free zone (EFZ). The EFZ has been firstly identified and studied in [70]. Then, papers like [66], [71], [30] have provided deeper insight and recently some authors have confirmed the presence of the EFZ [72]. According to such studies, the EFZ is often seen away from the ice domes and ice divides, but in extensive areas of the ice sheets. Note that the EFZ is not an ice subsurface physical region (like the layers or bedrock), but rather a consequence of the radar acquisition process. In [30], it is suggested that at the EFZ corresponding depth the disturbances introduced by the ice flow caused an increase of the layer roughness. Such large scale roughness reduces the coherency of the reflecting surfaces, thus generating the echo-free zone (EFZ). Besides the layers, bedrock and noise regions, which are typically shown in radargrams (see Fig. 3.0(a)), near-bed reflectors have been recently identified as freeze-on ice [72]. These reflectors are found primarily along the high ridges at the valley heads and along the steep valley walls surrounding subglacial mountain peaks. Furthermore, when present, deep specular and strong reflections are associated with subglacial lakes [73]. Therefore, the freeze-on ice and the liquid water constitute other two subsurface targets (see Fig. 3.0(a)), which should be considered in the modeling of the subsurface. However, since by visual interpretation it is difficult to assess with high accuracy the freeze-on regions (if present) and given that in the datasets at hand no liquid water returns could be identified, in the following we do not consider such regions as target classes for automatic classification.

The importance of identifying the ice sheet subsurface targets has been often highlighted in the literature. In particular, the results obtained from the presented algorithm can be used for instance in studies that can further focus on the interpretation of the detected layered area only, by applying other techniques for the identification of individ-

ual layers. Regarding the EFZ, in [30] the authors state that identifying the EFZ onset is fundamental since it indicates changing archeology that shall be accounted for in the modeling of ice sheet dynamics (similar to the identification of the depth of the Holocene in Greenland [20]). Also, one can analyze the shape of the EFZ for a better understanding of its formation. Finally, the identification of the whole bedrock backscattering area can be used in geological studies for assesing the type of material the bedrock is made of [74] or to understand the reasons for which the bedrock is thicker or thinner or it completely disappears at some coordinates. Moreover, the detection of the first return of the bedrock (i.e., the basal interface) helps estimating the topography of the bedrock, computing the thickness of the ice column and inferring information about the basal boundary conditions and processes (e.g., presence of melted ice at the interface). The last return of the bedrock marks the depth below which the losses through the subsurface (ice and bedrock) have completely attenuated the transmitted power. Thus, it can be used to derive the absorption properties of the bedrock.

In this work we aim to develop a system for the automatic classification of *layers*, *bedrock* and *noise* (which includes also the EFZ region). An example of backscattering from these classes is given in Fig. 3.0(b). In order to perform the classification, the radargrams are initially altitude corrected for removing the effect of the aircraft fluctuations. Then they are given in input to the classification system, which consists of 2 main components, i.e., i) feature extraction for target description, and ii) automatic classification based on SVM. As it will be explained later, the system requires a mimimum amount of human interaction in the training phase, in which the values of the few system parameters should be tuned to both the characteristics of the data and the scale of the subsurface targets. However, this not a critical problem, since such parameters are directly related to properties of the targets and can be easily derived. On the other hand, after the training, the system is completely automatic. Moreover, it is important to mention the flexibility and learning capabilities of the system, e.g., depending on the radar frequency and resolution of the radargrams, different target classes with associated patterns can be identified (e.g., high resolution data allows the identification of crevasses). Therefore, one first needs to set the number of classes, appropriately model the properties of the classes in the feature extraction phase and then train the classifier to automatically recognize such classes.

3.3 Proposed system: feature extraction

The possibility to measure similar values of reflected power from different targets (e.g., returns from deep layers and bedrock can have the same power, see Fig. 3.0(b)) and the

(a)

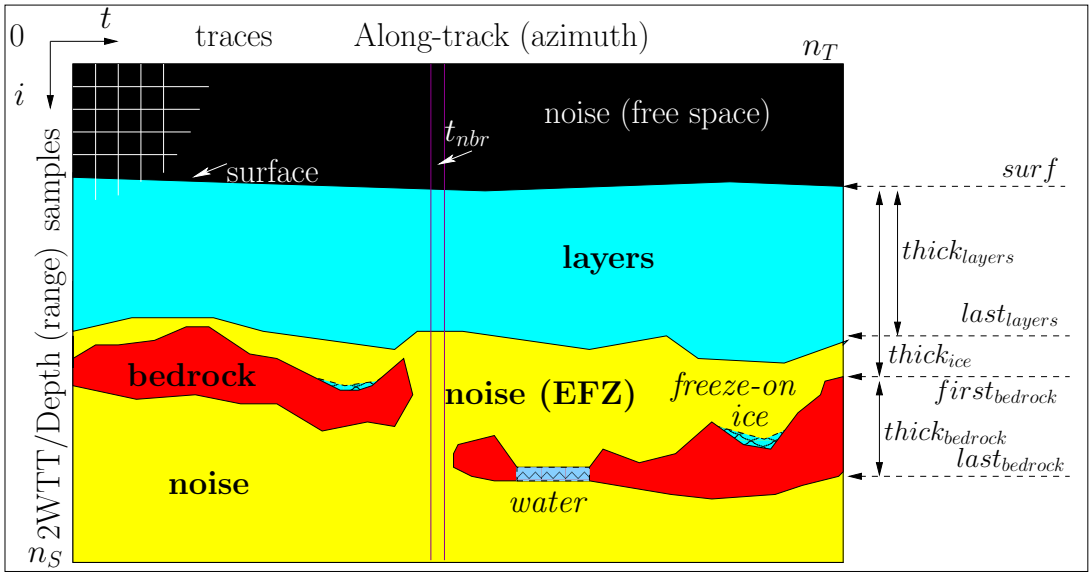

(b)

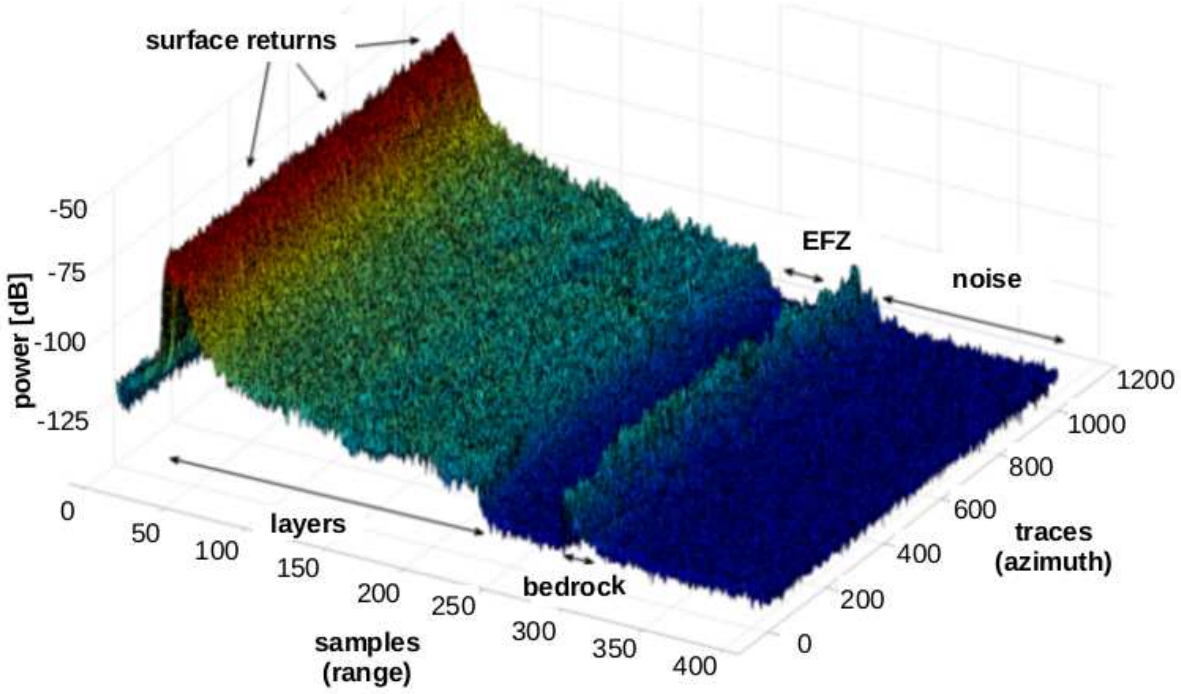

Figure 3.1: (a) Qualitative representation of ice sheet target classes typically visible in radargrams. In the presented work, only the target classes highlighted in bold, i.e., layers, bedrock, noise, are considered, whereas those highlighted in italics, i.e., water, freeze-on ice, are intentionally omitted. For details see Sec. 3.2. (b) Example of backscattering from the *layers*, *bedrock* and *noise* target classes.

noisy character of the radar images make the extraction of significant features for automatic classification a very challenging task. Here we address this problem by presenting a set of features that we chose after a detailed analysis of the amplitude fluctuation of the radar signal and of the spatial distribution of the investigated targets. For ensuring a logical flow, we structure this section in three parts. First, in Sec. 3.3.1 we present the preliminary analysis that we performed on the statistical properties of the radar signal. Then, in Sec. 3.3.2 we analyze the spatial distribution of the subsurface targets. Finally, in Sec. 3.3.3 we describe in detail the procedure for extracting features that model both the statistical and the spatial properties of the radar signal and of the subsurface targets.

3.3.1 Analysis of the statistical properties of the radar signal

Similarly to [33], we first performed a *statistical analysis* of the distribution of the radar signal. We analyzed the distribution of the radar signal by empirically fitting several probability density functions (pdf), i.e., Rayleigh (R_{pdf}), Nakagami (N_{pdf}), K (K_{pdf}), Gamma (G_{pdf}), to the histogram of samples drawn from regions corresponding to the investigated target classes. The abovementioned pdfs are parametric models, i.e., they can be described by using a finite number of parameters $\theta = (\theta_1, \theta_2, ...)$. Tab. 3.1 reports the parameters describing each of these theoretical distributions. The choice of these pdfs is motivated by their expected capability to model the amplitude fluctuations of the radar signal backscattered by different targets and/or processed with different algorithms, as it has been proven in works like [11], [33]. As such, the Rayleigh pdf (R_{pdf}) typically models the amplitude oscillation of a zero-mean additive Gaussian noise (AWGN) (e.g., this is the case of thermal noise measured by the radar in the regions with no backscattering). The Nakagami pdf (N_{pdf}) generally models amplitude radar data that have been priorly subjected to multilooking processing (for speckle reduction). The K pdf (K_{pdf}) generally guarantees good performances for fitting data from regions with bunched scatterers (e.g., this is the case of *layers* and *bedrock* returns). The Gamma pdf (G_{pdf}) is generally employed in the intensity domain (I), for fitting data whose distribution in the amplitude domain (A) follows a Nakagami pdf (we remind that $I \propto A^2$). Moreover, due to its flexibility, the Gamma pdf is likely to model data whose original distribution has been altered by possible processing. The analytical formulation of these pdfs along with the procedure for estimating their parameters are reported in Appendix A 3.7 (for further details refer to [33], [11], [75]).
Among all the investigated distributions, the best fitting model for each class can be chosen as the one that minimizes the Kullback-Leibler (KL) distance [76] between two

distributions $\mathcal{H}$ and $\mathcal{M}$, defined according to:

$$KL(\mathcal{H}, \mathcal{M}) = \sum_{A_i} \mathcal{H}(A_i) \log \frac{\mathcal{H}(A_i)}{\mathcal{M}(A_i)}, \tag{3.1}$$

where $\mathcal{H}$ is the real histogram of the amplitude samples and $\mathcal{M}$ is one of the investigated theoretical models, i.e., $\mathcal{M} = \{R_{pdf}, N_{pdf}, K_{pdf}, G_{pdf}\}$.
Thus, given a specific RS instrument and the related data, we can select the distribution that best fits the target classes as the model that empirically minimizes (3.1).

Table 3.1: Theoretical models and their parameters.

Distribution	Parameters	Parameter name
R_{pdf}	$\theta_R = \mu_{A^2}$	mean power
N_{pdf}	$\theta_G = (\mu_{A^2}, \beta_N)$	mean power, shape
K_{pdf}	$\theta_K = (\mu_{A^2}, \beta_N)$	mean power, shape
G_{pdf}	$\theta_G = (\alpha_G, \beta_G)$	scale, shape

3.3.2 Analysis of the properties of the subsurface targets

In order to properly design the proposed system, we also performed a qualitative analysis of the ice subsurface representation in radargrams (see Fig. 3.1). This allows obtaining an approximate knowledge of the *location and spatial distribution* of the target classes, which can be then used in the feature extraction for classification. From this analysis we derived that:

i) The *expected order in the range direction* of the ice sheet subsurface target classes visible in radargrams is: *layers*, *noise (EFZ*, if present), *bedrock* and *noise*. This statement has general validity, as it could be derived from Sec. 3.2.

ii) The ice subsurface targets visible in radargrams are mostly *extended in the along-track direction*, due to the isochronous character of the ice stratigraphy and the continuous shape of the bedrock.

iii) The ice subsurface targets shown in radargrams present *significant variation of backscattering along the range direction*. These variations are caused by reflections from the layered structure of the ice column and the basal interface.

Before going further, it is important to notice that the radargrams can be partitioned in two main regions, the subsurface region R_{ss} that contains all the target classes of interest

(i.e., layers, bedrock, noise) and a region R_{noise} at the bottom of the radargrams that contains exclusively noise measurements. In order to speed-up the processing, we will focus the following analysis on the R_{ss} region.

3.3.3 Features that model the statistical properties of the radar signal and the geometrical distribution of the subsurface targets

The analysis on the statistical distribution of the amplitude radar data and the location and spatial distribution of ice subsurface targets that has been carried out previously enabled the identification of the features for classification described below.

1. *Parameters of the best fitting model.* Once the best fitting model for the statistical characterization of the radar signal has been identified (see Appendix A 3.7 and (3.1)), we use the values of its parameters θ_{best} as features. In other words, if the best model is the K_{pdf}, then $\theta_{best} = \theta_K = (\mu_{A^2}, \beta_K)$, or if the best model is G_{pdf}, then $\theta_{best} = \theta_G = (\alpha_G, \beta_G)$, and so on. In order to cover the whole radargram space, for computing these features we employ a *sliding window approach*, as in the following. We use a rectangular window inside which we estimate the values of the desired parameters (by using the appropriate eq. among (3.9), (3.11), (3.13), (3.15)). The window is moved over the R_{ss} region with a step of one pixel both in the along-track and range directions. In order to filter out some noisy contributions, the final value of these features at each step of the sliding window is computed by averaging the estimated values on overlapping windows. It is worth mentioning that, from a statistical and image processing point of view, the size of the rectangular window ($W_z \times W_x$ (range $\times$ along-track)) should be sufficiently small for avoiding filtering the information at the borders of the scattering classes, while the number of samples inside the rectangular window should be sufficiently large for a good estimation of the parameters of the distributions. The resolution of the radargram, the spatial distribution and possibly the knowledge of the scale of the subsurface targets should also be considered when choosing the size of the sliding window. From the qualitative analysis performed previously regarding the spatial distribution of the subsurface targets, i.e., they are elongated in the alogn-track direction and present higher backscattering variation in the range direction, we can derive that an initial constraint on the choice of the sliding window is $W_x > W_z$. This constraint allows for a more consistent averaging when applying the sliding window approach, as it ensures a high level of affinity among the samples within the window. Such observation on the choice of the values for W_z and W_x hold for all the features computed on a sliding window basis.

2. *Texture*. As pointed out in Sec. 3.2, a qualitative analysis of the radargrams indicates that different target classes present distinctive patterns. We convert such qualitative information into a quantitative measure, by computing a texture feature. Among the many texture measures used in radar image processing (e.g., [77]), we consider the entropy Ent, which is a simple but informative measure. The entropy is a statistical measure of the uncertainty of a random variable, i.e., the more uncertain a random variable, the higher its entropy value. Accordingly, when computing the entropy of the samples of the radargram that belong to the *layers* and *bedrock* classes, it is expected to obtain a high value. This is due to the fact that the amplitudes of the backscattered waves in these regions can have very large dynamic range since they also depend on the structure and dielectric properties of the investigated targets which can vary significantly within the ice subsurface. On the other hand, the *noise* regions are characterized by relatively similar values (resulting in a less textured portion in the radargram), therefore their entropy is relatively lower. Thus, Ent helps in differentiating the subsurface targets on the basis of specific patterns that are characterized by the probability of appearance $\wp(C_i)$ computed in a local neighborhood $W_z \times W_x$, according to the sliding window approach described previously, i.e.,

$$Ent = -\sum_{C_i \in W_z \times W_x} \wp(C_i) \log_2 \wp(C_i), \tag{3.2}$$

where C_i is a quantized version of the log-amplitude data, i.e., $C_i = Q\{10 * \log_{10}(A_i)\}$ where $Q\{\cdot\}$ is the uniform quantization operation on n_q levels. Note that the quantization is a common operation used to reduce the very large dynamic range of the radar data to only n_q distinct values (e.g., [78]).

3. *Kullback-Leibler distance between the distribution of the samples of the target classes and of the noise*. Using the same sliding window approach and the output of the statistical analysis, we generate a feature that statistically models the distance between the measured bakscattering and the background noise. The literature suggests that a potential such statistical distance measure applicable to RS data is the KL distance [33]. Accordingly, we computed the KL distance of the radargram $\mathrm{KL}_{R_{ss}}$, by applying (3.1) to the R_{ss} region. Here, $\mathcal{H}$ is the histogram of the amplitude samples within the sliding window and $\mathcal{M}$ is the noise model fitted on the samples of the window. The values of the noise parameters have been estimated (as explained in Appendix 3.7) on the R_{noise} region. Note that the $\mathrm{KL}_{R_{ss}}$ is a smoothed version of the input radargram, in which the most scatterable subsurface target are highlighted. Therefore, $\mathrm{KL}_{R_{ss}}$ represents a good measure to discriminate between the samples belonging to high backscattering areas (i.e., *layers* and *bedrock*) and those of noise.

4. *Range position of the subsurface targets.* Intuitively, useful information that could help in discriminating the different types of backscattering classes is the distance $Dist_z$ of the subsurface targets with respect to the air/ice interface *surf*, see (3.3). *surf* is detected automatically for each trace of the radargram as the position of the maximum return along the trace. This is a fast and simple approach that has been employed in other works for the analysis of airborne acquisitions (e.g., [25]).

$$Dist_z(i,t) = [i - surf(t)], \forall i > surf(t), \forall t. \tag{3.3}$$

5. *Relational feature.* A less intuitive feature relates the position of the samples in the range direction with their backscattering strength. For this reason we call it relational feature *Rel*. Its objective is mainly to enable the separation between the returns of the classes with high backscattering, i.e., *layers* and *bedrock*. To this aim, a first requirement is to isolate in the radargram these high backscattering classes. This is achieved by exploiting the property of the statistical $\mathrm{KL}_{R_{ss}}$ distance measure, i.e., the fact that it highlights the most scatterable targets. In particular, we threshold the $\mathrm{KL}_{R_{ss}}$ as follows:

$$\mathrm{KL}_{bin}(i,t) = \begin{cases} 1 & \text{if } \mathrm{KL}_{R_{ss}}(i,t) \geq thr_{\mathrm{KL}} \cdot \mu_{\mathrm{KL}_{R_{noise}}}, \\ 0 & \text{otherwise,} \end{cases} \quad \forall i,t, \tag{3.4}$$

where KL_{bin} is the resultant thresholded (binary) $\mathrm{KL}_{R_{ss}}$ measure, $\mu_{\mathrm{KL}_{R_{noise}}}$ is the mean of the samples of the $\mathrm{KL}_{R_{noise}}$ (where $\mathrm{KL}_{R_{noise}}$ has been generated by applying (3.1) to R_{noise}) and thr_{KL} is a user defined threshold that tunes the degree of similarity between the samples of the $\mathrm{KL}_{R_{noise}}$ and those of the $\mathrm{KL}_{R_{ss}}$ measures. Note that, since the range of possible values of the threshold is $thr_{KL} > 0$, choosing an optimal value for the threshold requires a minimum amount of human interaction. In order to filter out only the regions of the $\mathrm{KL}_{R_{ss}}$ corresponding to the class *noise* in the amplitude domain, a low value of the thr_{KL} is preferable. Otherwise, by choosing a too large value, the risk is to filter also high backscattering contributions. After the thresholding operation, the discrimination between samples belonging to different backscattering classes is achieved by taking into account their expected order in the range direction (see Sec. 3.3.2). In particular, *Rel* is generated in a columnwise manner, starting from *surf* (with the initial condition $Rel[surf(t), t] = 1, \forall t$), and computing a constrained cumulative sum while moving downwards over the KL_{bin} map. The constraint is to sum 0 instead of 1 at the positions where $\mathrm{KL}_{bin} = 1$. Qualitatively, by looking downwards in the range direction, each trace of the *Rel*

feature has monotonically increasing values, with a behavior depending on the measured backscattering contribution (see Fig. 3.2, which represents the vertical profile of a generic trace t' of the *Rel* feature).

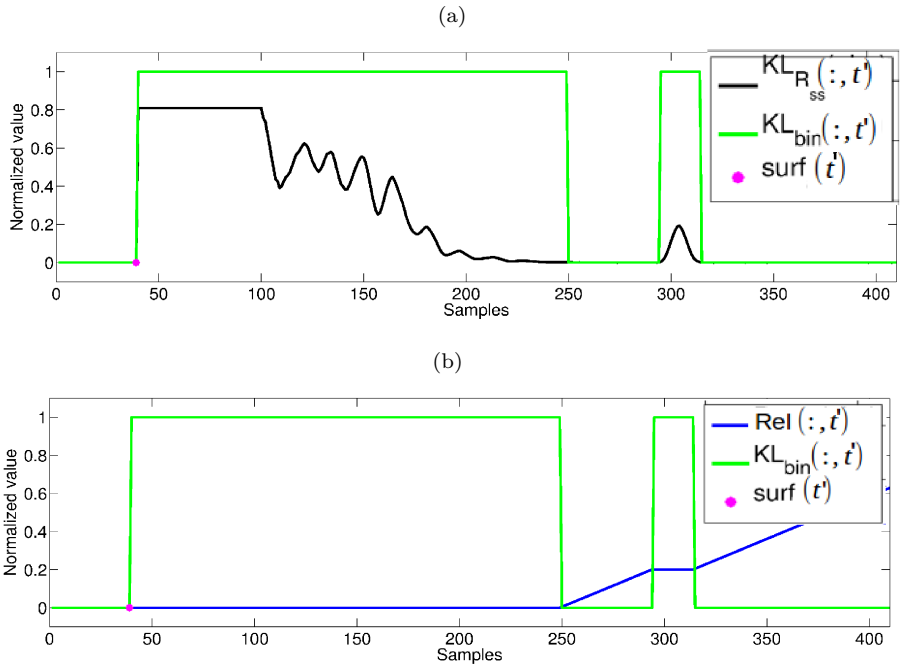

Figure 3.2: (a) Qualitative example of trace t' for the $\mathrm{KL}_{R_{ss}}$ and KL_{bin} measures; and (b) Corresponding relational feature *Rel*.

In the presented system, all the above-mentioned features are given as input to the classification algorithm. These features are the amplitude of the backscattering A, the parameters of the best fitting model θ_{best}, the entropy Ent, the Kullback-Leibler distance $\mathrm{KL}_{R_{ss}}$, the range position of the subsurface targets $Dist_z$ and the relational feature Rel. Therefore, the resulting feature vector $\mathbf{v}$ can be defined as:

$$\mathbf{v} = [A, \theta_{best}, \mathrm{KL}_{R_{ss}}, Ent, Dist_z, Rel]. \tag{3.5}$$

3.4 Proposed system: automatic classification with Support Vector Machine

The feature vector is given as input to a supervised automatic classifier. Based on a set of labeled training samples, the aim of the automatic classifier is to build a model (characterized by a set of parameters) which can accurately predict the labels for unknown (test) target samples. There are several automatic classifiers presented in the literature among which we chose the SVM [79]. The SVM is currently the state of the art in the

automatic classification of remotely sensed data [80]. Our choice is also due to the fact that the SVM has many properties very useful for solving our classification problem. Among these properties, we mention: i) very good generalization capability (it is able to avoid overfitting the model on the training samples); ii) capability to solve non-linearly separable problems in the original feature space; and iii) sparseness and uniqueness of the solution of the learning problem.

The SVM is a binary classifier. However, multiclass problems can also be solved by employing architectures made up of different binary SVMs (e.g., one against one (OAO), one against all (OAA)) [81], [82]. Here, the basic principle of the binary SVM is only briefly summarized. For solving non-linearly separable problems in the original feature space, the SVM uses a mapping function to project the samples into a higher dimensional feature space in which they are separable by hyperplanes. The mapping is done implicitly by a kernel function (e.g., linear, polynomial, gaussian) and the classification is performed after optimizing a convex objective function during the training phase of the SVM. The convexity of the objective function guarantees a unique solution, which is the optimal decision boundary between classes. Such decision boundary is the hyperplane in the transformed kernel space that maximizes the geometric margin between the training samples of the two classes taking into account a regularization term. There are several studies that treat both theoretical and practical aspects related to the use of the SVM (e.g., [80], [83]). As this kind of analysis is out of the scope of this work, we here provide only the analytical formulation of the objective function to be optimized in the learning process of the SVM and the corresponding decision boundary that have been used by the presented system. The dual formulation used for solving the constrained optimization problem associated with the training of the SVM is given by:

$$\begin{cases} \max_{\pounds} \sum_{i=1}^{n_\Psi} \pounds_i - \frac{1}{2} \sum_{i=1}^{n_\Psi} \sum_{j=1}^{n_\Psi} \kappa_i \kappa_j \pounds_i \pounds_j \mathcal{K}(\mathbf{v}_i, \mathbf{v}_j) \\ \text{subject to: } \sum_{i=1}^{n_\Psi} \kappa_i \pounds_i = 0, \quad 0 \leq \pounds_i \leq \varsigma, \quad 1 \leq i \leq n_\Psi, \end{cases} \tag{3.6}$$

where n_Ψ is the number of training samples characterized by the pairs $(\mathbf{v}_i, \kappa_i)$. $\mathbf{v}_i$ is the feature vector (see (3.5)) and κ_i is the label associated to the sample i. $\pounds_i$ are the Lagrange multipliers involved in the optimization process and ς, also called error penalization term, represents the cost associated to a wrong classification. ς and the parameters of the kernel function $\mathcal{K}(\mathbf{v}_i, \mathbf{v}_j)$ constitute the set of SVM model parameters that have to be optimized during the learning process. After the optimization, the final decision boundary (solution) $\mathcal{D}$ of the SVM is given by the following equation:

$$\mathcal{D}(\mathbf{v}) = \sum_{i \in SV} \kappa_i \pounds_i \mathcal{K}(\mathbf{v}_i, \mathbf{v}) + b, \tag{3.7}$$

where b is the bias term, which measures the distance of the hyperplane from the origin.

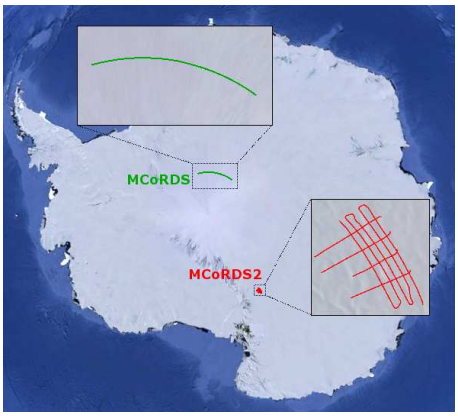

Figure 3.3: Location and flightlines for the acquisition of the MCoRDS and MCoRDS2 radargrams investigated in this work.

Note that the sparseness of the solution is explained by the fact that only a subset of samples $i \in SV$ associated to non-zero Lagrange multipliers, i.e., the support vectors, are necessary in the definition of the separation hyperplane.

3.5 Experimental results

We applied the presented algorithm to two datasets acquired by the MultiCoherent Radar Depth Sounder instrument (MCoRDS), owned by the Center of Remote Sensing of Ice Sheets (CReSIS) [62]. The datasets where acquired by the instrument operated with different bandwidths, i.e., $B_w = 9.5$MHz and $B_w = 30$MHz, in different regions of Antarctica. In order to distinguish the data, when operated with $B_w = 9.5$MHz, the instrument and the dataset are called MCoRDS, while when operated with $B_w = 30$MHz, they are called MCoRDS2. The approximate positions and the paths followed by the aircrafts carrying the instruments, MCoRDS and MCoRDS2, are shown in Fig. 3.3, in green and red, respectively. In the following we present: i) the description of the two datasets, ii) the results of the statistical analysis of the radar signal, iii) the experimental setup employed in the training phase of the SVM classifier, iv) the classification results, and v) the computational efficiency obtained by applying the presented technique to the two datasets.

3.5.1 Dataset description

The first considered dataset (MCoRDS) was acquired during the sounding campaign conducted in Central Antarctica in November 2010 [63]. It is made up of 8 radargrams acquired in sequence, i.e., from (-86.00°N, -15.67°E) to (-86.02°N, 29.45°E), over a dis-

tance of $\approx$ 400 line-km (which corresponds to $n_T = 27350$ traces). The instrument was flown on a jet aircraft (DC-8) at high altitude ($H \approx 7000$m). The central frequency of the instrument and the bandwidth are $f_c = 193.5$MHz and $B_w = 9.5$MHz, respectively.
The second dataset (MCoRDS2) was acquired at $f_c = 193.5$MHz with $B_w = 30$MHz. The instrument was flown on a TO aircraft at a relatively low altitude ($H \approx 500$m) in parallel and cross-track configurations over an area of around 1000km^2, i.e., within (-80.93°N, 145.72°E) and (-80.40°N, 148.10°E), over the Byrd Glacier in Antarctica, in December 2011 [64]. For obtaining best quality dynamic range, the MCoRDS2 dataset has been generated by multiplexing in time two types of data: i) signals collected from the shallow subsurface, acquired by using a waveform playlist (wpl) coupled with low gain channel (LGC) and a pulse duration $\tau_{ps} = 1\mu$s, and ii) signals collected from the deep subsurface, acquired by using a wpl coupled with high gain channel (HGC) and pulse duration $\tau_{pd} = 10\mu$s [84], [14]. However, this combination introduces a certain amount of heterogeneity between the radiometric quality of the data acquired in shallow and deep modes, which is difficult to handle at data processing level. Considering this and the fact that the low gain channel acquires data exclusively from the first km within the subsurface (i.e., class *layers*), and given that our purpose is the classification of ice subsurface targets, in our analysis we investigated data acquired only with the high gain channel, which contains returns belonging to all target classes, i.e., *layers*, *bedrock*, *noise*.

Regarding the quality of data, several preprocessing techniques have been applied in order to obtain improved resolution. In particular, pulse compression and windowing algorithms (e.g., 20% Tuckey window in the time domain, with widening factor $k_t = 1.53$) have been used to improve the range resolution while suppressing the sidelobe level. SAR processing has been applied to improve the along-track resolution and for clutter removal, and multilooking processing (11 looks in the along-track direction and 1 look in the range direction) for despeckling. Also, a minimum variance distortionless response (MVDR) [1] algorithm has been applied to data to suppress clutter contributions coming from the cross-track direction. It is worth noting that all these processing techniques affect the statistical models to be used for modeling the fluctuation of the investigated amplitude radar signal (see Sec. 3.3.1 and Appendix A 3.7).
The parameters of the acquisition systems and the main characteristics of the data are reported in Tab. 3.2. Fig. 3.4 shows the subsurface region R_{ss} of the investigated datasets.

3.5.2 Results of the statistical analysis of the radar signal

In the following, the results of the statistical analysis performed by fitting the Rayleigh, Nakagami, K and Gamma pdfs to the amplitude radar signal are presented. Fig. 3.5 shows

(a)

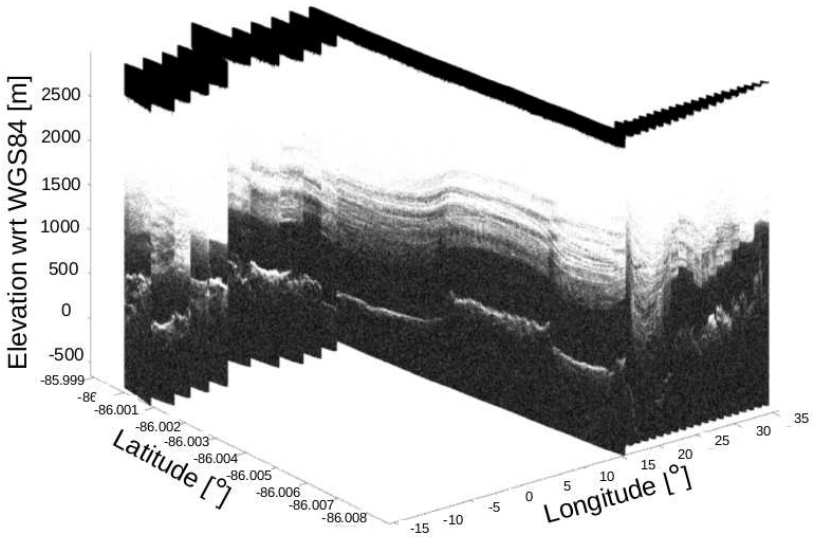

(b)

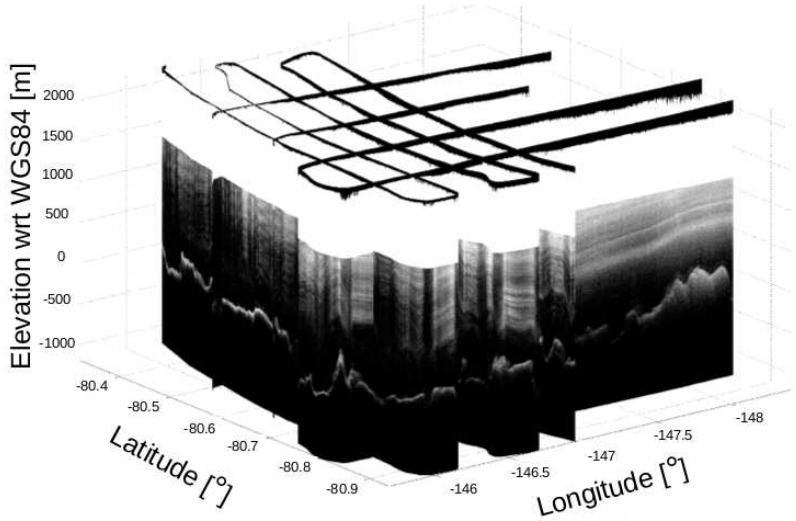

Figure 3.4: Datasets investigated. (a) MCoRDS [$n_S = 410 \times n_T = 27350$], and (b) MCoRDS2 [$n_S = 1200 \times n_T = 17093$]. Values are in dB. The figures are stretched (color adjusted) and vertically exagerated in order to highlight the regions of interest of the subsurface. The upper black region corresponds to the free space above the surface return *surf* (for the MCoRDS2 dataset *surf* is computed using the radargram acquired by the LGC data). The white band in the shallow subsurface (first 285 samples $\simeq$ 798 m below *surf*) of the MCoRDS2 dataset corresponds to the data acquired by the LGC, which is not investigated in our analysis.

Table 3.2: Parameters and characteristics of the investigated datasets.

Parameter	MCoRDS	MCoRDS2
Location	Central Antarctica	Byrd Glacier Antarctica
Platform and altitude (H)	DC-8 @ $H \approx 7000$m	TO @ $H \approx 500$m
Number of radargrams	8	14
Acquisition strategy	sequence	parallel and cross-track
Distance / Area	400 line-km	1000km^2
Central frequency (f_c)	193.9MHz	193.9MHz
Bandwidth (B_w)	9.5MHz	30MHz
Transmitted power (P_{tx})	550W	1050W
Acquisition	14 bit ADC @ 111MHz	14 bit ADC @ 111MHz
Dynamic range	wpl	wpl with LGC and HGC
Range resolution in ice (δ_z^{RS})	13.6m	4.3m
Along-track resolution (δ_x^{RS})	25m	25m
Total number of samples (n_S)	410	1200
Total number of traces (n_T)	27350	17093

Table 3.3: Number of picked samples per class (corresponding to the regions highlighted in Fig. 3.5) used in the statistical analysis.

	Number of picked samples	
Target class	MCoRDS	MCoRDS2
layers	38351	43979
EFZ	12257	16314
bedrock	9321	22710
noise	21381	32754

the regions that have been selected for the analysis from each target class, from a portion of the (a) MCoRDS, and (b) MCoRDS2 datasets. Note that in the figures the values are reported in dB (for visibility), while the statistical analysis has been performed on the normalized amplitude data. Also, note that we considered the *EFZ* class individually (i.e., not merged with the *noise* class). This class has been intentionally selected separately, since another objective in these experiments is to verify also from a statistical point of view the hypothesis on the noisy character of the EFZ (see Sec. 3.2). In order to ensure that the results of the statistical analysis are sufficiently representative, in the fitting process for both datasets we picked a very large number of samples per class (see Tab. 3.3). The fitting performances, which have been evaluated in terms of Kullback-Leibler distance, [76], are reported in Tab. 3.4, in which the best fitting results for each class (which have been derived as defined in Sec. 3.3.1) are highlighted in bold. Such results point out that in almost all the cases, the best fitting model is the Gamma pdf. The

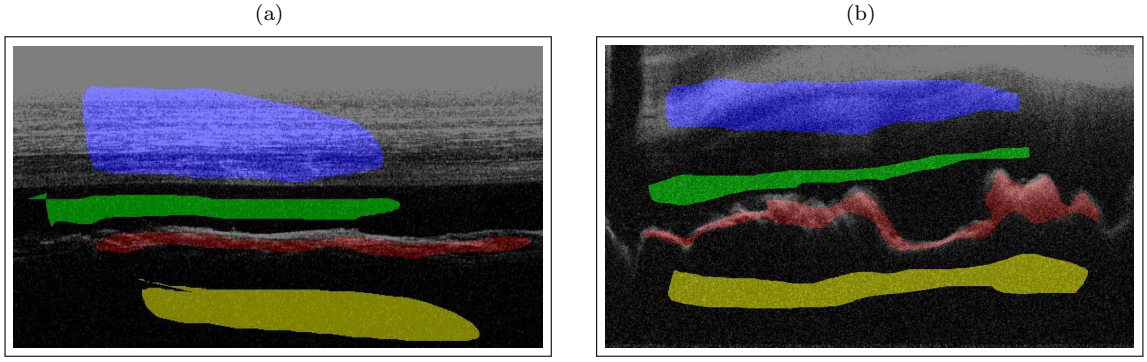

Figure 3.5: Samples picked manually from each target class on a portion of radargram from (a) the MCoRDS dataset, and (b) the MCoRDS2 dataset. In the figures, each color corresponds to a different target class, i.e., blue - *layers*, green - *EFZ*, red - *bedrock*, yellow - *noise*.

exceptions are for the classes *layers* and *bedrock* of the MCoRDS dataset, where the K pdf fits slightly better than the Gamma pdf (difference at the third decimal). However, given the overall very good performances of the Gamma pdf (see also Fig. 3.6) and the fast computation time in estimating its parameters (i.e., two analytical formulas, see (3.15), instead of the iterative approach employed for the K pdf, see (3.13)), in the following, the Gamma pdf is considered as the most suitable fitting model for all classes for both datasets. Note that this is in disagreement with theoretical grounds in radar signal distribution [11] and with the results obtained from applying a similar approach to other RS datasets [33]. For instance, in [11] it is analytically proven that in the regions of no backscattering, e.g., *noise*, the histogram of samples follows a Rayleigh distribution, which is confirmed on a subset of SHARAD radargrams in [33]. However, it is important to recall that our results have been obtained by applying the statistical analysis to data that have been preprocessed (for clutter and sidelobe reduction) and the preprocessing operations changed the data properties with respect to the datasets investigated in other studies. The qualitative results shown in Fig. 3.6 indicate that this preprocessing has changed the original Rayleigh distribution into a distribution that can be better modeled by the Gamma pdf.

It is also worth to analyze the results reported qualitatively in Fig. 3.7, which shows (a) the summary of the fitted Gamma models to all target classes, and (b) the fitted Gamma pdfs to the *noise* and *EFZ* classes. These results refer to the MCoRDS2 dataset, but similar results have been obtained on the MCoRDS dataset. The plot in Fig. 3.7(a) indicates the large difference between the distributions of the *EFZ/noise* and *layers/bedrock* classes, and the very large dynamic range characterizing the radar signal. Fig. 3.7(b) points out the similarity of the two Gamma pdfs modeling the *EFZ* and *noise* samples.

Table 3.4: Fitting performances in terms of Kullback-Leibler distance (dimensionless) of the Rayleigh, Nakagami, K and Gamma distributions to the sample amplitude data for *layers*, *EFZ*, *bedrock* and *noise* classes. The best results (smallest values on each column for each dataset) are highlighted in bold.

		Target class			
Dataset	**Distribution**	layers	EFZ	bedrock	noise
MCoRDS	Rayleigh	0.7097	0.0809	0.6117	0.0815
	Nakagami	0.1395	0.0138	0.3257	0.0127
	K	**0.0212**	0.0974	**0.1442**	0.0990
	Gamma	0.0263	**0.0025**	0.1494	**0.0015**
MCoRDS2	Rayleigh	0.0840	0.1835	0.1433	0.2691
	Nakagami	0.0844	0.0158	0.1357	0.0084
	K	0.0062	0.2095	0.0796	0.2995
	Gamma	**0.0029**	**0.0017**	**0.0578**	**0.0007**

This similarity confirms also from a statistical point of view the validity of the hypothesis that in the EFZ the reflections are buried in thermal noise, therefore very closely matching the noise distribution. For this reason, in the automatic classification of ice subsurface targets, the *EFZ* and *noise* classes are merged within a single no backscattering target class, from now on called *noise*.

3.5.3 Experimental setup

From the considerations made above on the type of data and the scale of the subsurface features, the values of the system parameters selected in our experiments are: $W_x = 14$ and $W_z = 7$ samples, $N_q = 256$ levels and $thr_{KL} = 10$. According to our previous analysis, the Gamma pdf is the best fitting model for all the classes. We therefore extract as features its parameters, i.e., $\theta_{best} = \theta_G = (\alpha_G, \beta_G)$, as explained in Sec. 3.3.3. These are shown along side the amplitude radargrams (which are converted in dB for visibility), the $\mathrm{KL}_{R_{ss}}$ maps, and Ent in Fig. 3.8, for a portion of the MCoRDS dataset at left, and MCoRDS2 dataset at right.

The set of labeled samples for training and testing the SVM was created by defining a reference map of the subsurface. This was done by manually selecting, according to an accurate visual analysis of the radargrams, the regions corresponding to the various target classes. A subset of the reference samples along with the corresponding features are given in input to the SVM classifier for training (we recall that a generic sample $\mathbf{v}$ is characterized by seven features, i.e., $\mathbf{v} = [A, \alpha_G, \beta_G, \mathrm{KL}_{R_{ss}}, Ent, Dist_z, Rel]$). The subset of reference samples is chosen in order to take into account the variability of the subsurface targets in the along-track direction (e.g., at some locations the bedrock is deeper than in

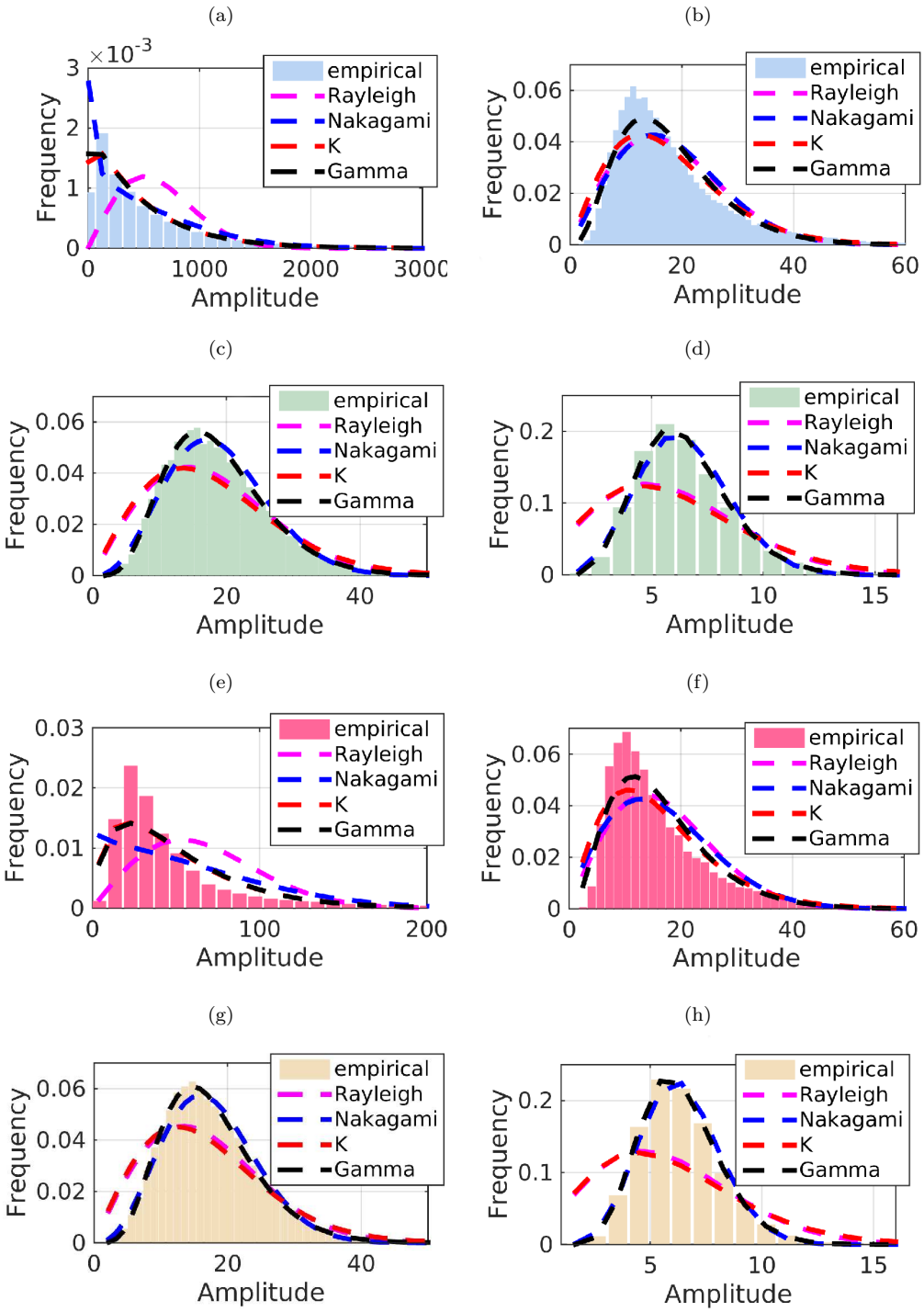

Figure 3.6: Empirical and estimated (with the maximum likelihood technique) distributions for each target class for the (left) MCoRDS, and (right) MCoRDS2 datasets. The color of the (empirical) histograms represent each target class, i.e., blue - *layers*, green - *EFZ*, red - *bedrock*, yellow - *noise*. (a) layers MCoRDS, (b) layers MCoRDS2, (c) EFZ MCoRDS, (d) EFZ MCoRDS2, (e) bedrock MCoRDS, (f) bedrock MCoRDS2, (g) noise MCoRDS, (h) noise MCoRDS2.

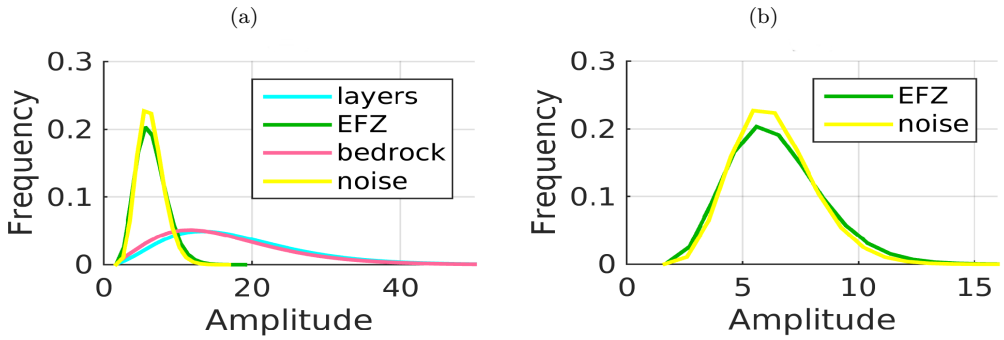

Figure 3.7: Fitted Gamma distributions for (a) all target classes, and (b) the *EFZ* and *noise* classes. Results are shown for the MCoRDS2 dataset.

others). We split the dataset (and the reference map) in N^{tiles} vertical tiles, from which we collect randomly 1% of the samples belonging to each class, to be used in the learning phase. Then, the samples collected from $N_{\Psi}^{tiles} = 2N^{tiles}/3$ tiles are used in a training $k - fold$ *cross-validation* algorithm for selecting the SVM model parameters. In our experiments, we used a Gaussian radial basis function (RBF) kernel for the SVM. This choice is motivated by the fact that the RBF kernel is typically more flexible than the linear kernel and it usually outperforms the polynomial kernel in convergence time [83]. Therefore, the SVM model parameters are the penalty error term ς and the gamma parameter of the RBF kernel, denoted with ϑ. ς and ϑ are tested by performing a grid-search model selection. ϑ is tested between $[10^{-3}..10^{6}]$ with a logarithmic step size, and ϑ is tested with 10 values in logarithmic scale, with central value $\vartheta_c = 1/(2 * \varrho^2)$, where ϱ is the average distance between each pair of classes. Then, for testing the SVM on unknown samples, we chose the values ς_Ω and ϑ_Ω that provided in average (on the kf folds) the highest classification accuracy. The test samples are collected from the remaining $N_{\Omega}^{tiles} = N^{tiles} - N_{\Psi}^{tiles}$ tiles. N^{tiles} is chosen depending on the number of traces n_T available in the considerend dataset, i.e., $N^{tiles} = 99$ for the MCoRDS (with $n_T = 27350$) and $N^{tiles} = 66$ for the MCoRDS2 dataset (with $n_T = 17093$). This implies $N_{\Psi}^{tiles} = 66$ and $N_{\Omega}^{tiles} = 33$ tiles for the MCoRDS dataset, $N_{\Psi}^{tiles} = 44$ and $N_{\Omega}^{tiles} = 22$ tiles for the MCoRDS2 dataset, and a number of traces per tile $n_T^{tile} \in [250..300]$. The number of folds is $kf = 11$. Tab. 3.5 reports the number of samples per class used for the cross-validation and included in the test sets for the MCoRDS and MCoRDS2 datasets.

3.5.4 Classification results

In the following, the analysis of the training (k-fold cross-validation) and test results is given. Tab. 3.6 reports the average error matrix [85] computed after applying the cross-

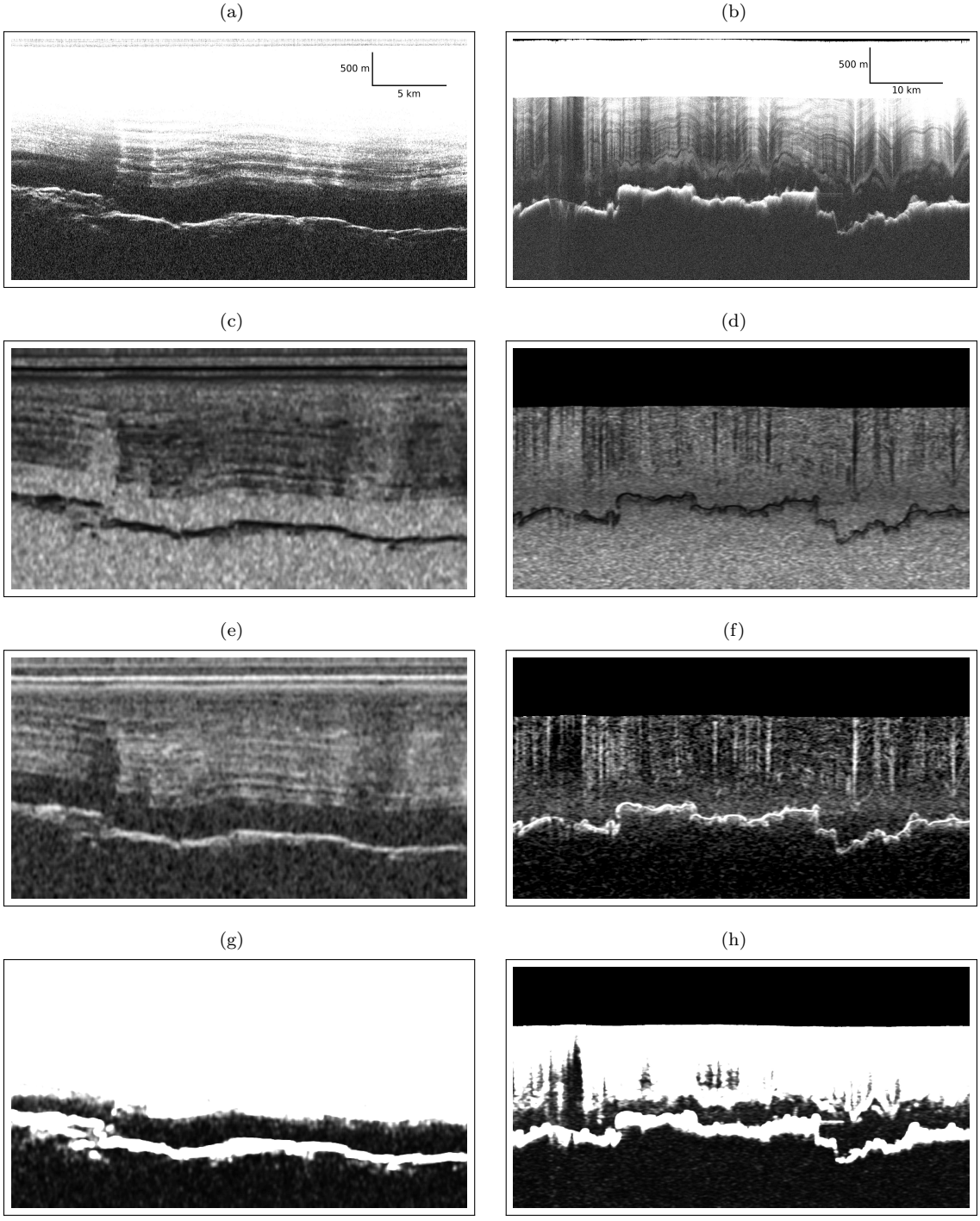

Figure 3.8: Examples of extracted features. The features at the left side of the figure are (a) the radargram, (c) the shape parameter of the Gamma distribution, (e) the Entropy, and (g) the $\mathrm{KL}_{R_{ss}}$ measure on a portion of radargram ($\approx$ 30 line-km) of the MCoRDS dataset. The features at the right side are (b) the radargram, (d) the shape parameter of the Gamma distribution, (f) the Entropy, and (h) the $\mathrm{KL}_{R_{ss}}$ measure on a portion of radargram ($\approx$ 60 line-km) of the MCoRDS2 dataset. The radargrams are in dB, stretched and vertically exagerated to improve visibility.

Table 3.5: Number of reference samples per class used in the cross-validation and test sets.

	Number of reference samples			
	MCoRDS		MCoRDS2	
Target class	cross-validation	test	cross-validation	test
layers	37685	18930	44267	22290
bedrock	18398	7980	13200	6600
noise	23596	12003	39309	19808
Total	n_Ψ=79679	n_Ω=38913	n_Ψ=96776	n_Ω=48698

validation algorithm to $kf = 11$ folds on the MCoRDS dataset. The average accuracy (AA), the corresponding standard deviation (STDEV), the average user accuracy (AUA) and the average producer accuracy (APA) for each class are also reported. The average accuracy values, i.e., AA, AUA and APA, are computed as the mean values of the overall accuracy (OA), user accuracy (UA) and producer accuracy (PA), respectively, calculated on each validation fold. The OA quantifies the overall goodness of the classifier. The UAs represent the percentage of samples correctly labeled in the classification map for each class. The PAs provide for a given class in the reference map, the percentage of samples correctly labeled in the classification map. Tab. 3.7 shows the same information for the MCoRDS2 dataset. The cross-validation algorithm provides $\varsigma_\Omega = 10^6$ and $\vartheta_\Omega = 2.08$ for the MCoRDS dataset, and $\varsigma_\Omega = 10^3$ and $\vartheta_\Omega = 8.88$ for the MCoRDS2 dataset. The error matrices on the test sets along with the correspondent UA, PA and OA are reported in Tab. 3.8 and in Tab. 3.9, for MCoRDS and for MCoRDS2 dataset, respectively.

By analyzing the tables, one can see that the low values of the standard deviation (i.e., 0.41 for MCoRDS and 0.73 for MCoRDS2) confirm the robustness of the presented system to the random choice of the samples used in the kf folds of the cross-validation algorithm. By comparing Tab. 3.6 and Tab. 3.8, one can see that, for the MCoRDS dataset, the AUA and the UA, and the APA and PA, respectively, have similar values. This means that the overall variability of the samples has been well captured in the training phase and proves that the selected SVM model for testing the system capabilities is not biased. The same observations hold for the MCoRDS2 dataset (see Tab. 3.7 and Tab. 3.9). Moreover, we obtained values of OA $> 97\%$ (i.e., 99.09% for MCoRDS and 97.93% for MCoRDS2), which are very satisfactory, especially when considering the type and scale of the investigated targets, the noisy character of the data, and the fact that after training, the system is completely automatic. The effectiveness of the system is also proven by the high values of UA and PA, obtained on both datasets. From the tables one can see that the few errors are mainly due to a wrong classification of some returns at the interfaces between the classes (e.g., 193 out of 7980 bedrock samples and 70 out of 8930 layers samples are labeled as noise samples for the MCoRDS dataset, whereas for the MCoRDS2

Table 3.6: Average (on $kf = 11$) error matrix of the samples of the cross-validation folds (MCoRDS dataset).

		Predicted samples				
		layers	bedrock	noise	Total	APA(%)
Reference samples	layers	3417	0	8	3425	99.75
	bedrock	2	1645	25	1672	98.37
	noise	7	8	2129	2144	99.27
	Total	3426	1653	2162	n_Ψ/kf=7241	
	AUA (%)	99.75	99.54	98.54	AA=99.28% STDEV=0.41	

dataset 219 and 109 noise samples out of 19808 are labeled as layers and bedrock samples, respectively). Such errors are mainly caused by the sliding window approach. Due to its intrinsic low pass filtering effect, in the layers and bedrock regions, it tends to slightly overestimate the areas with high backscattering and to underestimate the areas with low backscattering (where the signal amplitude is close to the measured background noise). These effects can be seen in the final classification maps in Fig. 3.9 for the MCoRDS dataset and in Fig. 3.10 for the MCoRDS2 dataset. For a better understanding, they are also highlighted in Fig. 3.11(d). On the other hand, it is important to note that in the regions characterized by deep and strongly scattering layers followed in range by the absence of bedrock returns (see an example of such radargram in Fig. 3.11(a)), the classifier is able to perform an accurate classification (see Fig. 3.11(b)). In such cases, the classifier mostly relies on the relational feature, which, by integrating both the knowledge of the radar signal statistical properties and the position in the range direction of the subsurface targets, is generally able to correctly discriminate the samples. The importance and effectiveness of the relational feature in our classification problem has been confirmed by the unsatisfactory results obtained in initial experiments in which the relational feature has been omitted from the set of extracted features used in the learning phase (i.e., $\mathbf{v} = [A, \alpha_G, \beta_G, \mathrm{KL}_{R_{ss}}, Ent, Dist_z]$). In particular, we obtained a lower overall accuracy and poor quality classification maps. An example of such classification map is shown in Fig. 3.11(c). By comparing this map with that obtained by using all the features (i.e., $\mathbf{v} = [A, \alpha_G, \beta_G, \mathrm{KL}_{R_{ss}}, Ent, Dist_z, Rel]$, see Fig. 3.11(b)), one can easily understand the effectiveness of the proposed relational feature.

Table 3.7: Average (on $kf = 11$) error matrix of the samples of the cross-validation folds (MCoRDS2 dataset).

		Predicted samples				
		layers	bedrock	noise	Total	APA(%)
Reference samples	layers	3958	6	61	4025	98.35
	bedrock	7	1127	66	1200	94.95
	noise	51	20	3502	3573	98.01
	Total	4016	1153	3629	n_Ψ/kf=8798	
	AUA (%)	98.55	97.78	96.51	AA=97.60% STDEV=0.73	

Table 3.8: Error matrix on the test samples (MCoRDS dataset).

		Predicted samples				
		layers	bedrock	noise	Total	PA(%)
Reference samples	layers	18839	21	70	18930	99.51
	bedrock	5	7782	193	7980	97.51
	noise	17	46	11940	12003	99.48
	Total	18861	7849	12203	n_Ω=38913	
	UA (%)	99.88	99.15	97.84	OA=99.09%	

Table 3.9: Error matrix on the test samples (MCoRDS2 dataset).

		Predicted samples				
		layers	bedrock	noise	Total	PA(%)
Reference samples	layers	21918	15	357	22290	98.33
	bedrock	17	6290	293	6600	95.30
	noise	219	109	19480	19808	98.34
	Total	22154	6414	20130	n_Ω=48698	
	UA (%)	98.93	98.07	96.77	OA=97.93%	

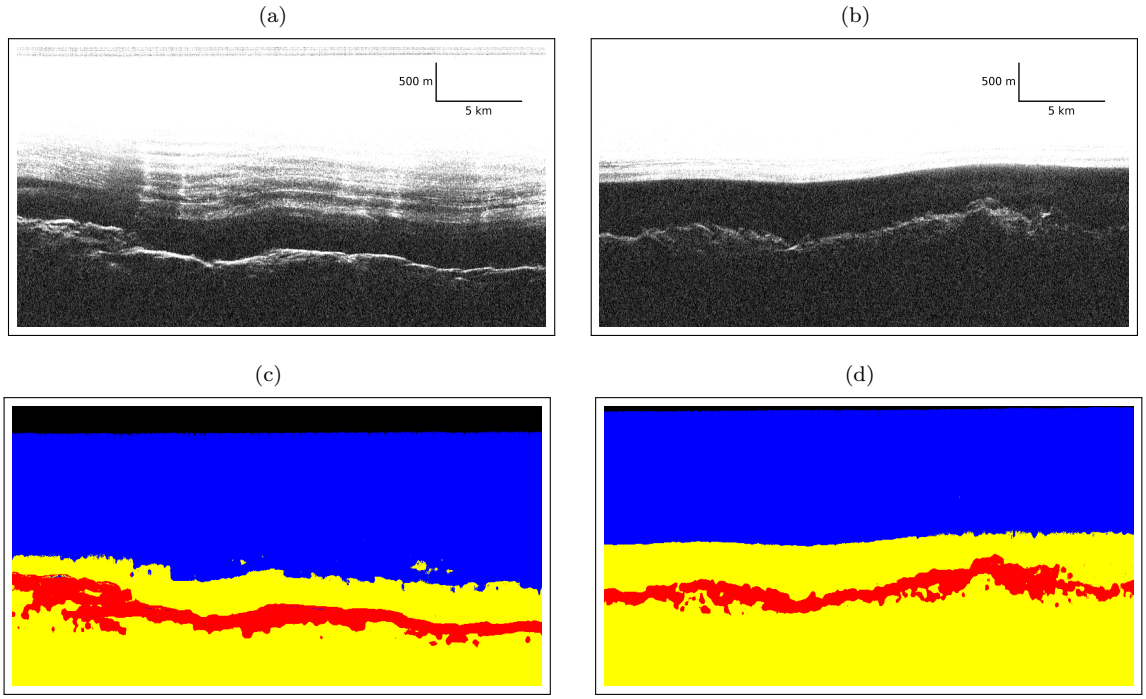

Figure 3.9: Examples of (a) and (b) radargrams, and (c) and (d) corresponding classification maps generated with the presented algorithm (MCoRDS dataset). The radargrams are in dB, stretched and vertically exagerated to improve visibility. In the classification maps, each color represents a different target class, i.e., black - *free space*, blue - *layers*, red - *bedrock*, yellow - *noise*.

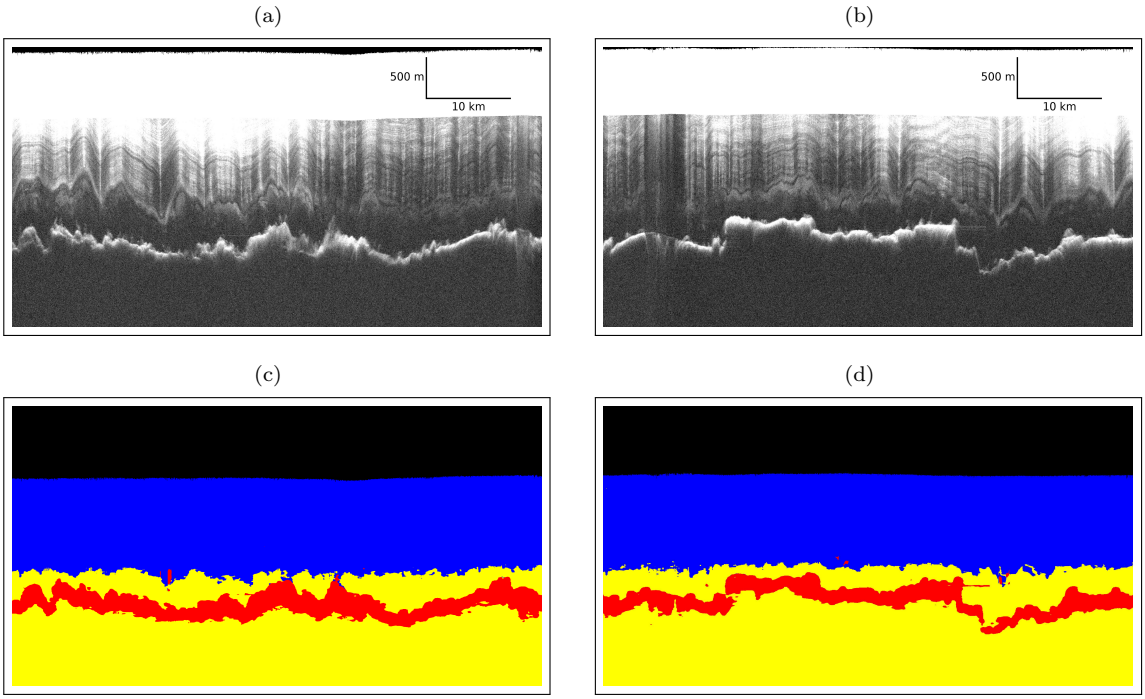

Figure 3.10: Examples of (a) and (b) radargrams, and (c) and (d) corresponding classification maps generated with the presented algorithm (MCoRDS2 dataset). The radargrams are in dB, stretched and vertically exagerated to improve visibility. In the classification maps, each color represents a different target class, i.e., black - *free space*, blue - *layers*, red - *bedrock*, yellow - *noise*.

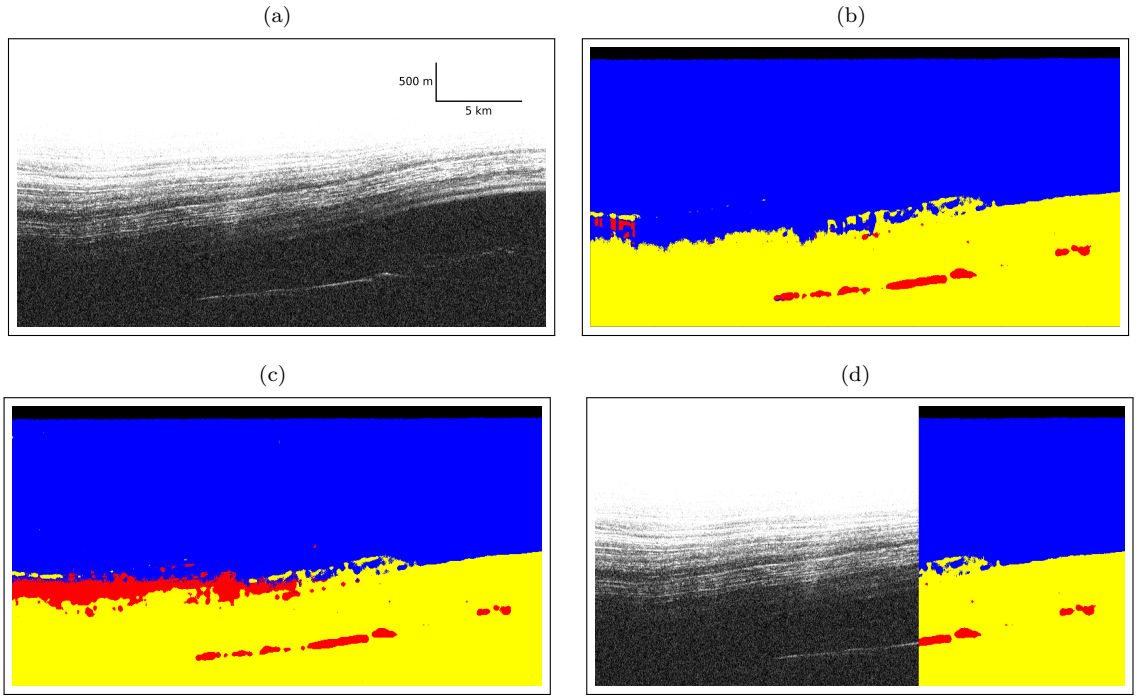

Figure 3.11: Example of (a) radargram (MCoRDS dataset) showing a particular subsurface pattern, i.e., deep and strong backscattering layers and partially missing bedrock area, (b) corresponding classification map obtained by training the SVM with all the features presented in this work (i.e., the vector $\mathbf{v} = \{A, \alpha_G, \beta_G, \mathrm{KL}_{R_{ss}}, Ent, Dist_z, Rel\}$), (c) corresponding classification map obtained by training the SVM with a subset of the presented features, i.e., which does not contain the relational feature *Rel* (i.e., $\mathbf{v} = \{A, \alpha_G, \beta_G, \mathrm{KL}_{R_{ss}}, Ent, Dist_z\}$), and (d) portions of radargram and classification map highlighting the effect of the sliding window approach; the low-pass filtering effect results in a slight underestimation and overestimation of the layers and bedrock classes, respectively, at their interfaces with the noise region. The radargrams are in dB, stretched and vertically exagerated to improve visibility. In the classification maps, each color represents a different target class, i.e., black - *free space*, blue - *layers*, red - *bedrock*, yellow - *noise*.

(a)

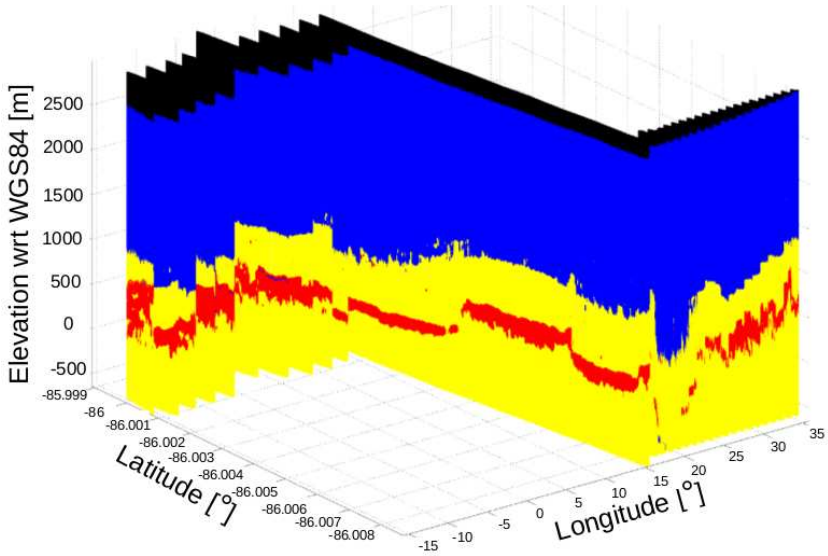

(b)

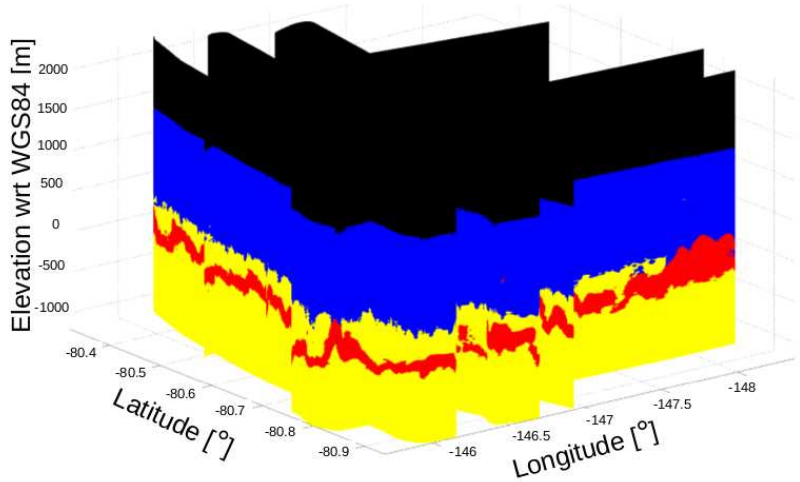

Figure 3.12: Classification maps corresponding to (a) the MCoRDS dataset (radargrams in dB shown in Fig. 3.4(a)), and (b) the MCoRDS2 dataset (radargrams in dB shown in Fig. 3.4(b)). In the classification maps, each color represents a different target class, i.e., black - *free space*, blue - *layers*, red - *bedrock*, yellow - *noise*.

3.5.5 Analysis of the computational load

From a computational point of view, an important characteristic of the presented system is its ability to process in a fast way a large amount of data. This is due to the fact that the algorithms included in the system can be parallelized. Thus, it is possible to take advantage of the latest technology (e.g., clusters of large-storage and high-power computers (cpus)) in order to faster achieve the desired performances. The feature extraction and the training of the classifier can be easily split into several subtasks to be given to different cpus that can run in parallel. Given that the features are computed with a sliding window approach (which is characterized by the fact that the computations within the windows are independent), one can use a cluster of cpus to perform such computations in parallel. In the grid-search selection of the SVM model parameters with the cross-validation algorithm, both the operations within each cross-validation fold and the computations at each intersection point of the grid are independent. This enables parallelizing the algorithm also in the training phase of the classifier, which otherwise has a time complexity in the order of $O(n_{\Psi}^3)$ [86]. Moreover, the feature extraction and the training of the classifier are operations that can be computed only once, in offline mode. Once the SVM model has been selected, the only online/real-time operation is the classification of new samples, which can also be performed by several cpus in parallel. In our experiments, the computational capabilities of the presented system have been proven by using a cluster of 192 cpus (@2.05 GHz) which performed all the operations per dataset in ≈ 5 hours. This is a reasonable computation time if we consider the very large amount of data that has been processed. Moreover, note that the offline computations (feature extraction and SVM training with cross-validation) require about 98% of this amount of time, while the generation of the classification maps for the whole datasets (after the training phase) require only few minutes. In general, we expect to require a new training of the classifier only when either the acquisition mode or the pre-processing phase of the data are changed. Another advantage of the presented system is the fact that it can be easily tuned for analyzing different RS datasets, since it involves a small number of parameters in the overall classification algorithm (i.e., W_x, W_z, thr_{KL}).

3.6 Conclusion

In this Chapter, as a first contribution of the thesis on the problem of ice subsurface target identification, we have proposed a novel system for the automatic classification of ice sheet subsurface targets. The system relies on advanced image processing and machine learning techniques to efficiently extract the information contained in radargrams. The presented system is made up of two main components, i.e., i) feature extraction and ii)

automatic classification based on SVM. The feature extraction for ice sheet subsurface target description is the main component of the system, which also represents one of the main contributions of this work. The features extracted take into account both the statistical properties of the measured radar signal and the spatial properties of the subsurface targets. Along with the original amplitude data, several features have been identified and extracted, i.e., the parameters of the best fitting model, the entropy, the Kullback-Leibler distance, the range position of the ice subsurface targets and the relational feature. The extracted features have been given as input to an automatic classifier based on SVM to obtain the final classification maps.

The main characteristics of the presented system are: i) robustness and/or adaptiveness to the heterogeneity of radargrams as a consequence of the features used and the learning approach employed; ii) capability to obtain objective and quantitative results on large amount of data; and iii) capability to process large archives of data due to the computational efficiency and the possibility of parallelizing the algorithms it is made of. These have been proven by applying the algorithm to two real-world datasets acquired by the MCoRDS instrument operated with different parameters (i.e., bandwidth) in different regions of Antarctica. For both datasets, covering $\approx$ 400 line-km, the system provided in few hours ($\approx$ 5 hours per dataset) high quality classification maps with an overall accuracy greater than 97%. This is a very satisfactory result, considering the type and scale of the investigated targets, the noisy character of the radar data, and the fact that the algorithm is nearly completely automatic. More precisely, the system requires a minimum amount of user interaction in the training phase of the classifier, wheareas in the operational phase (classification of new data), it is completely automatic.

The output of the system can be used for estimating the extent of the subsurface targets both in the range and along-track directions (e.g., ice layered area thickness, bedrock scattering area distribution). Furthermore, when the spatial sampling allows it (e.g., sufficiently dense grid of tracks followed by the instrument), such output can be used along with appropriate RS data integration techniques (e.g., based on standard interpolation algorithms) for generating 3D models of the subsurface, useful for the estimation of the ice subsurface targets in all dimensions. This can also help to detect critical basal boundary conditions and study changing archeology or geology. Therefore, the automatic classification of the subsurface targets is an initial essential step for the further development of more elaborate analyses of the ice sheet subsurface.

As future work, we aim to use the output classification maps, in particular at the traces (and neighborhoods) where more tracks overlap, for defining a reliable postprocessing technique for removing outliers and finally assessing a unique solution at the corresponding lat-long coordinates in the range direction. Another objective is to check the applicability

of the system to radargrams acquired in Greenland. Also, we aim to study the possibility to tune the presented system in order to adapt it to the detection of subsurface targets visible in radargrams acquired in other icy regions (e.g., glaciers).

3.7 Appendix A

In this Appendix, the theoretical distributions used in the statistical analysis of the radar signal are briefly described:

– The analytical equation of the Rayleigh pdf is given by:

$$R_{pdf}(A) = \frac{2A}{\mu_{A^2}} \exp\left[-\frac{A^2}{\mu_{A^2}}\right], \tag{3.8}$$

where the parameter of the distribution μ_{A^2} is the mean power of the signal and can be estimated using the Maximum Likelihood Estimation (MLE) approach as:

$$\tilde{\mu}_{A^2} = E\left\{A^2\right\}, \tag{3.9}$$

with $E\{\cdot\}$ denoting the expectation operation.

– The analytical equation of the Nakagami pdf is given by:

$$N_{pdf}(A) = 2\left(\frac{\beta_N}{\mu_{A^2}}\right)^{\beta_N} \frac{A^{2\beta_N-1}}{\aleph(\beta_N)} \exp\left[-\frac{\beta_N A^2}{\mu_{A^2}}\right], \tag{3.10}$$

where $\aleph(\cdot)$ denotes the Gamma function. The estimation of the mean power μ_{A^2} can be done with the MLE approach as explained previously for the Rayleigh distribution, while the shape parameter β_N can be estimated by using the estimator presented in [87], i.e.,

$$\tilde{\beta}_N = \begin{cases} \frac{(0.5000876+0.1648852y-0.0544274y^2)}{2}, \\ \quad \text{if } 0 < y < 0.5772 \\ \frac{8.98919+9.059950y+0.9775373y^2}{y(17.79728+11.968477y+y^2)}, \\ \quad \text{if } 0.5772 < y < 17 \end{cases} \tag{3.11}$$

where $y = \ln\left(\frac{\tilde{\mu}_{A^2}}{F}\right)$ and $F = \left(\prod_{i=1}^{n} {A_i}^2\right)^{\frac{1}{n}}$, and n is the number of samples considered in the estimation.

– The analytical equation of the K pdf is given by:

$$K_{pdf}(A) = \frac{4}{\aleph(\mu_{A^2})}\left(\frac{\beta_K}{\mu_{A^2}}\right)^{\frac{\beta_K+1}{2}} A^{\beta_K} B_{\beta_K-1}\left[2A\sqrt{\frac{\beta_K}{\mu_{A^2}}}\right], \tag{3.12}$$

where $B_{\beta_K-1}(\cdot)$ is the modified Bessel function of the second kind of order β_K-1. The parameters of the K pdf can be estimated with the MLE by maximizing the logarithm of the likelihood function $l_n(\beta_K, \mu_{A^2}; \forall A_i, i \in [1..n])$ of the K distribution [76], i.e.,

$$(\tilde{\beta}_K, \tilde{\mu}_{A^2}) = \underset{(\beta_K, \mu_{A^2})}{\arg\max} \ln [l_n], \tag{3.13}$$

where $\ln(\cdot)$ is the natural logarithm function.

– The analytical equation of the Gamma pdf is given by:

$$G_{pdf}(A) = \left(\frac{A}{\alpha_G}\right)^{\beta_G-1} \cdot \frac{e^{-\frac{A}{\alpha_G}}}{\alpha_G \aleph(\beta_G)}. \tag{3.14}$$

The values of the scale $\tilde{\alpha}_G$ and shape $\tilde{\beta}_G$ parameters of the Gamma distribution can be estimated using the MLE as solutions of the simultaneous equations [75]:

$$\begin{cases} \hat{\alpha}_G = \frac{\bar{A}}{\hat{\beta}_G}, \\ \log(\hat{\beta}_G) - \Xi(\hat{\beta}_G) = \log [\bar{A}/(\prod_{i=1}^{n} A_i)^{1/n}], \end{cases} \tag{3.15}$$

where $\Xi(\cdot)$ is the di-gamma function and $\bar{A} = E\{A\}$.

Chapter 4

A Model-Based Technique for the Automatic Detection of Earth Continental Ice Subsurface Targets in Radar Sounder Data

This Chapter[1] *provides a second contribution to the identification of ice subsurface features in RS data. In particular, we propose an automatic technique for a large scale detection of the ice subsurface targets and the estimation of their properties (e.g., layered area thickness, bedrock scattering area) from radargrams acquired by RS operated at the Earth continental polar caps. Unlike the method described in the previous Chapter, which is based on a supervised learning algorithm, the model-based technique which we present in this Chapter is unsupervised. It uses the parameters of the RS acquisition system combined with the output of an automatic image segmentation algorithm. The segmentation operation is applied to the radargrams after a preliminary processing phase aimed to emphasize the relevant subsurface targets. The segmentation criterion considers the radar signal backscattering properties and a model of the spatial distribution of the investigated targets that takes into account the effects of the wave propagation through the subsurface. Experimental results obtained on real radargrams acquired by an airborne RS in Antarctica confirm the efficiency of the proposed technique.*

[1] Part of this chapter appears in:

[88] Ilisei, A.-M. and Bruzzone, L., "A Model-Based Technique for the Automatic Detection of Earth Continental Ice Subsurface Targets in Radar Sounder Data," in *IEEE Geoscience and Remote Sensing Letters*, Vol. 11, No. 11, pp. 1911-1915, 2014.

4.1 Introduction

As already mentioned in the previous chapters, the automatic analysis of radargrams of the ice sheet is essential for an efficient usage of the available RS data in order to better understand the ice subsurface structure. However, the review of the related literature (see Sec. 2.1) points out that the development of automatic techniques for the analysis of RS data has not been sufficiently addressed.

In this Chapter we contribute to the related state of the art with a second approach to the identification of ice subsurface features. In particular, we propose a novel unsupervised technique for the automatic detection of ice subsurface targets and the estimation of their properties, which can guarantee quantitative and large scale analysis of radargrams. The proposed technique relies on the knowledge of the statistical properties of the radar signal and the spatial distribution of the subsurface targets. In order to understand the radar signal fluctuations, a preliminary statistical analysis of the radar signals is carried out. Based on such an analysis, the technique generates a statistical map which is afterwards segmented into homogeneous regions corresponding to the different types of targets. The segmentation criterion involves the strength of the signal with respect to noise and a model of the spatial distribution of the subsurface targets (which considers the effects of the wave propagation through the material). The segmentation enables the automatic identification of both the layers and bedrock scattering areas and thus the analysis of their properties. The effectiveness of the proposed technique has been confirmed by results obtained by applying the algorithm to MCoRDS data acquired in Antarctica [62].

The rest of this Chapter is organized as follows. In Sec. 4.2 we present the details of the proposed technique. Experimental results obtained on a real dataset acquired in Antarctica are reported in Sec. 4.3. Finally, Sec. 4.4 discusses the capabilities and limitations of the proposed technique and proposes future developments of this work.

4.2 Detection and estimation of ice subsurface targets properties

The goal of this work is to develop an efficient technique for the automatic analysis of radargrams, in particular for the detection and properties estimation of the different ice subsurface targets commonly visible in airborne RS data. The architecture of the proposed technique is shown in Fig. 4.1 and consists of four main blocks: 1) data preprocessing (radargram alignment), 2) statistical map generation, 3) statistical map thresholding, and 4) layered and bedrock scattering areas detection. The blocks of the proposed scheme

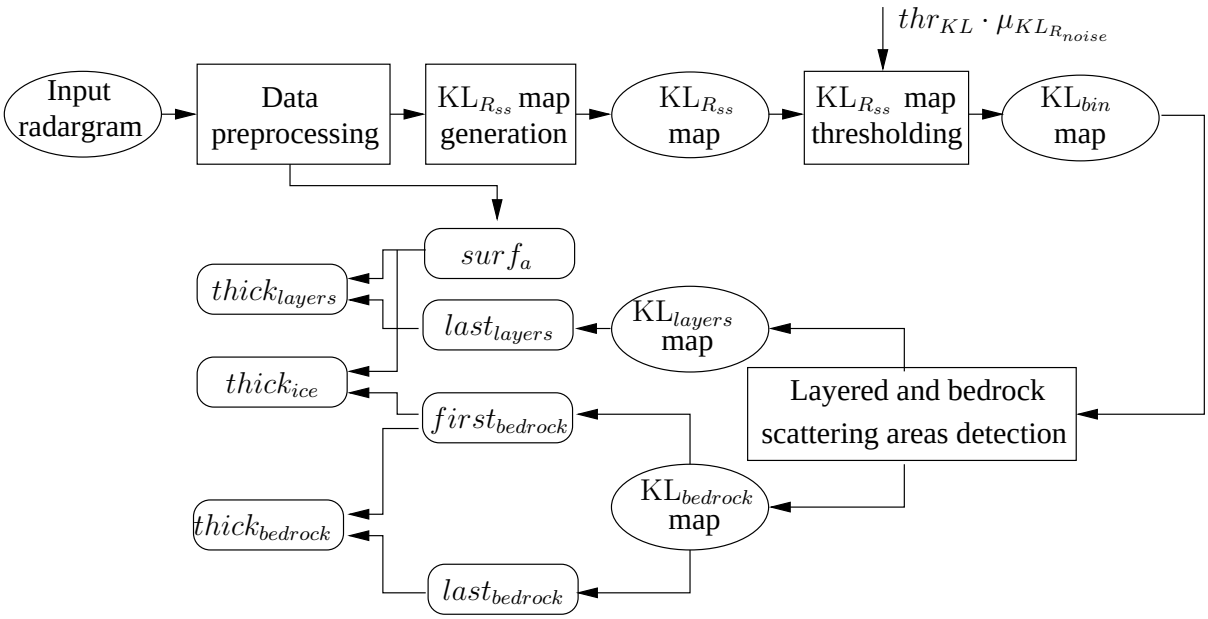

Figure 4.1: Block scheme of the proposed technique.

are detailed in the following subsections, after the description of the model of a typical radargram acquired at the continental polar caps. This model is useful for understanding the types of investigated targets and drives the development of the proposed algorithm.

4.2.1 Radargram model

As already mentioned in the introduction of the thesis, a radargram is a 2D matrix showing the cross-section of the ice subsurface. The method in this chapter relies on the ice sheet subsurface radargram model introduced in Sec. 3.2 and depicted in Fig. 3.1. Recall that the ice subsurface targets are i) *layers* of ice that are spatially coherent englacial surfaces, ii) the *bedrock* scattering area, which represents the portion below the ice/bedrock interface within which the backscattered wave has still sufficient power to be measured, and iii) *noise* regions characterized by the absence of scatterers, which are present above and below the bedrock. Note that discontinuities can be present in the bedrock scattering area shown in radargrams (see trace t_{nbr} in Fig. 3.1). This is not consistent with the real situation in which the bedrock under the ice column is expected to be continuous. The reason for this discontinuity is either the loss of power through the ice column or the preprocessing of the radargrams (e.g., which does not completely remove the surface clutter). The noise region located below the bedrock is due to strong attenuation through the subsurface which makes it impossible to acquire coherent returns. Therefore, at the corresponding depth the RS mainly measures noise. According to recent studies [30], the noise region located above the bedrock, also called echo free zone (EFZ),

is a consequence of the lack of coherent reflecting surfaces due to the layer disturbances caused by the ice flow at the basal interface. It is worth mentioning here that the main assumption considered in the development of our technique is the presence of the EFZ. This is a reasonable hypothesis as the EFZ is present in extended areas of Antarctica and Greenland [30].

4.2.2 Data preprocessing

The instability of the platform that carries the RS introduces errors in the radargram acquisition process, which must be corrected in order to perform accurate analyses of the subsurface targets. These errors are mainly due to the variable height of the platform, which causes the surface and subsurface returns recorded in radargram to appear at range positions that do not correspond to the real air/ice surface and subsurface. In order to correct these displacements, we apply to the radargram a sequence of standard preprocessing steps that consist in a shift in range of the traces of the original radargram. This operation generates a corrected/aligned radargram. Notice that the aligned radargram can be partitioned in two main regions, the subsurface region R_{ss} that contains all the target classes of interest (i.e., layers, bedrock, noise) and a region R_{noise} at the bottom of the radargrams that contains exclusively noise measurements. In this step we separate the two regions at a reference depth of 3500m, below which in the investigated radargrams there is no target backscattering along the whole azimuth track. The referece depth is computed considering a constant dielectric constant of ice $\varepsilon^{ice} = 3.15$. In the following, in order to speed-up the processing, we will focus the analysis on the R_{ss} region.

4.2.3 Proposed technique

The ice subsurface target properties to be estimated by the proposed technique are: the layer thickness zone $thick_{layers}$ [m] (see (4.1)), the ice column extension $thick_{ice}$ [m] (which contains both the layer thickness zone and the EFZ) (see (4.2)) and the bedrock scattering area extension $thick_{bedrock}$ [m] (see (4.3)). Note that the technique is trace-based and $thick_{ice}$ can be computed only for the traces $t \neq t_{nbr}$, where t_{nbr} indicates the traces with no bedrock returns (see Fig. 3.1). These properties are estimated as follows:

$$thick_{layers}(t) = [last_{layers}(t) - surf(t)] \cdot d_{ss}, \forall t, \tag{4.1}$$

$$thick_{ice}(t) = [first_{bedrock}(t) - surf(t)] \cdot d_{ss}, \forall t \neq t_{nbr}, \tag{4.2}$$

$$thick_{bedrock}(t) = \begin{cases} [last_{bedrock}(t) - first_{bedrock}(t)] \cdot d_{ss}, \forall t \neq t_{nbr}, \\ 0, \qquad\qquad \forall t = t_{nbr}, \end{cases} \tag{4.3}$$

where $d_{ss} = c/(2 \cdot f_r \cdot \sqrt{\varepsilon^{ice}})$ is the length of the pixel in the range direction in the subsurface region (with f_r denoting the range sampling frequency), $last_{layers}(t)$ represents the last return of the layered scattering area, and $first_{bedrock}(t)$ and $last_{bedrock}(t)$ are the first and the last returns of the bedrock, respectively, on the t-th trace of the radargram. The borderlines $last_{layers}$, $first_{bedrock}$ and $last_{bedrock}$ are identified by combining the knowledge of the strength of the radar signal with an image segmentation technique that we apply to a statistical map of the subsurface, as explained in the following subsections.

Statistical map generation

In order to detect the ice subsurface targets we define a segmentation algorithm that can divide the subsurface region R_{ss} into the three investigated target classes, i.e., *layers*, *bedrock* and *noise*. Given that the radar signals are typically very noisy, we apply the segmentation algorithm to a processed version of the aligned radargram, which we call statistical $\mathrm{KL}_{R_{ss}}$ map. The $\mathrm{KL}_{R_{ss}}$ has been calculated with a sliding window approach as described in Sec. 3.3.3, after a detailed statistical analysis of the radar signal, which has been performed as explained in Sec. 3.3.1. In more details, the $\mathrm{KL}_{R_{ss}}$ map is generated by applying to the R_{ss} region the Kullback-Leibler (KL) divergence [76], which computes the local statistical difference between two distributions. The KL distance is computed between the distribution of the amplitude samples $\mathcal{H}$ inside windows of size $W_z \times W_x$ (range $\times$ azimuth) and the theoretical distribution of the noise $\mathcal{M}$, as in (3.1). $\mathcal{M}$ has been estimated by considering exclusively noise samples, i.e., samples drawn from the bottom part R_{noise} of the radargram (below 3500m), which is free of target returns and acquisition artifacts (e.g., closure of the acquisition window, double bounce returns of the wave with the surface and platform). As derived in Sec. 3.5.2, the noise samples are better modeled by the Gamma theoretical model (see (3.14)) which is characterized by the parameters scale α_G and shape β_G estimated with (3.15). Thus, $\mathcal{M} = G_{pdf}$. The resulting $\mathrm{KL}_{R_{ss}}$ map is of particular interest as it highlights the most scatterable targets, i.e., whose strength is noticeably higher than that of the noise. This characteristic is going to be considered in the thresholding step. Note that if the input radargram has not been preprocessed for surface clutter return suppression, the $\mathrm{KL}_{R_{ss}}$ map also highlights artifacts due to possible clutter returns [33]. Therefore, a postprocessing step is required to remove clutter.

Statistical map thresholding

The objective in this step is to extract the regions of the $\mathrm{KL}_{R_{ss}}$ map that have high backscattering, i.e., *layers* and *bedrock*, and to distinguish them from the areas that have low backscattering (only *noise*). To achieve this, we threshold the $\mathrm{KL}_{R_{ss}}$ map on the basis of the mean $\mu_{\mathrm{KL}_{R_{noise}}}$ of the samples of the $\mathrm{KL}_{R_{noise}}$ (which has been generated by applying (3.1) to R_{noise}). This is done as in (3.4), where thr_{KL} is a user defined threshold that controls the degree of similarity between the samples of $\mathrm{KL}_{R_{ss}}$ map and those of $\mathrm{KL}_{R_{noise}}$ map, and KL_{bin} is the binary map (obtained by thresholding the $\mathrm{KL}_{R_{ss}}$ map) that points out the returns corresponding to the *layers* and *bedrock* scattering areas.

Layered and bedrock scattering area detection

The aim of this step is to distinguish the returns of the *layers* from those of the *bedrock* region in the KL_{bin} map. In order to perform this operation, we consider the assumption of the presence of the EFZ in the aligned radargram, and implicitly in the $\mathrm{KL}_{R_{ss}}$ and KL_{bin} maps. Therefore, we take into account the spatial distribution of the subsurface targets and their relational properties, i.e., the expected order of the ice subsurface targets in the range direction: *layers*, *noise* (EFZ), *bedrock* and *noise*. According to this hypothesis, the KL_{bin} map is composed of at least two main disjunct regions, separated by the EFZ, where the one just below the surface $surf$ represents the *layers*, and the remaining represent the *bedrock* returns (see Fig. 3.1). It follows that the region of KL_{bin} map that intersects $surf$ contains the returns of the layers (which we represent in the KL_{layers} map), while the remaining regions with value "1" contain only *bedrock* returns (which we represent in the $\mathrm{KL}_{bedrock}$ map).
At this point, the traces with no bedrock returns t_{nbr} are those for which there is no value of "1" on the $\mathrm{KL}_{bedrock}$ map. For all other traces $t \neq t_{nbr}$, the first return of the bedrock $first_{bedrock}(t)$ is detected as the position of the first "1" encountered by moving downwards over the traces of the $\mathrm{KL}_{bedrock}$ map, i.e.,

$$first_{bedrock}(t) = \arg\min_i\{\mathrm{KL}_{bedrock}(i,t) = 1\}, \forall t \neq t_{nbr}. \tag{4.4}$$

Similarly, the last return of the bedrock $last_{bedrock}$ (see (4.5)) and of the layers $last_{layers}$ (see (4.6)) are detected as the position of the first "1" found by moving upwards over the traces of the $\mathrm{KL}_{bedrock}$ map and KL_{layers} map, respectively.

$$last_{bedrock}(t) = \arg\max_i\{\mathrm{KL}_{bedrock}(i,t) = 1\}, \forall t \neq t_{nbr}, \tag{4.5}$$

$$last_{layers}(t) = \arg\max_i\{\mathrm{KL}_{layers}(i,t) = 1\}, \forall t. \tag{4.6}$$

It is worth noting that on the traces with no bedrock returns t_{nbr}, the computation of bedrock thickness provides $thick_{bedrock}(t_{nbr}) = 0$ (see (4.3)). Moreover, the EFZ and implicitly the ice thickness $thick_{ice}(t_{nbr})$ (see (4.2)) cannot be reliably computed. Note that this is not a limitation of the proposed technique, but rather a consequence of the lack of information in the radargram. Approximate values of $thick_{ice}(t_{nbr})$ could be estimated by considering further assumptions (e.g., in the real scenario the bedrock is expected to be continuous) and using the detected borderlines at the nearest adjacent traces $t \neq t_{nbr}$.

4.3 Experimental results

We applied the proposed unsupervised model-based technique to a dataset made up of 8 MCoRDS radargrams acquired in sequence over an extension of about 400 km in Antarctica [62]. The data are compressed in azimuth with a SAR procedure (for azimuth resolution improvement) and processed the MVDR technique (for clutter return suppression) [1]. The resolution of the radargram is 13m in range, 25m in azimuth and 70m in the across-track direction. The range sampling frequency of the instrument is $f_r = 9.5$MHz, implying $d_{ss} = 8.9$m.

Since the MCoRDS dataset is composed of radargrams acquired in sequence, in order to align the traces of the radargrams with respect to a single reference trace and to use the information at the lateral borders of the radargrams, we created an extended radargram by appending all the 8 radargrams. We applied the preprocessing steps detailed in Sec. 4.2.2 to the extended radargram. Thus we obtained an aligned radargram showing the R_{ss} regions, which has a size $[n_S = 410 \times n_T = 27350]$. Fig. 4.1(a) shows a portion $[410 \times 3500]$ of the aligned radargram. The corresponding statistical $\mathrm{KL}_{R_{ss}}$ map generated with the algorithm presented in Sec. 4.2.3 is shown in Fig. 4.1(b). The size of the sliding window used in the computation of the related $\mathrm{KL}_{R_{ss}}$ statistical map has been chosen by considering the spatial distribution of the subsurface targets, which are mostly extended in the azimuth direction and present sharper variations in the range direction. To account for these variations, we set $W_z = 7$ and $W_x = 14$ samples. For the segmentation of the statistical map we considered values of the threshold $thr_{\mathrm{KL}} > 0$. The choice of such value strongly affects the output of the thresholding operation. Indeed, thr_{KL} defines the boundary on the degree of similarity between the samples with high backscattering and samples of noise. Too high values of thr_{KL} may lead to identify samples belonging to high backscattering areas as noise samples, whereas too low values of thr_{KL} may lead to confuse high backscattering samples in the noise regions with *layers* or *bedrock* returns. Fig. 4.1(c) shows the corresponding KL_{bin} map generated with the proposed algorithm when $thr_{\mathrm{KL}} = 10$. Fig. 4.1(d) shows the position of the $last_{layers}$, $first_{bedrock}$ and $last_{bedrock}$

borderlines detected with the proposed algorithm, for the portion of radargram shown in Fig. 4.1(a). The output of the proposed algorithm on other three portions of the aligned radargram is provided in Fig. 4.3.

Table 4.1: Accuracy provided by the proposed technique for the detection of layers and bedrock scattering areas.

Target class	Target samples	Missed alarms	% Missed alarms	Non-target samples	False alarms	% False alarms	Total error	% Total error
layers	111946	1074	0.96	88054	923	1.05	1997	0.99
bedrock	11615	2120	18.25	188385	1344	0.71	3464	1.73

From a quantitative point of view, since no ground truth data are available for our detection problem, in order to validate the proposed algorithm we created by visual interpretation a reference map of the ice subsurface (i.e., accurate masks of the investigated target classes), from which we picked randomly 200000 samples (111946 samples of *layers*, 11615 samples of *bedrock* and 76439 samples of *noise*). Tab. 4.1 reports the accuracy in the detection of *layers* and *bedrock* scattering areas, in terms of missed and false alarms. Fig. 4.4 shows the fitting performances of the detection of the three detected borderlines with the reference borders (derived manually) for the portion of radargram shown in Fig. 4.1(a).

By analyzing the quantitative and qualitative results one can observe that in most of the cases the proposed algorithm detects the targets of interest accurately. The few errors are mainly due to the sliding window approach employed, which tends to filter out some returns, mainly in the regions with low backscattering (e.g., the *bedrock* region). This effect, combined with the thresholding operation, leads to a slight increase in the missed alarm rate. However, the low values of overall errors confirm the effectiveness of the proposed technique.

4.4 Conclusion

In this Chapter we have provided a second contribution to the problem of the identification of ice subsurface targets. In particular, we proposed an unsupervised automatic technique for the detection of the ice subsurface targets and the estimation of their properties from radargrams acquired at the Earth continental polar caps. The main novel contributions of the proposed technique are: i) it is defined on the basis of a realistic model of radargrams that considers the effects of the wave propagation through the ice subsurface (i.e., the presence of the EFZ and the discontinuous shape of the bedrock scattering area), and ii)

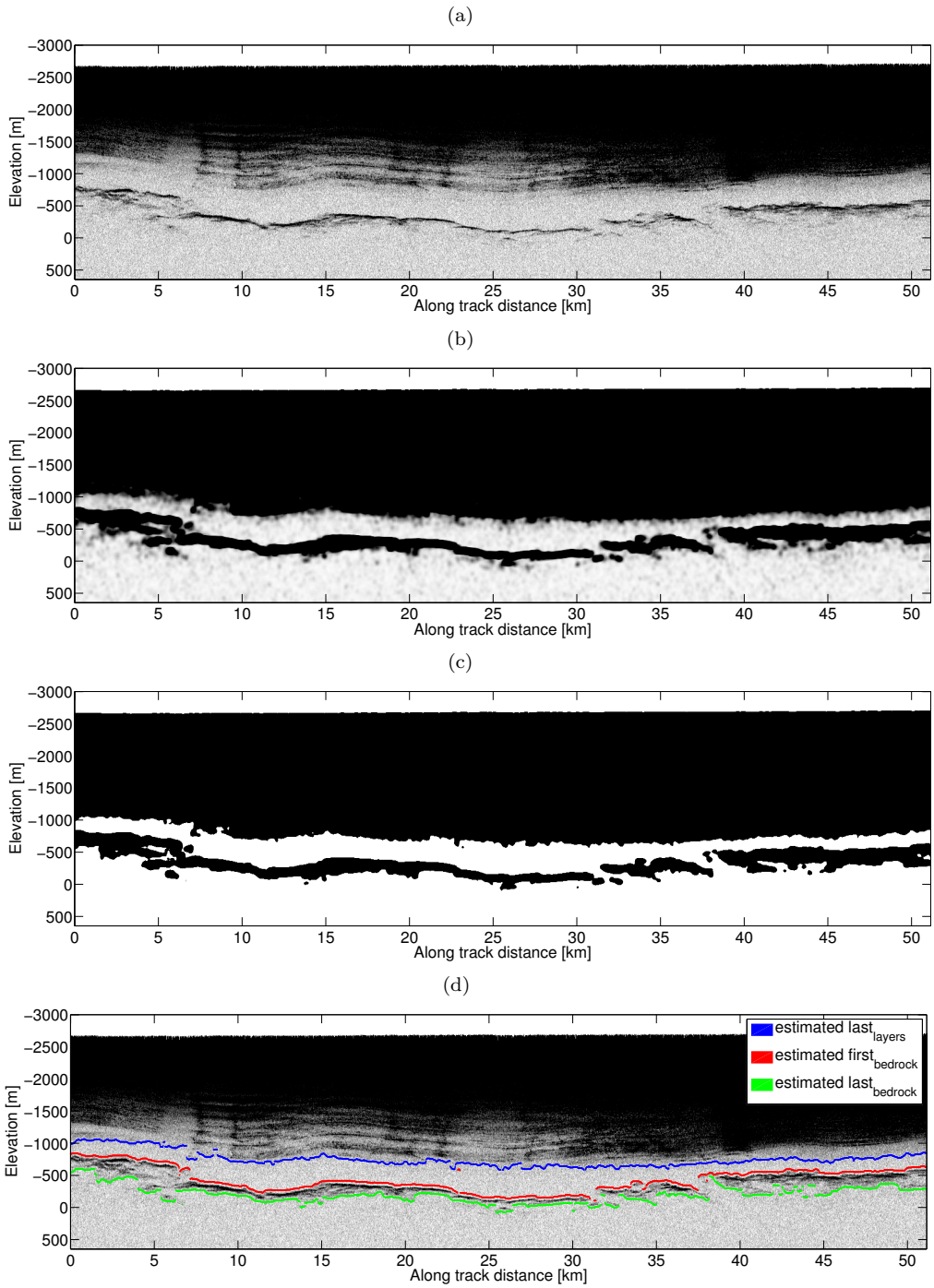

Figure 4.2: (a) Example of aligned radargram (dB data). The portion of radargram considered [410 × 3500] represents a segment on the ground of about 50km, (b) Corresponding $\mathrm{KL}_{R_{ss}}$ statistical map, (c) Corresponding KL_{bin} map, and (d) Results provided by the proposed algorithm.

it involves a segmentation algorithm that enables the detection of both the whole layer area, the ice column (containing also the EFZ) and the bedrock scattering area. The

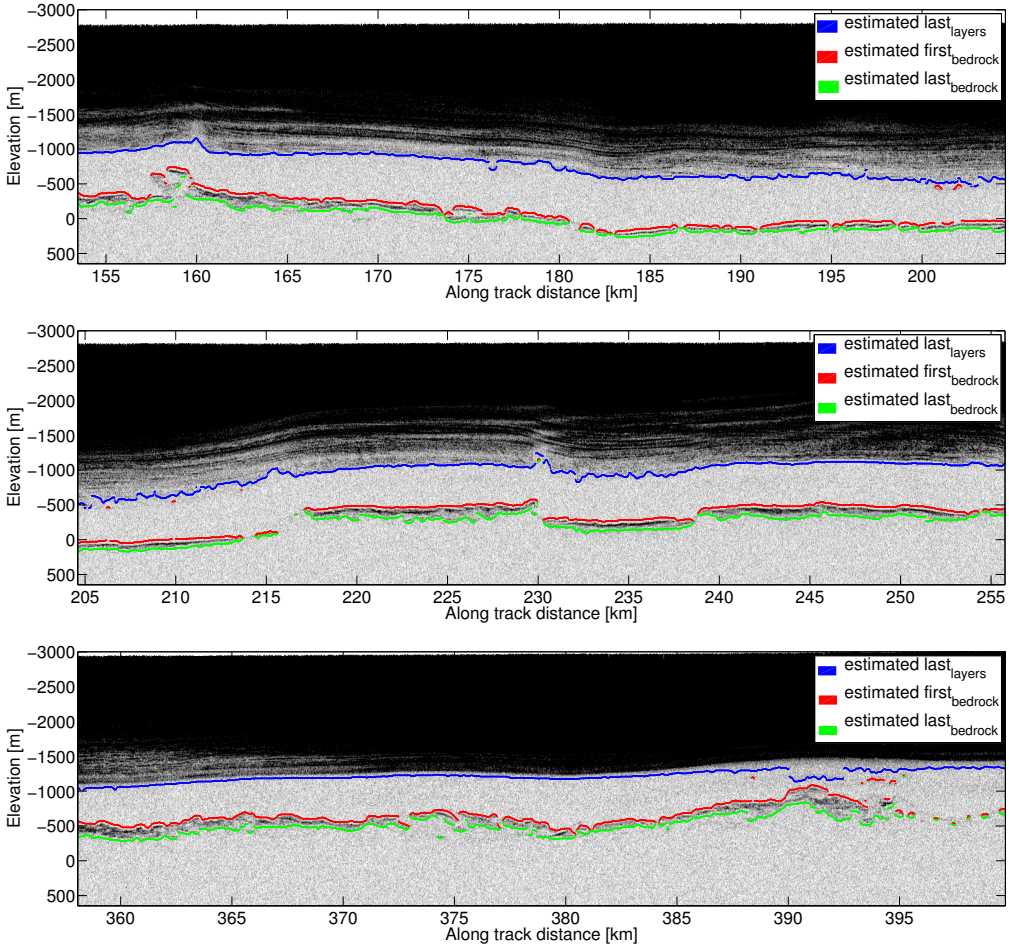

Figure 4.3: Example of results provided by the proposed algorithm on three different portions of the aligned radargram.

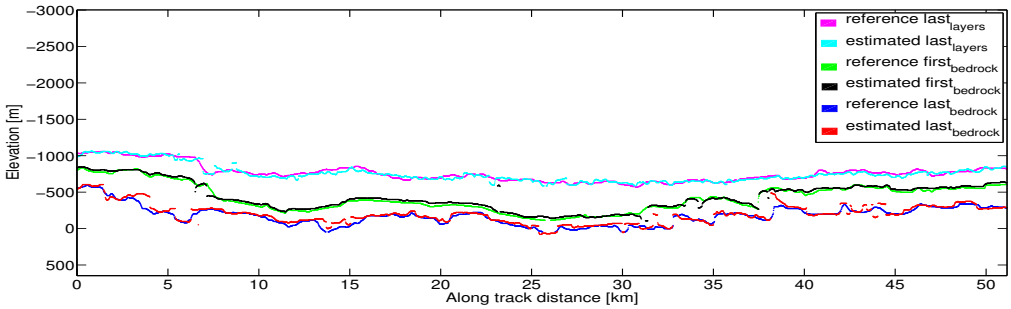

Figure 4.4: Example of fitting performances for the $last_{layers}$, $first_{bedrock}$ and $last_{bedrock}$ borderlines for the portion of radargram shown in Fig. 4.1(a).

accurate results obtained by applying the proposed technique to real data acquired by an airborne RS in Antarctica prove its effectiveness for the large scale analysis of ice

subsurface.

As future development of this work, we aim to include in the proposed technique an algorithm for the mitigation of surface clutter returns highlighted in the $\mathrm{KL}_{R_{ss}}$ map, in order to improve the final detection results.

Chapter 5

Automatic Local 3D Reconstruction of the Ice Sheet by Using Radar Sounder and Altimeter Data

This Chapter[1] *provides a contribution to the problem of 3D ice sheet modeling. In particular, we propose an automatic technique for the local 3D reconstruction of the ice sheet, by using jointly RS and ALT data. The technique exploits the complementarity of the RS and ALT data and relies on the use of the ordinary kriging geostatistical interpolation method and on several statistical measures for validating the interpolation results and the quality of interpolation. Results obtained on a real RS and ALT dataset acquired in Antarctica prove the effectiveness of the proposed technique.*

5.1 Introduction

During the past decades several studies in glaciology highlighted the importance of better understanding the ice sheet dynamics and processes. Remote sensing data acquired at the ice sheets are the main input of such studies. In particular, radar sounder (RS) instruments, which acquire radargrams that show the ice sheet cross-section, and altimeters (ALT), which acquire surface elevation data, represent two of the most important sources of information on the ice sheets. At the ice sheets, RSs are usually operated using airborne platforms equipped with a global positioning system (GPS). During the several dedicated RS airborne campaigns carried out, a huge volume of RS data with heterogeneous quality

[1] Part of this chapter appears in:

[89] Ilisei, A.-M. and Bruzzone, L. ,"Automatic Local 3D Reconstruction of the Ice Sheet by Using Radar Sounder and Altimeter Data," *IEEE Transactions on Geoscience and Remote Sensing*, Submitted for publication in February 2016.

and local coverage has been generated and is now available in archives. On the other hand, ALTs are Earth orbiting laser or radar instruments that have been providing enormous quantities of ice surface elevation data. The availability and the complementarity of the RS and ALT data (see Sec. 5.2.1) and the need for better modeling the ice sheet structure, call for the development of novel automatic techniques for the generation of improved 3D maps of the ice sheet surface, ice/bedrock interface and ice thickness. As pointed out in the review of the related literature, (see Sec. 2.2), the availability of automatic techniques for the reconstruction of the ice subsurface by using multisensor data is still limited.

In this Chapter we contribute to the related literature by proposing an automatic technique for the local 3D reconstruction of the ice sheets, which uses jointly RS and ALT data. The technique aims to address two main challenges: i) the reconstruction should be performed by estimating 3D maps of the ice surface, ice/bedrock and ice thickness at the most reliable scale s^*, derived automatically given the input RS and ALT data properties, and ii) the estimated maps should have the highest overall quality, i.e., the lowest overall uncertainty. Our choice of focusing on the local rather than the global ice sheet 3D reconstruction is driven by the importance that some regions have for specific glaciological analyses. The absence of satellite Earth orbiting RS missions limits the data acquisition with airborne platforms to relatively small regions of particular glaciological importance. Our objective is thus to perform a thorough subsurface reconstruction of such regions, in order to support the glaciological community to improve the use of the available data for a better understanding of the local structure of the ice sheet. To this aim, we employ the ordinary kriging (OK) method [90], which along with the estimated elevation maps, also provides uncertainty interval maps that quantify the overall quality of the estimation.

The proposed technique relies on data processing techniques and statistical measures on the basis of which it aims to identify the most reliable scale s^* for interpolation and the highest overall quality 3D maps of the ice surface elevation and ice/bedrock interface. The method is composed of 4 main blocks, i.e., A) RS data preprocessing, B) identification of the OK parameter set and identification of s^* for the estimation of the ice surface map with the highest overall quality at the most reliable scale, C) identification of the OK parameter set for the estimation of the bedrock elevation map with the highest overall quality at s^*, and D) estimation of the ice thickness map at s^*. In order to identify s^*, several candidate scales are investigated. The highest quality map at a certain scale is the one with the lowest overall uncertainty among different maps generated by interpolating the RS measurements with the OK method run with different parameter sets. The most reliable scale is chosen by minimizing the overall absolute error between the highest quality ice surface elevation map at each scale and consistently rescaled ALT data. The identification

of s^* can be viewed as a validation of the interpolation method by considering the rescaled ALT data as reference. Thus, for the identification of s^*, the complementary properties of the input RS and ALT data are exploited. The joint use of RS and ALT data for the optimization of the interpolation, the automatic identification of s^*, and the analysis and use of the uncertainty maps generated by the OK method are the main novel contributions of this work with respect to other works in the literature that aim to reconstruct the ice subsurface with the OK method (e.g., [48], [42]).

Results obtained by validating the method on a subset of RS data acquired by the MultiChannel Coherent Radar Depth Sounder (MCoRDS) [14] and ALT data acquired by the Geoscience Laser Altimeter System (GLAS)/ICESat [91] over a portion of the Byrd Glacier in Antarctica confirm its effectiveness.

The remaining of this Chapter is organized as follows. Sec. 5.2.1 describes the main properties of the RS and ALT data. Sec. 5.2.2 presents the general description of the OK method. The proposed technique is presented in Sec. 5.3. Sec. 5.4 illustrates results obtained by applying the technique to real RS and ALT data acquired in Antarctica. Finally, Sec. 5.5 draws the conclusion of this work and proposes ideas for future developments.

5.2 Background

5.2.1 Properties of the radar sounder and altimeter data acquired at the ice sheets

Nowadays, there are several archives containing both RS and ALT data acquired at the ice sheets. In this subsection we describe their general properties and derive the relationships that exist among them, mainly in terms of sampling and resolution.

Radar Sounder data. RS data, or radargrams, showing the georeferenced vertical profile of the ice sheet, are acquired during dedicated airborne campaigns at the ice sheets. Orbital RSs have been designed only for the exploration of other planetary bodies, e.g., LRS [4]), SHARA) [5]), RIME (currently under development) [7]. The main advantages of orbiting RSs with respect to airborne RSs are the global coverage, the homogeneous quality of the radargrams and the capability to perform multitemporal acquisitions over wide regions of interest in different seasons or years. Presently, there are no satellite-mounted RSs for Earth observation. RS airborne mission science requirements and technological constraints drive data acquisition strategy plans (e.g., location, flightline spacing) and affect the data quality (e.g., maximum penetration, resolution). Therefore, the RS data acquired during different campaigns present different properties. However, there are properties of the RS data that are common in most acquisitions. For instance, the spacing between two adjacent measurements in the flightline/azimuth direction d_x^{RS} is typically

much smaller than the spacing between two adjacent flightlines d_y^{RS}. This results in a highly irregular sampling pattern in the horizontal direction, with d_x^{RS} (in the order of few m) $\ll d_y^{RS}$ (in the order of few km). The vertical resolution δ_z^{RS} is generally obtained through range compression [92] and depends on both the bandwidth of the system and the type of windowing used to remove the sidelobes generated through compression. Typical values for δ_z^{RS} range between few m and few tens of m. The resolution of the data in the azimuth direction δ_x^{RS} is much finer than the resolution in the cross-track direction δ_y^{RS}. The finer resolution in the azimuth direction is obtained by applying SAR techniques to the raw or range compressed data, whereas the same cannot be done in the cross-track direction [93], thus δ_x^{RS} (which ranges between few m and few tens of m) $\ll \delta_y^{RS}$ (which ranges between few hundreds of m and few km, depending on the platform height and the ice surface roughness).

Altimeter data. ALT measurements over the ice sheets are typically acquired from satellite platforms. With respect to the RSs that take georeferenced measurements of the 2D vertical profile of the ice, the ALTs take georeferenced measurements of the ice surface elevation only, on wide areas. ALT measurements are subsequently processed to provide 3D maps of the ice surface, called DEMs. The resolution δ^{ALT} and spacing d^{ALT} in the horizontal direction of the DEMs are uniform and typically have values $\delta^{ALT} \approx d^{ALT} \approx$ few hundreds of m. Thus, with respect to the RS data, they are typically in the relationship $d_x^{RS} \ll \delta^{ALT} \approx d^{ALT} \ll d_y^{RS}$. A qualitative representation of the described RS and ALT data properties in terms of resolution and spacing in the horizontal directions is given in Fig. 5.1. In the vertical direction, the resolution δ_z^{ALT} of the ALT data is generally in the order of few cm to few m, thus much finer than that of the RS data, i.e., $\delta_z^{ALT} \ll \delta_z^{RS}$.

The analysis of the general properties of the RS and ALT data points out that they have complementary attributes that can be exploited together in order to aid for a better usage and extraction of information from the available measurements.

5.2.2 Ordinary Kriging: general concept and problem formulation in the proposed method

The proposed technique relies on the use of the OK method. In this subsection we provide a general description of the parts of the OK method which are relevant for the proposed technique.

OK is a geostatistical interpolation method that estimates the value of a random variable at an unknown/query position x_0, i.e., $\hat{e}(x_0)$, based on N_0 known/observed values at positions $x_n, n = [1..N_0]$, i.e., samples $e(x_n)$ in the domain of interest. OK relies on what is called spatial variability analysis (SVA), which is a process that aims to quantify

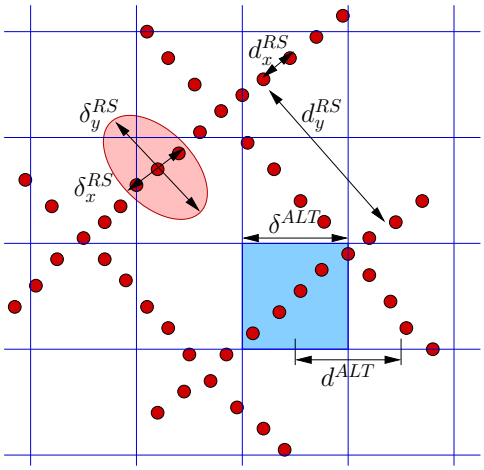

Figure 5.1: Qualitative representation of RS and ALT data spacing and resolution in the horizontal direction. Note the general relationship $d_x^{RS} \ll d^{ALT} \approx \delta^{ALT} \leq d_y^{RS}$.

the spatial autocorrelation of the samples through the generation and model fitting of the empirical semivariogram $\hat{\gamma}(\mathbf{h})$. In this study we assume an isotropic model of spatial variability, thus $\hat{\gamma}(\mathbf{h})$ is a graph generated by computing the squared difference between all pairs of samples separated by a distance (lag) h_k. $\mathbf{h}$ is the vector of point pair distances h_k, with $k = [1..\bar{k}]$, where $\bar{k}$ is the maximum number of bins of the semivariogram. Several candidate theoretical models γ^{Can} can be used to fit the empirical semivariogram. Appendix 5.6 reports the analytical formulation of the theoretical models used in our analysis, i.e., the Spherical γ^{Sph}, Exponential γ^{Exp}, Gaussian γ^{Gau} and Linear γ^{Lin} models. We chose these models since they are likely to fit elevation data. In particular, the Spherical model and the Exponential model have a steep behavior near the origin, and therefore are suitable for representing surfaces with high elevation variability at short range, i.e., with weak autocorrelation. Among the two models, the Exponential model, with its steeper behaviour near the origin, is appropriate for representing rougher surfaces. The Gaussian model has a parabolic shape near the origin, therefore it is suitable for representing smoothly varying surfaces. The Linear model indicates non-stationarity in the data. The presence of non-stationarity in the data invalidates the intrinsic hypothesis required in geostatistics. A common approach used to solve the problem of non-stationarity is to fit a trend surface to the data and to regenerate the semivariogram by using the residuals [94], [95]. The vector of parameters θ of each theoretical model can be estimated on the basis of the weighted least square criterion [96], expressed as follows:

$$\tilde{\theta} = \min_{\theta} \sum_{k=1}^{\bar{k}} w_k [\hat{\gamma}(h_k) - \gamma^{Can}(h_k, \theta)]^2, \tag{5.1}$$

where w_k is the weight associated to bin k. Then, the fitting performances of these models can be quantified in terms of the R^2 indicator; the best fitting model with the associated vector of parameters $\gamma^*(\mathbf{h};\tilde{\theta})$ is the one that maximizes R^2, according to:

$$\gamma^*(\mathbf{h};\tilde{\theta}) = \max_{\gamma^{Can}}\{1 - \frac{\sum_{k=1}^{\bar{k}}[\hat{\gamma}(h_k) - \gamma^{Can}(h_k;\tilde{\theta})]^2}{\sum_{k=1}^{\bar{k}}[\hat{\gamma}(h_k)]^2}\}. \tag{5.2}$$

$\gamma^*(\mathbf{h};\tilde{\theta})$ is the output of the SVA and is used to interpolate the observed samples in order to estimate $\hat{e}(x_0)$ (see (5.3)). Moreover, since OK is a (geo)statistical method, it also provides an uncertainty value $u(x_0)$ (see (5.4)) associated to $\hat{e}(x_0)$.

$$\hat{e}(x_0) = \frac{1'_{N_0}V_0^{-1}e_{N_0}}{1'_{N_0}V_0^{-1}1_{N_0}} + c'_0V_0^{-1}e_{N_0} - c'_0V_0^{-1}1_{N_0}\frac{1'_{N_0}V_0^{-1}e_{N_0}}{1'_{N_0}V_0^{-1}1_{N_0}}, \tag{5.3}$$

$$u(x_0) = 1.96\sqrt{\sigma^2 - c'_oV_0^{-1}c_o + \frac{(1 - 1'_{N_0}V_0^{-1}c_0)^2}{1'_{N_0}V_0^{-1}1_{N_0}}}. \tag{5.4}$$

In (5.3) and (5.4) the superscript '-1' denotes the inverse of a matrix, e_{N_0} is the vector of N_0 observed values surrounding x_0, 1_{N_0} is a column vector of N_0 ones, and the apex "$\prime$" denotes the vector or matrix transpose operation. c_0 and V_0 are the elements of the full covariance matrix C_0 in x_0, defined as:

$$C_0 = \begin{pmatrix} \sigma^2 & c'_o \\ c_o & V_0 \end{pmatrix}. \tag{5.5}$$

The column vector c_0, the submatrix V_0 and σ^2 can be estimated by employing the covariogram $\mathcal{C}(\mathbf{h})$, as follows:

$$\begin{cases} \hat{c}_0 = (\hat{\sigma}_{0i} : i = [1..N_0])', \\ \quad \text{with } \hat{\sigma}_{0i} = cov[e(x_0), e(x_i)] = \mathcal{C}(||x_0 - x_i||), \\ \hat{V}_0 = (\hat{\sigma}_{ij}, i, j = [1..N_0]) = \mathcal{C}(||x_i - x_j||) = \mathcal{C}(h_{ij}), \\ \hat{\sigma}^2 = \hat{\sigma}^2_{00} = var[e(x_0), e(x_0)] = \mathcal{C}(||x_0 - x_0||) = \mathcal{C}(0), \end{cases} \tag{5.6}$$

where $var(a, a)$ denotes the variance of a random variable a, $cov(a, b)$ denotes the covariance of two random variables a and b, and $||x_i - x_j|| = h_{ij}$ denotes the euclidean distance between two locations x_i and x_j. Note that under the assumption of intrinsic stationarity [95], which is required in order to perform the geostatistical interpolation, $\mathcal{C}(\mathbf{h})$ can be best estimated by employing the empirical semivariogram best fitting model with the estimated parameters $\gamma^*(\mathbf{h};\tilde{\theta})$.

On the basis of the couple of values $\hat{e}(x_0)$ and $u(x_0)$, one can infer with 95% confidence that the true value $e(x_0)$ lies in the interval $[\hat{e}(x_0) \pm u(x_0)]$. Therefore, the lower the

uncertainty value, the more the estimated value is expected to approach the true value, i.e., the better the estimation.

SVA can be performed by using different parameter sets $p_i, i = [1..P]$ within the OK method. Tab. 5.1 reports the parameter sets considered in our analysis. In particular, note that we consider two possible ways to perform the aggregation of point pairs in each bin of the empirical semivariogram, i.e., constant binsize (bs) and constant binwidth (bw). In both cases, h_k is computed as the mean value of all the distances inside bin k. With the bs option, we create bins (of point pair distances) with variable width and with constant number of point pairs within each bin. In the bw option, the number of point pairs within each bin can vary, whereas the width of all $\bar{k}$ bins is the same. This difference is one of the main drivers of the estimation, therefore we study it by considering the *binning* = {bw,bs} as the first subset of parameters within the OK parameter set (see Tab. 5.1). Furthermore, we consider the choice of the *weighting* function (see (5.1)) as the second subset of parameters of the OK method. Several weighting functions have been proposed in the literature, among which we investigate the following:

- $\mathbf{W}1 = \left\{w_k = 1, \forall k = [1..\bar{k}]\right\}$. This represents the case in which the weights are all constant, as for the ordinary least squares criterion.
- $\mathbf{W}2 = \left\{w_k = |N_k|, \forall k = [1..\bar{k}]\right\}$. In this case higher weight is given to the bins k containing a higher number of samples.
- $\mathbf{W}3 = \left\{w_k = 1/[\gamma(h_k;\theta)]^2, \forall k = [1..\bar{k}]\right\}$. This is a particular case of inverse distance weighting, in which the experimental variogram points close to the origin receive higher weight than experimental variogram points at larger distances.
- $\mathbf{W}4 = \left\{w_k = |N_k|/[\gamma(h_k;\theta)]^2, \forall k = [1..\bar{k}]\right\}$. In this case the weights are set to the inverse of the uncertainty of the semivariogram estimate (or estimation variance). This is a popular weighting function [96], proven to work in many practical situations as it represents a good compromise of statistical efficiency and computability.
- $\mathbf{W}5 = \left\{w_k = |N_k|/h_k^2, \forall k = [1..\bar{k}]\right\}$. This weighting function gives more weight to estimates calculated with more point pairs and at short distances [97].

Therefore, *weighting* = $\{\mathbf{W}1, \mathbf{W}2, \mathbf{W}3, \mathbf{W}4, \mathbf{W}5\}$ (see Tab. 5.1). Considering all the combinations $\{binning, weighting\}$, one can deduce that there are 10 possible parameter sets p_i for the semivariogram best model fitting. In fact, note that the number of parameter sets reduces to $P = 8$ (see Tab. 5.1), since by definition, the parameter set $\{\text{bs}, \mathbf{W}1\} \equiv \{\text{bs}, \mathbf{W}2\}$, and $\{\text{bs}, \mathbf{W}3\} \equiv \{\text{bs}, \mathbf{W}4\}$. Given the parameter sets, it is worth to highlight the dependence of the fit on p_i; there are P semivariogram best fitting models $\gamma^*_{p_i}(\mathbf{h};\tilde{\theta}), i = [1..P]$ characterized by different values of the vector of parameters $\tilde{\theta}$. Consequently, for a

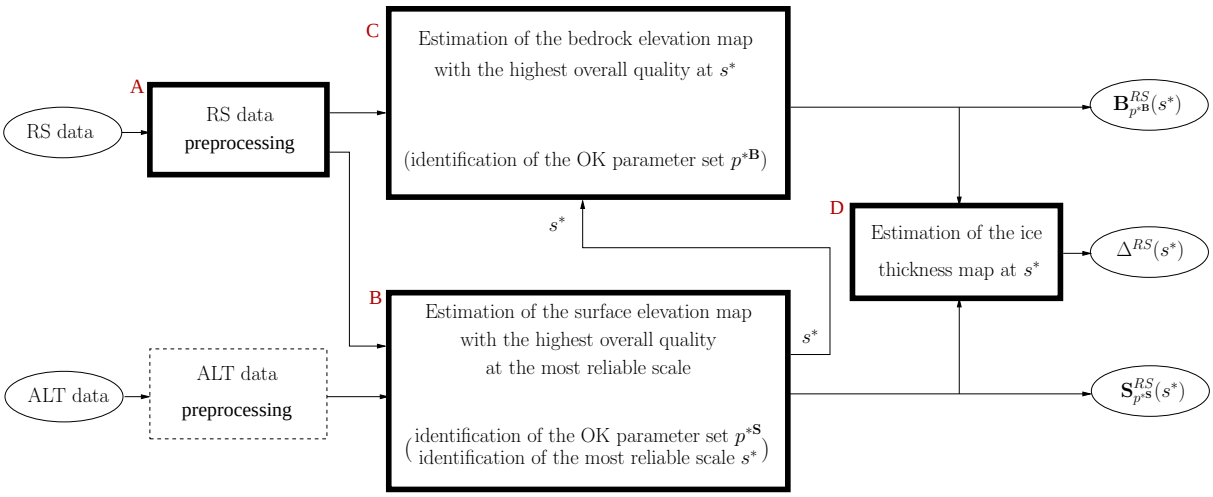

Figure 5.2: Architecture of the proposed technique.

query point x_0, not a single estimate, but a set of P estimates can be generated along with the corresponding set of uncertainty values, $\hat{e}^i(x_0)$ and $u^i(x_0), i = [1..P]$, respectively. By extending this reasoning to all the query points in the domain of interest, the OK method provides P estimated maps and P corresponding uncertainty maps.

Table 5.1: Parameter sets considered in the OK method.

binning	weighting	parameter set
bw	$\mathbf{W}1 = \{w_k = 1\}$	p_1={bw,$\mathbf{W}1$}
bs	$\mathbf{W}2 = \{w_k = \lvert N_k\rvert\}$	p_2={bw,$\mathbf{W}2$}
	$\mathbf{W}3 = \left\{w_k = 1/[\gamma(h_k;\theta)]^2\right\}$	p_3={bw,$\mathbf{W}3$}
	$\mathbf{W}4 = \left\{w_k = \lvert N_k\rvert/[\gamma(h_k;\theta)]^2\right\}$	p_4={bw,$\mathbf{W}4$}
	$\mathbf{W}5 = \left\{w_k = \lvert N_k\rvert/h_k^2\right\}$	p_5={bw,$\mathbf{W}5$}
		p_6={bs,$\mathbf{W}1$}
		p_7={bs,$\mathbf{W}3$}
		p_8={bs,$\mathbf{W}5$}

5.3 Proposed method

Fig. 5.2 shows the architecture of the proposed technique, which is made up of 4 main blocks (the dashed block, which represents an intermediate step to the generation of the ice surface map from the altimeter data is not developed in this paper). Assuming the availability of only RS an ALT data, partial (i.e., not fully 3D) information of the ice

subsurface can be extracted only in the flightline direction from the radargrams. In order to estimate the 3D structure of the ice subsurface, an efficient interpolation strategy of these measurements should be adopted. The interpolation should be carried out at a scale s^* that is validated by using the ALT data of the ice surface, which can be considered as reference. Furthermore, the estimated maps should have the highest overall quality. A detailed description of the processing steps involved in all the blocks of the method is given in the following subsections.

5.3.1 Radar sounder data preprocessing

The aim of this step is the extraction from the radargrams of the surface and bedrock elevation along the flightline direction at the original scale s_0^{RS} of the RS data. s_0^{RS} is given by the spacing between two adjacent measurements (or columns/traces of the radargram) in the along-track direction d_x^{RS}, i.e., $s_0^{RS} = d_x^{RS}$. Each trace of the radargram contains the RS measurements of power reflected by the surface and subsurface features at each platform coordinate (in the flightline/azimuth direction) as a function of radar wave travel time. We first detect the surface and bedrock reflection positions. This can be done manually or according to automatic techniques (see [61]). Then, we estimate the elevation of the ice surface and bedrock for all traces of the radargram, by using the elevation of the platform (given by the GPS along with the radargram) and a standard time-distance conversion equation that considers propagation in two media, air and ice. The output of this step consists of two sets of measurements forming an irregular pattern, i.e., the surface elevation and the bedrock elevation at the initial along-track scale s_0^{RS} of the RS data, i.e., $S^{RS}(s_0^{RS})$ and $B^{RS}(s_0^{RS})$, respectively. The set $S^{RS}(s_0^{RS})$ is used in the second block of the technique (see Sec. 5.3.2 and Fig. 5.3), while the set $B^{RS}(s_0^{RS})$ is used in the third block (see Sec. 5.3.3 and Fig. 5.4).

It is worth mentioning here that there are a few factors that influence the accuracy of the above estimations. The clutter is one critical factor. It is due to off-nadir surface reflections arriving at the RS receiver at the same time as the nadir reflections from the subsurface. For this reason, the bedrock reflection can be masked by clutter and therefore incorrectly detected. In order to limit the negative effect of clutter on the estimation of the ice thickness, we use radargrams processed with the minimum variance distortionless response (MVDR) algorithm for clutter reduction [1]. Other sources of errors in the estimation of the ice elevation and thickness are due to the GPS accuracy, the sampling frequency of the RS in the vertical direction, the accuracy of the automatic detection method employed (i.e., [61]) and the assumed dielectric permittivity of the ice. In fact, we here consider a constant dielectric permittivity of pure ice $\varepsilon^{ice} = 3.15$ along the whole ice column, neglecting the presence of firn and ice impurities. However, this will result in

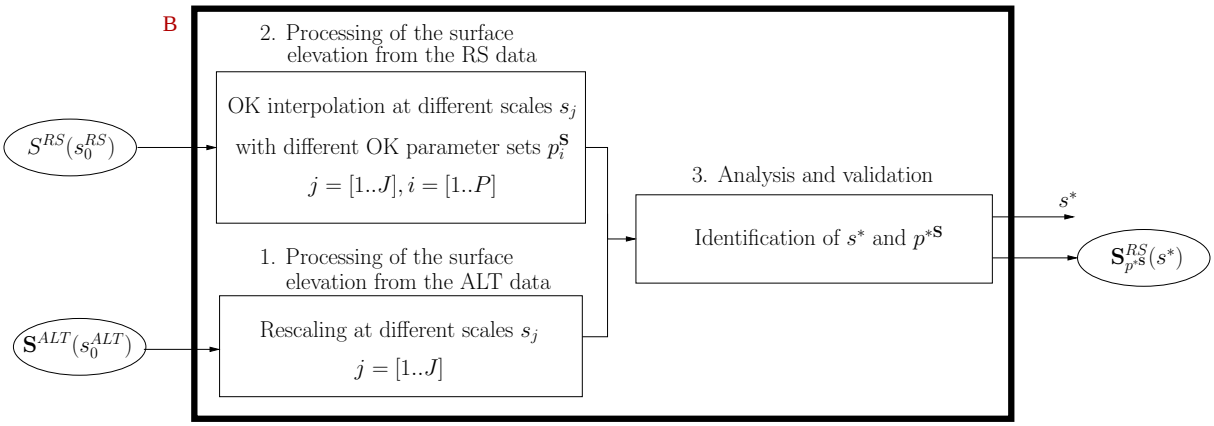

Figure 5.3: Detailed architecture of the second block of the proposed technique.

about 10m error in the ice thickness estimate [43].

5.3.2 Estimation of the surface elevation map with the highest overall quality at the most reliable scale

This block identifies the scale s^* at which the irregular pattern of surface elevation samples $S^{RS}(s_0^{RS})$ can be interpolated in order to obtain a reliable estimate of the ice surface elevation. At the same time, we require that estimates have the best overall quality with respect to different parameter sets of the adopted OK method. To address these challenges, we investigate a) several candidate scales $s_j, j = [1..J]$, and b) for each candidate scale s_j several parameter sets $p_i^{\mathbf{S}}, i = [1..P]$. As depicted in Fig. 5.3, this is accomplished in 3 main steps: 1) Processing of the surface elevation from the ALT data, 2) Processing of the surface elevation from the RS data, and 3) Analysis and validation.

Processing of the surface elevation from the ALT data

The ALT data is available only for the ice surface elevation and is provided at the original scale s_0^{ALT}, i.e., $\mathbf{S}^{ALT}(s_0^{ALT})$. In this step we rescale the map $\mathbf{S}^{ALT}(s_0^{ALT})$ in order to generate reference maps for validating the interpolation process of the S^{RS} samples at different scales $s_j, j = [1..J]$. To this aim we use the bicubic interpolation method [98] at each scale $s_j, j = [1..J]$. This operation provides a set of J maps $\mathbf{S}^{ALT}(s_j)$, with decreasing resolution as s_j increases.

Processing of the surface elevation from the RS data

The final goal of this step is the estimation of the set of surface elevation maps obtained by running the OK method with P different parameter sets at a generic scale s_j. In order

to obtain estimates of the surface elevation maps from the RS data, we use the available surface elevation measurements $S^{RS}(s_0^{RS})$ (see Sec. 5.3.1). Since we are interested in the results at scale s_j, we first rescale $S^{RS}(s_0^{RS})$ to obtain $S^{RS}(s_j)$. We accomplish this by simply averaging adjacent RS measurements in the along-track direction on a distance s_j and by collecting one measurement every s_j meters to define the set of rescaled measurements $S^{RS}(s_j)$. Note that by increasing s_j the pattern of these measurements becomes more regular, with the along-track spacing of the rescaled measurements $d_x^{RS}(s_j) = s_j$ approaching d_y^{RS}. Then, we interpolate $S^{RS}(s_j)$ with the OK method (see 5.2.2) by considering for the interpolation at each query point its $N_0 = 10$ nearest observed neighbors from $S^{RS}(s_j)$. We estimate the ice surface elevation and uncertainty maps at the same query points used to estimate $\mathbf{S}^{ALT}(s_j)$. As there are P possible parameter sets to be used in the OK method, for each scale s_j we generate P ice surface map estimates $\mathbf{S}^{RS}_{p_i^{\mathbf{S}}}(s_j), i = [1..P]$ and P corresponding uncertainty maps $\mathbf{U}^{\mathbf{S}}_{p_i^{\mathbf{S}}}(s_j), i = [1..P]$.

Analysis and validation

The aim of this step is two-fold, i.e., i) the identification at a generic scale s_j of the best parameter set $p^{*\mathbf{S}}$ and the associated $\mathbf{S}^{RS}_{p^{*\mathbf{S}}}(s_j)$ and $\mathbf{U}^{\mathbf{S}}_{p^{*\mathbf{S}}}(s_j)$, and ii) the identification of the best scale s^* and the corresponding $\mathbf{S}^{RS}_{p^{*\mathbf{S}}}(s^*)$ and $\mathbf{U}^{\mathbf{S}}_{p^{*\mathbf{S}}}(s^*)$. First, we identify the parameter set $p^{*\mathbf{S}}(s_j)$ at a generic scale s_j that provides the ice elevation map most similar to the reference $\mathbf{S}^{ALT}(s_j)$ and has the highest overall quality. At a certain scale s_j this is obtained by analyzing the statistical properties of the absolute error maps $\mathbf{D}_{p_i^{\mathbf{S}}}(s_j)$ (see (5.7)) and of the uncertainty maps $\mathbf{U}^{\mathbf{S}}_{p_i^{\mathbf{S}}}(s_j)$.

$$\mathbf{D}_{p_i^{\mathbf{S}}}(s_j) = |\mathbf{S}^{RS}_{p_i^{\mathbf{S}}}(s_j) - \mathbf{S}^{ALT}(s_j)|, \forall i = [1..P], \tag{5.7}$$

where $|a|$ denotes the absolute value of a. The key idea is to choose the parameter set that minimizes the mean value of $\mathbf{D}_{p_i^{\mathbf{S}}}(s_j), i = [1..P]$. In the case in which there are different parameter sets that provide similar values of $\mathbf{D}_{p_i^{\mathbf{S}}}(s_j)$ (and therefore no parameter set can be considered better than the others for interpolating the RS measurements), we choose the best parameter set by minimizing the mean value of $\mathbf{U}^{\mathbf{S}}_{p_i^{\mathbf{S}}}(s_j), i = [1..P]$. By doing so we aim to ensure that the OK solution has the highest overall quality (i.e., the lowest overall uncertainty). This operation provides $p^{*\mathbf{S}}(s_j)$ and implicitly $\mathbf{S}^{RS}_{p^{*\mathbf{S}}}(s_j)$ and $\mathbf{U}^{\mathbf{S}}_{p^{*\mathbf{S}}}(s_j)$.

The identification of the best parameter set is performed for all the scales $s_j, j = [1..J]$. Thus, we obtain a set of J elevation maps $\mathbf{S}^{RS}_{p^{*\mathbf{S}}}(s_j), j = [1..J]$, and a set of J corresponding uncertainty maps $\mathbf{U}^{\mathbf{S}}_{p^{*\mathbf{S}}}(s_j), j = [1..J]$. At this point we identify the scale s^* which provides, from a statistical point of view, the ice elevation map most similar to the reference rescaled ALT data. s^* is the scale that minimizes the mean value of the

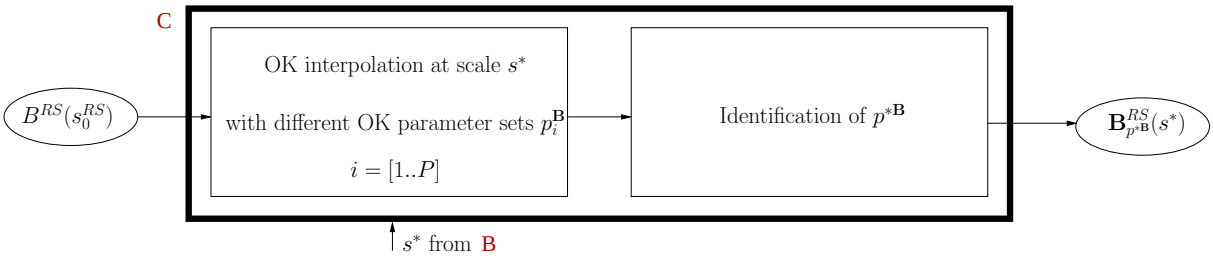

Figure 5.4: Detailed architecture of the third block of the proposed technique.

absolute error maps $\mathbf{D}_{p^{*\mathbf{S}}}(s_j)$ (see (5.8)).

$$\mathbf{D}_{p^{*\mathbf{S}}}(s_j) = |\mathbf{S}^{RS}_{p^{*\mathbf{S}}}(s_j) - \mathbf{S}^{ALT}(s_j)|, \forall j = [1..J]. \tag{5.8}$$

This operation provides s^* and implicitly $\mathbf{S}^{RS}_{p^{*\mathbf{S}}}(s^*)$ and $\mathbf{U}^{\mathbf{S}}_{p^{*\mathbf{S}}}(s^*)$. It is worth noting that, although we identify the best parameter set and the most reliable scale based on the minimization of the first order statistics (mean), more complex criteria could also be used, e.g., based on second order statistics (variance), R^2 indicator, root mean square error.

5.3.3 Estimation of the bedrock map with the highest overall quality at the most reliable scale

The processing steps involved in the estimation of the bedrock map are similar to those performed for the estimation of the ice surface elevation map. The main difference is the fact that, in the absence of ALT reference data of the bedrock, we choose to investigate the interpolation results only at scale s^* (see Fig. 5.4). Thus, we first rescale the RS bedrock measurements at s^*, as done with the RS ice surface elevation measurements (see Sec. 5.3.2), in order to obtain $B^{RS}(s^*)$. Then, for each query point, we interpolate with the OK method its $N_0 = 10$ nearest neighbors, as done for the surface samples. Since the OK method is run with P parameter sets (see Sec. 5.2.2), we obtain a set of P estimated bedrock maps $\mathbf{B}^{RS}_{p_i^{\mathbf{B}}}(s^*), i = [1..P]$, and a set of P corresponding uncertainty maps $\mathbf{U}^{\mathbf{B}}_{p_i^{\mathbf{B}}}(s^*), i = [1..P]$. In the absence of reference data for constructing the bedrock error maps, we select the best parameter set $p^{*\mathbf{B}}$ as the one that minimizes the mean value of $\mathbf{U}^{\mathbf{B}}_{p_i^{\mathbf{B}}}(s^*)$, i.e., which yields the highest overall quality. This operation provides $p^{*\mathbf{B}}$ and implicitly $\mathbf{B}^{RS}_{p^{*\mathbf{B}}}(s^*)$ and $\mathbf{U}^{\mathbf{B}}_{p^{*\mathbf{B}}}(s^*)$.

5.3.4 Estimation of the ice thickness map at the most reliable scale

Once the most reliable scale s^*, the surface elevation map and the bedrock elevation map have been derived as described in Sec. 5.3.2 and in Sec. 5.3.3, the ice thickness map

$\Delta^{RS}(s^*)$ can be obtained as:

$$\Delta^{RS}(s^*) = \mathbf{S}^{RS}_{p^{*\mathbf{S}}}(s^*) - \mathbf{B}^{RS}_{p^{*\mathbf{B}}}(s^*). \tag{5.9}$$

It is worth highlighting that the thickness map could have been obtained by directly interpolating the thickness measurements extracted from the RS data rescaled at s^*, i.e., by interpolating with the OK method the values $S^{RS}(s^*) - B^{RS}(s^*)$, as it has been done for the bedrock elevation measurements, (see Sec. 5.3.3). However, that would have likely introduced more ambiguities in the estimation, which are due to both the surface and bedrock elevation variability. For this reason, we chose to interpolate the bedrock measurements, and to subtract the result from the interpolated surface, to get the ice thickness map. Furthermore, since for computing the thickness map we are subtracting 2 maps, it is important that they are consistent and thus at the same scale. This is the main reason for which we chose to estimate the bedrock map at scale s^*, which has been validated for the interpolation of the ice surface samples.

5.4 Experimental results

The proposed technique has been validated on a subset of RS data acquired by the Multi-Channel Coherent Radar Depth Sounder (MCoRDS) [14] and ALT data acquired by the Geoscience Laser Altimeter System (GLAS)/ICESat [91] over a portion of about [32km $\times$ 32km] of the Byrd Glacier in Antarctica. Fig. 5.5(a) shows the investigated area and the positions of the RS flightlines. Tab. 5.2 reports the specific properties of the analyzed data. According to these properties, the values of the initial parameters of the technique are: $s_0^{RS} = d_x^{RS} = 15$m, $s_0^{ALT} = d^{ALT} = 500$m. Fig. 5.5(b)-(c) show the scatterplots of the ice surface elevation S^{RS} and bedrock elevation B^{RS}, computed at s_0^{RS} as described in Sec. 5.3.1.

Table 5.2: Properties of the RS and ALT data used in the experiments.

Property	RS data (MCoRDS)	ALT data (GLAS DEM)
Horizontal spacing	$d_x^{RS} = 15$m, $d_y^{RS} \approx 1.8 - 12$km	$d_x^{ALT} = d_y^{ALT} = d^{ALT} = 500$m
Horizontal resolution	$\delta_x^{RS} = 25$m with SAR processing, $\delta_y^{RS} \in [35 - 250]$m depending on surface roughness (at a platform height ≈ 500m)	$\delta_x^{ALT} = \delta_y^{ALT} = \delta^{ALT} = 500$m
Vertical resolution	$\delta_z^{RS} = 4.3$m in ice, $\delta_z^{RS} = 7.4$m in air with range compression and windowing factor $k_t = 1.53$	$\delta_z^{ALT} = 15$cm

The input data properties drive the choice of the range of scales for interpolation. The minimum scale for interpolation is constrained by the scale of the input ALT data, i.e.,

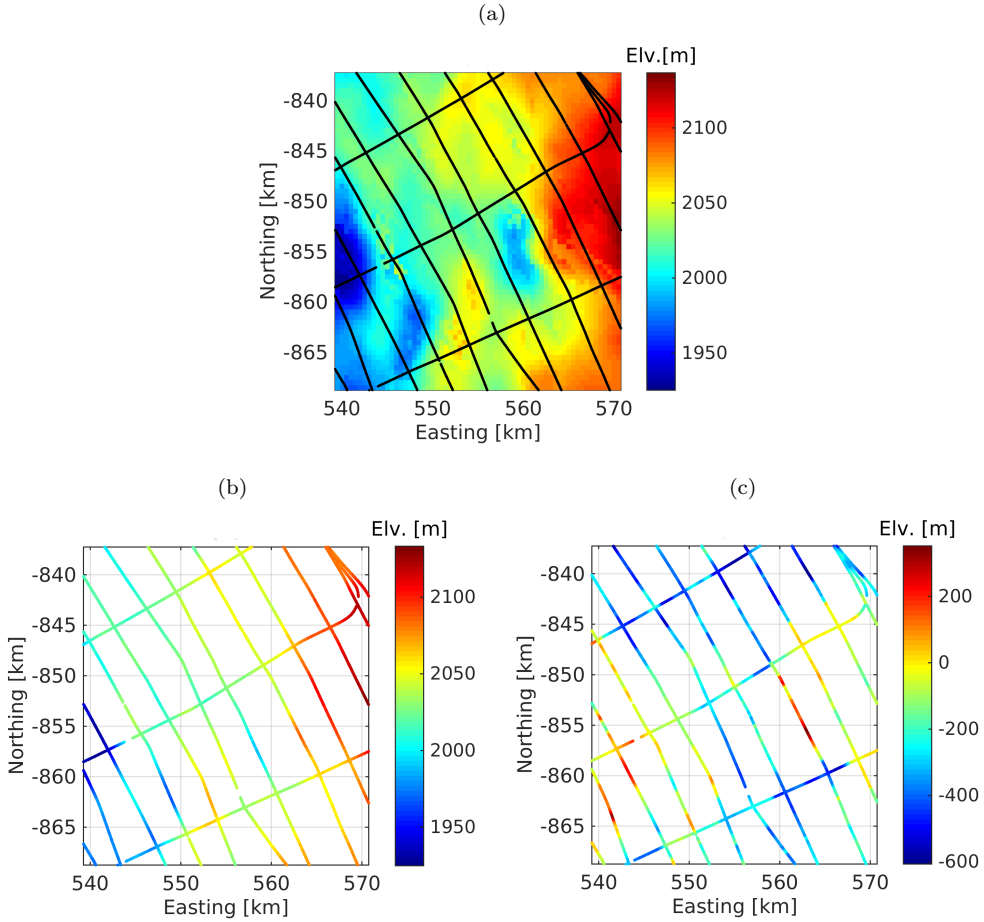

Figure 5.5: Input ALT and RS data. (a) ALT DEM of the ice surface; the position of the RS flightlines are highlighted in black. (b) Scatterplot of the ice surface elevation from the RS data at the original scale $s_0^{RS} = 15$m. (c) Scatterplot of the bedrock elevation from the RS data at the original scale $s_0^{RS} = 15$m.

$s_1 = s_0^{ALT} = 500$m. In fact, since the highest horizontal resolution of the ALT data (which is considered as reference in our technique) is 500m, it is worthless to interpolate the RS measurements at smaller scales; a rescaling of the ALT data at scales smaller than s_0^{ALT}, i.e., upsampling, would only introduce artifacts, with no gain in resolution. On the other hand, the maximum scale for interpolation is imposed by two conditions: i) the number of rescaled RS samples at large scales becomes insufficient for performing a reliable geostatistical analysis (i.e., the fitting performance of the empirical semivariograms suddenly drops for scales ≥ 2000m), and ii) for large scales the resulting maps become too smooth and with insufficient degree of detail. For these reasons, we set the maximum scale for interpolation to be approximately equal to the minimum spacing of the RS data in the across-track direction, i.e., $s_J \approx \min\left\{d_y^{RS}\right\}$. In the above-mentioned range we consider $J = 6$ scales, i.e., $s_j = [500, 750, 1000, 1250, 1500, 1750]$m.

In order to analyze the impact of the different OK parameter sets (see Tab. 5.1), of the different theoretical models (see Appendix B 5.6) used to fit the empirical semivariograms and of the different scales s_j, in the following we provide a qualitative and quantitative assessment of a specific case. We analyze the RS ice surface elevation samples rescaled at $s_1 = 500$m, by considering the first parameter set, i.e., $p_1 = \{\text{bw}, \mathbf{W1}\}$. Fig. 5.6(a)-(d) show the fitting performances of all the 4 investigated theoretical models on the set of rescaled samples $S^{RS}(500)$ (see Sec. 5.3.2). As one can see, the best fitting model in this case is the linear model, with $R^2 = 0.968$ and $\theta = (0.08, 0\text{m}^2)$. Thus, the semivariogram is regenerated as explained in Sec. 5.2.2; we fit a surface to $S^{RS}(500)$ by using a local linear regression procedure [99] and perform the fitting on the semivariogram of the residuals. The residuals and the best fit are illustrated in Fig. 5.6(e) and Fig. 5.6(f), respectively. Quantitatively, the best fitting model in this case is the Gaussian model with $R^2 = 0.806$ and $\theta = (4.14\text{km}, 210.97\text{m}^2, 0\text{m}^2)$.

We apply this algorithm to derive the best fitting model of the semivariograms of ice surface samples generated with all the parameter sets and rescaled at all the $J = 6$ scales $s_j = [500, 750, 1000, 1250, 1500, 1750]$m. The obtained best fitting model with the estimated vector of parameters, for all the investigated cases, are reported in Tab. 5.3. On the basis of these results, ice surface elevation maps and uncertainty maps are estimated for all the parameter sets, for all the scales. The statistics of the absolute error maps $\mathbf{D}_{p_i^{\mathbf{S}}}(s_j)$ and uncertainty maps $\mathbf{U}^{\mathbf{S}}_{p_i^{\mathbf{S}}}(s_j)$, for $i = [1..P], j = [1..J]$ are shown qualitatively in Fig. 5.7(a)-(f) and Fig. 5.8(a)-(f), respectively. As it can be seen from Fig. 5.7(a)-(f), for a certain scale the variability of the mean values of the absolute error maps versus the parameter set is very low. This means that the OK solution for the estimated value tends to keep constant the local mean independently on the parameter set. Therefore, the best parameter set $p^{*\mathbf{S}}$ at each scale s_j, and its corresponding OK solution (i.e., estimated elevation $\mathbf{S}^{RS}_{p^{*\mathbf{S}}}(s_j)$ and uncertainty maps $\mathbf{U}^{\mathbf{S}}_{p^{*\mathbf{S}}}(s_j)$), is derived as the one that minimizes the mean value of all the uncertainty maps generated at scale s_j (see Sec. 5.3.2). The best fitting model and its associated vector of estimated parameters, which are related to the identified best parameter set at each scale, are highlighted in bold in Tab. 5.3. The statistics of $\mathbf{D}_{p^{*\mathbf{S}}}(s_j)$ and $\mathbf{U}^{\mathbf{S}}_{p^{*\mathbf{S}}}(s_j), j = [1..J]$ are shown in the boxplots in Fig. 5.7(g) and Fig. 5.8(g), respectively. As explained in Sec. 5.3.2, we choose s^* as the one that minimizes the mean values of the absolute error maps $\mathbf{D}_{p^{*\mathbf{S}}}(s_j), j = [1..J]$. This is identified at $s^* = 1250$m, see Fig. 5.7(g). From the statistics of the uncertainty maps $\mathbf{U}^{\mathbf{S}}_{p^{*\mathbf{S}}}(s_j)$, which are shown qualitatively in Fig. 5.8(g), the following can be derived. First, the mean values of $\mathbf{U}^{\mathbf{S}}_{p^{*\mathbf{S}}}(s_j)$ increase for larger scales. This is due to the fact that at larger scales the rescaled RS samples used by the OK method, i.e., $S^{RS}(s_j)$, are more sparse than at short scales, thus leading to more uncertain estimates. However, this negative trend

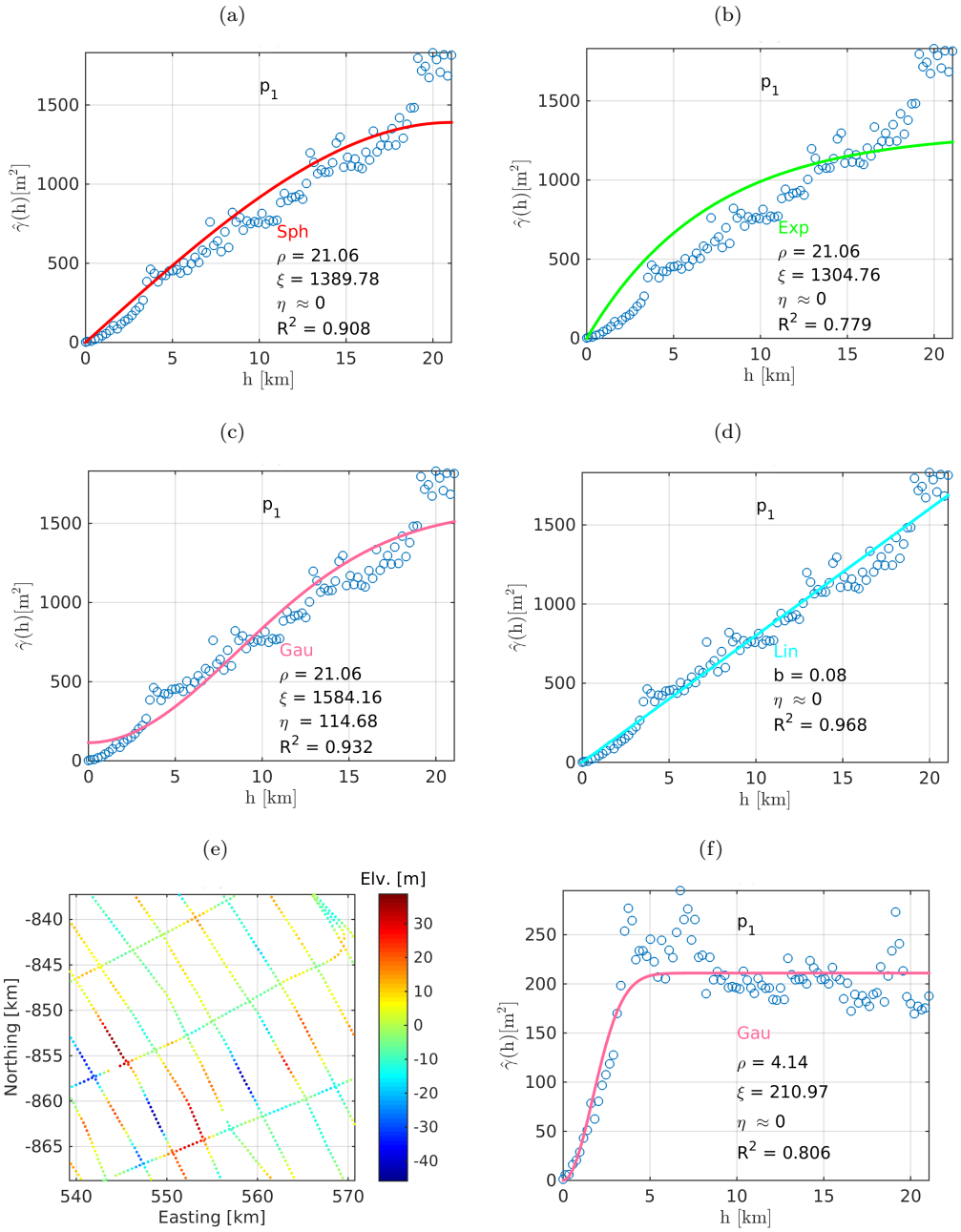

Figure 5.6: Example of model fitting and associated estimated vector of parameters of the semivariogram of $S^{RS}(500)$ generated with the parameter set $p_1 = \{\text{bw}, \mathbf{W}1\}$. a) Spherical model, b) Exponential model, c) Gaussian model, d) Linear model, e) Scatterplot of the residuals obtained by subtracting the values of the fitted surface from the initial $S^{RS}(500)$, f) Fitting performances on the semivariogram regenerated with the parameter set $p_1 = \{\text{bw}, \mathbf{W}1\}$ on the residuals shown in Fig. 5.6(e); quantitatively, the best fitting model is the Gaussian model with $R^2 = 0.806$ and $\theta = (4.14\text{km}, 210.97\text{m}^2, 0\text{m}^2)$.

towards large scales is compensated by the smaller standard deviations of $\mathbf{U}^{\mathbf{S}}_{p^{*\mathbf{S}}}(s_j)$ towards large scales. This is due to the fact that, not only the $S^{RS}(s_j)$ are sparser, but also the query points are less at larger scales, leading to more similar uncertainties for neighboring query points. Therefore, it can be derived that at the most reliable scale s^*, the overall uncertainty is relatively good (see Fig. 5.8(g)), i.e., with a mean value of 15m. The parameter set that provides the lowest overall uncertainty at s^* is $p^{*\mathbf{S}} = p_8 = \{\text{bs}, \mathbf{W}5\}$. The best fitting model of the empirical semivariogram at s^* is highlighted in bold italics in Tab. 5.3.

Table 5.3: Best fitting models and estimated vector of parameters obtained with all OK parameter sets, at all investigated scales, on the ice surface samples. The results obtained with the parameter set that provides the lowest mean uncertainty at a given scale are highlighted in bold. The results obtained at the best scale are highlighted in bold italics.

Scale	Model	OK parameter set							
		p_1	p_2	p_3	p_4	p_5	p_6	p_7	p_8
500	Name	gauss	gauss	gauss	gauss	gauss	gauss	gauss	**gauss**
	ρ[km]	4.14	3.79	4.44	4.11	4.47	4.10	4.55	**4.92**
	ξ[m^2]	210.97	208.37	215.67	212.19	227.63	208.45	212.58	**227.83**
	η[m^2]	≈ 0	≈ 0	4.22	3.00	1.31	≈ 0	≈ 0	$\approx$ **0**
750	Name	gauss	gauss	gauss	gauss	gauss	gauss	**gauss**	spher
	ρ[km]	4.13	3.78	4.49	4.07	4.49	4.10	**4.60**	6.79
	ξ[m^2]	210.85	207.66	217.11	212.29	227.33	207.34	**212.02**	223.02
	η[m^2]	≈ 0	≈ 0	3.64	3.01	1.36	≈ 0	$\approx$ **0**	≈ 0
1000	Name	gauss	gauss	gauss	gauss	gauss	gauss	gauss	**spher**
	ρ[km]	4.02	3.74	4.26	4.06	4.38	4.12	4.57	**6.70**
	ξ[m^2]	206.17	204.25	211.79	209.04	221.74	204.86	209.70	**219.93**
	η[m^2]	≈ 0	≈ 0	3.80	3.06	1.74	≈ 0	≈ 0	$\approx$ **0**
1250	Name	gauss	gauss	gauss	gauss	gauss	gauss	gauss	***spher***
	ρ[km]	4.12	3.81	4.57	4.16	4.63	4.13	4.65	***6.67***
	ξ[m^2]	204.42	201.83	212.03	207.66	222.25	202.48	208.36	***217.55***
	η[m^2]	≈ 0	≈ 0	2.54	1.91	2.97	≈ 0	≈ 0	$\approx$ ***0***
1500	Name	gauss	gauss	gauss	gauss	gauss	gauss	gauss	**spher**
	ρ[km]	3.98	3.74	4.14	3.94	4.46	4.14	4.52	**6.59**
	ξ[m^2]	200.73	198.26	210.14	205.91	217.28	199.84	206.67	**214.23**
	η[m^2]	≈ 0	≈ 0	1.88	1.63	2.11	≈ 0	≈ 0	$\approx$ **0**
1750	Name	gauss	gauss	gauss	gauss	gauss	gauss	gauss	**spher**
	ρ[km]	4.09	3.80	4.46	4.19	4.53	4.18	4.70	**6.71**
	ξ[m^2]	197.71	195.15	206.41	202.69	212.98	197.27	204.74	**212.27**
	η[m^2]	≈ 0	≈ 0	5.58	4.33	0.17	≈ 0	≈ 0	$\approx$ **0**

The most reliable scale s^* is then used for interpolating the bedrock samples $B^{RS}(s_0)$ as explained in Sec. 5.3.3. Tab. 5.4 reports the best fitting model and its associated

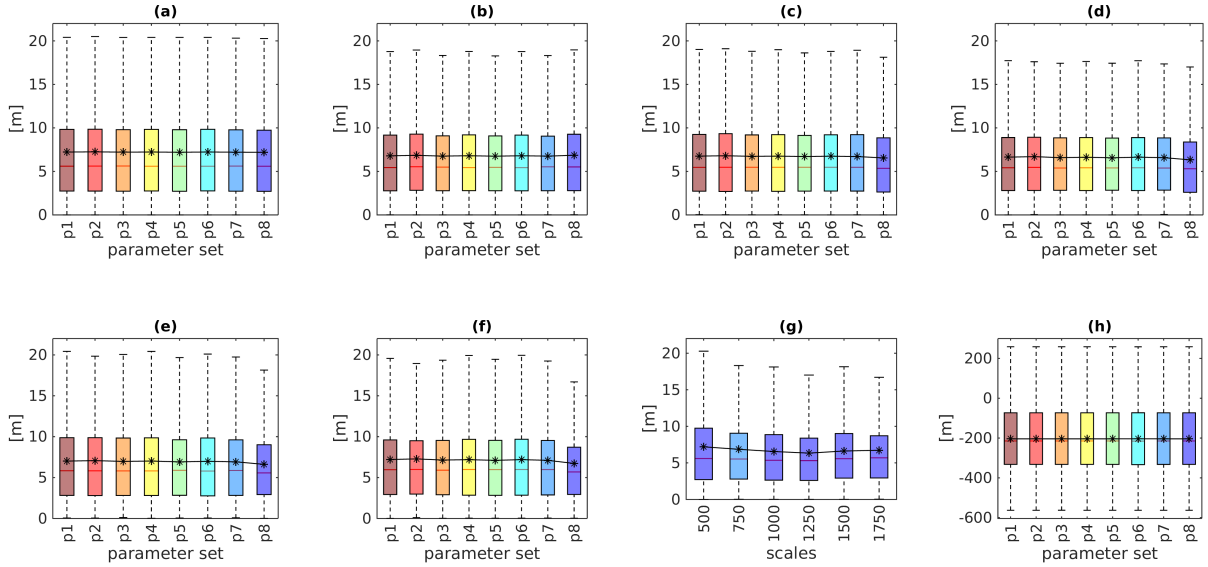

Figure 5.7: Statistical representation of the obtained results. Boxplots of $\mathbf{D}_{p_i^{\mathbf{S}}}(s_j), i = [1..P]$ at scales: (a) $s_1 = 500$m, (b) $s_2 = 750$m, (c) $s_3 = 1000$m, (d) $s_4 = 1250$m, (e) $s_5 = 1500$m, (f) $s_6 = 1750$m, (g) Boxplots of $\mathbf{D}_{p^{*\mathbf{S}}}(s_j), j = [1..J]$, (h) Boxplots of $\mathbf{B}^{RS}_{p_i^{\mathbf{B}}}(s^* = 1250), i = [1..P]$. Each color is associated to a parameter set. The asterisks '*' are placed at the mean value of the boxplots and linked in order to highlight the mean overall variability of the analysed maps.

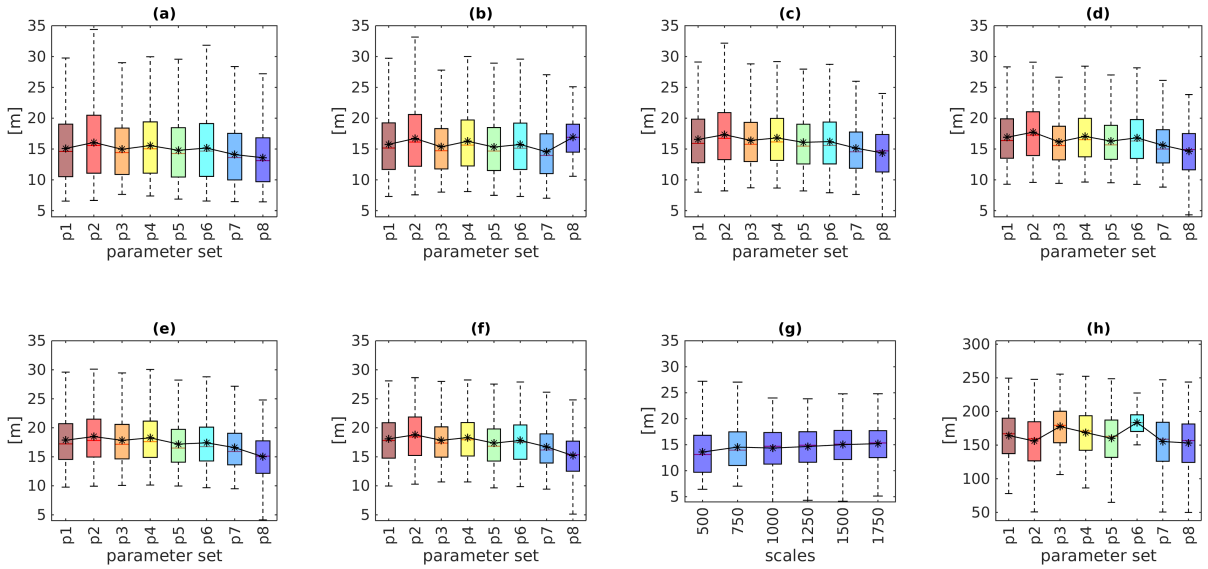

Figure 5.8: Statistical representation of the obtained uncertainty maps. Boxplots of $\mathbf{U}^{\mathbf{S}}_{p_i^{\mathbf{S}}}(s_j), i = [1..P]$ at scales: (a) $s_1 = 500$m, (b) $s_2 = 750$m, (c) $s_3 = 1000$m, (d) $s_4 = 1250$m, (e) $s_5 = 1500$m, (f) $s_6 = 1750$m, (g) Boxplots of $\mathbf{U}^{\mathbf{S}}_{p^{*\mathbf{S}}}(s_j), j = [1..J]$, (h) Boxplots of $\mathbf{U}^{\mathbf{B}}_{p_i^{\mathbf{B}}}(s^* = 1250), i = [1..P]$. Each color is associated to a parameter set. The asterisks '*' are placed at the mean value of the boxplots and linked in order to highlight the mean overall variability of the analysed maps.

vector of estimated parameters related to the different OK parameter sets for $B^{RS}(s^*)$. On the basis of these results, we estimate the bedrock maps $\mathbf{B}^{RS}_{p_i^{\mathbf{B}}}(1250), i = [1..P]$ and uncertainty maps $\mathbf{U}^{\mathbf{B}}_{p_i^{\mathbf{B}}}(1250), i = [1..P]$. Fig. 5.7(h) and Fig. 5.8(h) show the boxplots of $\mathbf{B}^{RS}_{p_i^{\mathbf{B}}}(1250), i = [1..P]$ and $\mathbf{U}^{\mathbf{B}}_{p_i^{\mathbf{B}}}(1250), i = [1..P]$, respectively. The parameter set that provides the lowest overall uncertainty is $p^{*\mathbf{B}} = p_8 = \{\text{bs}, \mathbf{W}5\}$. The best fitting model of the empirical semivariogram at s^* is highlighted in italics in Tab. 5.3.

It is worth analyzing the results obtained for the surface and bedrock in terms of uncertainty values. As it can be seen from Fig. 5.8(g)-(h), the uncertainties obtained by interpolating the surface samples at 1250m are in the range [13-17]m, whereas the uncertainties obtained by interpolating the bedrock samples are in the range [130-200]m. This is explained by the fact that the variability of the bedrock samples at short range is very high, i.e., in the same order of magnitude with the scale s^*. The variability of the surface and bedrock samples can be compared in Fig. 5.9(a) and Fig. 5.9(b), which show the scatterplots of $S^{RS}(1250)$ and $B^{RS}(1250)$, respectively. Note both the different dynamic range of values and the different variability in local neighborhoods of the surface and bedrock samples. This short range variability is captured also by the semivariograms and best fitting models of $S^{RS}(1250)$ (see Fig. 5.9(c)) and $B^{RS}(1250)$ (see Fig. 5.9(d)). As it can be seen, $S^{RS}(1250)$ is better modeled by the Spherical model, with $\theta = (6.67\text{km}, 217.55\text{m}^2, 0\text{m}^2)$, whereas $B^{RS}(1250)$ is better modeled by the exponential model, with $\theta = (21.12\text{km}, 39623\text{m}^2, 0\text{m}^2)$(see Appendix B 5.6). Moreover, recall that the best parameter set for both $S^{RS}(1250)$ and $B^{RS}(1250)$ is $p^{*\mathbf{S}} = p^{*\mathbf{B}} = p_8 = \{\text{bs}, \mathbf{W}5\}$. This means that, given the characteristics of the input RS data (see Tab. 5.2), the semivariograms that provide the highest overall quality maps of both surface and bedrock elevation at scale s^* are generated with the binsize method. This can be explained by the fact that with the binsize method a sufficient number of RS point pairs falls in each bin to ensure a consistent statistical analysis. Given the particularity of the RS data, the same is not necessarily true in the case of the binwidth method. Moreover, different works have demonstrated the importance of a good semivariogram fit near the origin in order to ensure good interpolation performances. This result is confirmed also by our study, i.e., the best fitting model of these semivariograms is determined by using the Zhang [97] weighting function, $\mathbf{W}5$, which gives more weight to the semivariogram bins near the origin.

The final estimated surface and bedrock elevation maps at scale $s^* = 1250$m, both obtained with the best parameter set $p_8 = \{\text{bs}, \mathbf{W}5\}$ are provided in Fig. 5.10(a)-(b). The thickness map at 1250m is provided in Fig. 5.10(c).

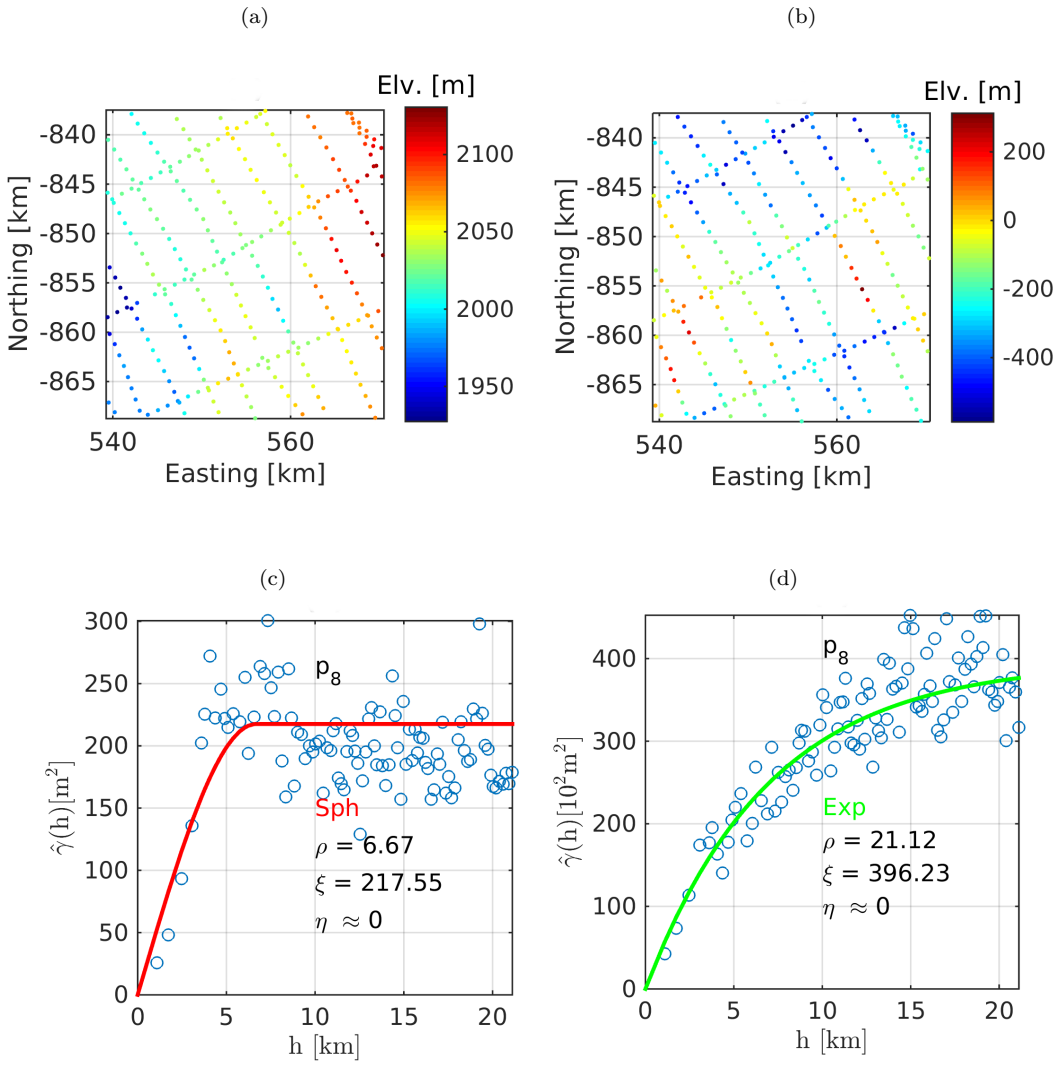

Figure 5.9: (a) Scatterplot of the surface samples rescaled at the most reliable scale, i.e., $S^{RS}(1250)$, (b) Scatterplot of the bedrock samples rescaled at the most reliable scale, i.e., $B^{RS}(1250)$, (c) Semivariogram best fit of $S^{RS}(1250)$, using the best parameter set $p^{*\mathbf{S}} = p_8 = \{\text{bs}, \mathbf{W}5\}$, (d) Semivariogram best fit of $B^{RS}(1250)$, using the best parameter set $p^{*\mathbf{B}} = p_8 = \{\text{bs}, \mathbf{W}5\}$.

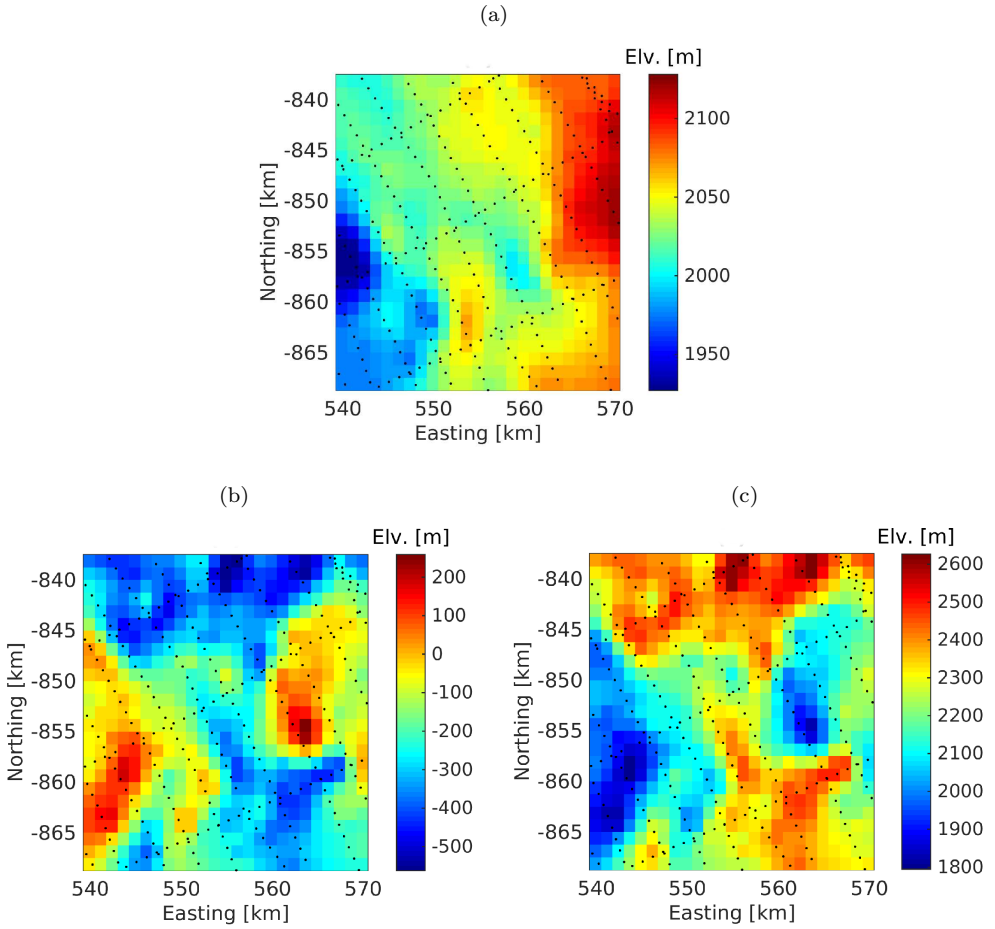

Figure 5.10: Estimated maps at $s^* = 1250$. (a) Ice surface map, (b) Bedrock map, (c) Ice thickness map.

Table 5.4: Best fitting models and estimated vector of parameters obtained for the bedrock samples, with all OK parameter sets, at $s^* = 1250$m. The results obtained with the parameter set that provides the lowest mean uncertainty are highlighted in italics.

Scale	Model	OK parameter set							
		p_1	p_2	p_3	p_4	p_5	p_6	p_7	p_8
1250	Name	expon	expon	expon	expon	expon	spher	expon	***expon***
	ρ[km]	21.10	20.55	21.10	21.10	20.77	17.17	21.12	***21.12***
	$\xi[10^2\text{m}^2]$	400.48	399.99	398.96	404.19	399.77	374.26	407.12	***396.23***
	$\eta[10^2\text{m}^2]$	9.40	≈ 0	23.16	12.98	4.39	55.18	≈ 0	$\approx$ ***0***

5.5 Conclusion

In this Chapter we have provided a contribution to the problem of 3D modeling of the ice sheet. In particular, we proposed an automatic method for the local 3D reconstruction of the ice sheet. The method exploits the complementary properties of the RS and ALT data. It uses the geostatistical OK method to interpolate at different scales and with different OK parameter sets the elevation measurements extracted from the RS data. It relies on the use of several statistical measures for investigating the interpolation results and the quality of interpolation at the considered scales. The highest quality map at a certain scale is the one with the lowest overall uncertainty among all maps generated at that scale with different OK parameter sets. The most reliable scale is chosen by comparing the highest quality ice surface elevation map at each scale against rescaled ALT data, which are considered as reference. Results obtained by validating the method on a subset of RS data acquired by MCoRDS and ALT data acquired by the GLAS/ICESat over a portion of the Byrd Glacier in Antarctica confirm its effectiveness.

According to our results, for the considered datasets the most reliable scale for interpolation is at 1250m. This means that at 1250m, we obtained the lowest mean absolute error between the ice surface elevation map generated by interpolating the rescaled RS measurements with the OK algorithm and the rescaled reference ALT data. Moreover, the estimated ice and bedrock elevation maps have the highest overall quality among several maps generated with different OK parameter sets at 1250m.

The generated maps are a result of a detailed SVA performed on the rescaled ice surface and bedrock RS samples. We obtained that on our datasets the ice surface and bedrock interface are best represented by the Spherical and Exponential models, respectively. This highlights the higher variability (in elevation) of the bedrock samples with respect to the surface samples. Moreover, the identified Spherical and Exponential models are both fitted on the empirical semivariograms generated with a constant number of samples in each bin. Given the particularities of the RS data, this ensures that there are enough samples

in each bin for performing a consistent statistical analysis. The identified Spherical and Exponential models are fit with the weighting function proposed in [97]. This confirms a result already derived in the literature, i.e., more accurate estimates are given by theoretical models that provide a good fit of the empirical semivariogram near the origin (indeed the weighting function proposed in [97] gives more weight to bins close to 0).

As future developments, we plan to study the possibility to refine the estimated 3D maps by including in the method possible known input data uncertainties and their effects on the results provided by the adopted geostatistical interpolation strategy. Another development consists in enlarging the parameter set with a subset that considers different ways of selecting the samples or the number of samples used in the interpolation. We recall that in this work for the estimation at a certain query point, we considered its 10 nearest observed samples. However, a different number or another selection criteria (e.g., quadrant search) can be considered. Moreover, we aim to include in the study the modeling of possible anisotropic behavior of the ice sheets. Anisotropy is most likely to appear along the ice streams or in mountainous areas, due to the preferred direction of snow deposition and accumulation or flow. Therefore, we plan to adapt and apply the method to the 3D modeling of the ice subsurface also in these particular regions of the ice sheets.

5.6 Appendix B

In this Appendix, the equations of the theoretical models used for fitting the empirical semivariogram are given.

– The Spherical model:

$$\gamma^{Sph}(h;\theta) = \begin{cases} 0, h = 0, \\ \eta + (\xi - \eta)[\frac{3}{2} \cdot \frac{h}{\rho} - \frac{1}{2}(\frac{h}{\rho})^3], 0 < h \leq \rho, \\ \xi, h > \rho, \end{cases} \tag{5.10}$$

– The Exponential model:

$$\gamma^{Exp}(h;\theta) = \begin{cases} 0, h = 0, \\ \eta + (\xi - \eta)[1 - e^{-\frac{3h}{\rho}}], h > 0, \end{cases} \tag{5.11}$$

– The Gaussian model:

$$\gamma^{Gau}(h;\theta) = \begin{cases} 0, h = 0, \\ \eta + (\xi - \eta)[1 - e^{-\frac{3h^2}{\rho^2}}], h > 0. \end{cases} \tag{5.12}$$

$\theta = (\rho, \xi, \eta)$ is the vector of parameters of these models, where the range ρ is the distance after which the samples lose spatial correlation, the sill ξ is the value that the semivariogram has at ρ, and the nugget η is associated with measurement errors and variations at microscales smaller that the distances between the available samples.

– The Linear model:

$$\gamma^{Lin}(h;\theta) = \begin{cases} 0, h = 0, \\ \eta + \flat h, h > 0, \end{cases} \tag{5.13}$$

where $\flat$ is the slope and η is the value of the semivariogram where the line fitted to the data intersects the y-axis.

Chapter 6

Estimation of Radar Power Losses in Ice by Using Radar Sounder and Ice Core Data

This Chapter[1] *provides a contribution to the problem of understanding the radar wave interaction with the ice sheet. In particular, we propose a method for the estimation of radar power losses in ice by fusing RS and ice core data. The objective of the method is the estimation of power losses through ice as a continuous non-linear function of depth, rather than the estimation of the ice power loss rate. The technique uses coincident RS and ice core data. It relies on the detection of ice layers in the RS data, the computation of their depth and reflectivity by fusing RS and dielectric permittivity profile (DEP) data collected at the ice core, and the use of the radar equation for ice power loss estimation as a discrete function of depth. Then, a continuous non-linear function is fitted to the discrete power losses and extrapolated to the bedrock in order to estimate the losses through the whole ice column. Although the method has been defined, at present it has not been fully implemented and validated. However, the preliminary results obtained by applying the technique to real RS and DEP ice core data acquired in Greenland encourage further research.*

6.1 Introduction and background

The importance of better understanding the interaction of the radar wave with the ice sheet has been often highlighted by the scientific community. It is well understood that

[1]The work has been carried out during a period of 3 months (mid June - mid September, 2014) as visiting PhD student at the Center for Remote Sensing of Ice Sheets (CReSIS), Lawrence, Kansas, USA, under the supervision of Prof. Prasad Gogineni and Dr. Jilu Li. At the time of writing the work is still under development.

the reduction of the wave power is due to geometric spreading losses in air and ice, wave reflection and scattering at the ice surface, internal layers and underlying bedrock, and attenuation in the subsurface [3]. The geometric losses depend on the distance between sensor and target, the reflection and scattering losses depend on the interface roughness, and the ice attenuation results from ice impurity and conductivity, which is a function of instrument working frequency and ice temperature [100]. Therefore, at constant RS central frequency, a variable temperature within the ice sheet implies a variable ice attentuation both as a function of depth and location. However, most works in the literature (see Sec. 2.3) assume a linear trend of the power attenuation and thus estimate a constant rate of power attenuation. In this work, we propose a technique for the estimation of ice power losses as a continuous non-linear function of depth and location, rather than the estimation of the ice power loss rate. This results in a more reliable estimation of the losses on wide areas, which is fundamental for a better understanding of the radar wave interaction with the ice subsurface and for a better modeling of the processes taking place within the ice sheet and at the basal interface (e.g., reduction of the uncertainties related to the boundary conditions [55]).

The method fuses RS and dielectric profile (DEP) data that are coincident at the ice core position, and is based on a layer-driven approach (see Sec. 2.3). This implies the use of information about the layers visible in the radargram rather than information about the bedrock reflected power. As already mentioned in the previous Chapters of the thesis, the ice internal layers have been generated over millennia by snow accumulation on the underlying bedrock, alternated by depositions of impurities from volcanic explosions [67], and ice flow dynamics [68], therefore they have an isochronous character [57] (see Sec. 3.2). As stated in [58], an important consequence of the isochronous character of the ice layers is the fact that it allows the findings at any given drill site to be extrapolated over a region covered by a RS survey that passes through the drill site. This statement motivates our choice of fusing the RS and ice core data and the use of the layer-driven approach to provide additional information about the radar power losses through ice on wide areas.

6.2 Proposed method for ice loss estimation

6.2.1 Problem formulation and architecture of the proposed method

A radargram is a 2D matrix that contains the power reflected by interfaces in the ice subsurface and measured by the RS receiver as a function of 2WTT Λ to the interface (or sample $i = [1..n_S]$) in the range direction, and as a function of platform position (or trace $t = [1..n_T]$) in the along-track direction. An ice dielectric profile (DEP) contains

measurements of the dielectric permittivity of the ice along the ice column. Our technique fuses RS and DEP data, which we assume coincident at the ice core position $t = t^c$.

The proposed method is a trace-based technique which relies on the use of the radar equation at each trace and assumes that the ice internal layers visible in the radargram are dominated by specular reflections. By adapting the general radar equation (see the simplified form of the radar equation in (1.2)) to a RS (i.e., nadir-looking geometry, subsurface penetration), the power P_k measured by the RS at trace t from a specular layer k located at a depth Z_k, is given by:

$$P_k = P_{tx} \cdot \left(\frac{\lambda}{4\pi}\right)^2 \cdot \frac{G^2}{\left[2\left(H + \frac{Z_k}{\sqrt{\varepsilon_k}}\right)\right]^2} \cdot L_k^2 \cdot \Upsilon_s^2 \cdot \Gamma_k, \tag{6.1}$$

where P_{tx} is the transmitted pulse power, λ is the wavelength, H is the height of the RS platform with respect to the surface, G is the gain of the antenna, ε_k is the dielectric permittivity at layer k and L_k is the one way power loss due to the ice attenuation until layer k. Γ_k is the reflectivity of the layer k, and is given by the dielectric contrast, according to the following equation:

$$\Gamma_k = \left|\frac{\sqrt{\varepsilon_{k^-}} - \sqrt{\varepsilon_{k^+}}}{\sqrt{\varepsilon_{k^-}} + \sqrt{\varepsilon_{k^+}}}\right|^2, \tag{6.2}$$

where ε_{k^-} and ε_{k^+} are the dielectric permittivities before and after the interface. Υ_s is the transmission coefficient of the surface and is given by:

$$\Upsilon_s = 1 - \rho_s \Gamma_s, \tag{6.3}$$

where ρ_s is the reflection reduction due to surface roughness and $\Gamma_s = 0.029$ (which is equivalent to -15.31dB) is the reflectivity of the surface, obtained with (6.2) by setting $\varepsilon_{k^-} = \varepsilon^{air} = 1$ and $\varepsilon_{k^+} = \varepsilon^{snow} = 2$. It is important to note that by using (6.1) we implicitly assume an ice sheet simplified model composed of two interfaces, i.e., the ice surface and the layer k, as depicted in Fig. 6.1. The intermediate $k-1$ internal layers are assumed to have a transmission coefficient close to 1, because of their very low reflectivity. For this reason and for the sake of clarity, the product of transmission coefficients until layer k is omitted in (6.1).

By expressing the received power from layer k in realtion to the received power from the surface, the derived power ratio is independent on the parameters of the RS, which is given by:

$$\frac{P_k}{P_s} = \frac{(1 - \rho_s \Gamma_s)^2 \Gamma_k}{\rho_s \Gamma_s} \cdot \left(\frac{H}{H + \frac{Z_k}{\sqrt{\varepsilon_k}}}\right)^2 \cdot L_k^2, \tag{6.4}$$

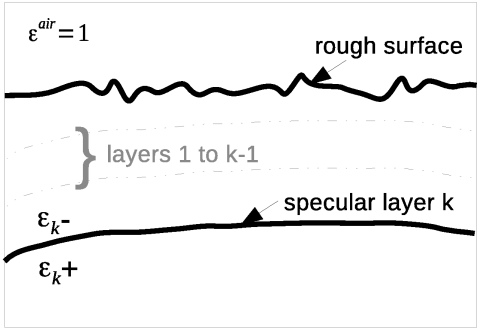

Figure 6.1: Two interface model of the ice sheet.

where P_s is the received power from the surface, given by:

$$P_s = P_{tx} \cdot \left(\frac{\lambda}{4\pi}\right)^2 \cdot \frac{G^2}{(2H)^2} \cdot \rho_s \Gamma_s. \tag{6.5}$$

Moreover, by inverting (6.4) one can derive L_k:

$$L_k = \left[\frac{P_s}{P_k} \cdot \frac{\rho_s \Gamma_s}{(1-\rho_s \Gamma_s)^2 \Gamma_k} \cdot \left(\frac{H + \frac{Z_k}{\sqrt{\varepsilon_k}}}{H}\right)^2\right]^{1/2}. \tag{6.6}$$

It is worth noting that L_k can be estimated for all layers k and for all traces t with (6.6) as a discrete function of layer depths Z_k and other properties of the surface and layers, i.e., surface reflectivity, power and roughness reduction coefficient, and layer power and reflectivities, which are all unknown quantities, to be estimated from the data.

In this work we aim to estimate the ice power losses for all traces t, as a continuous non-linear function $\mathcal{L}$ of depth, starting from the discrete form expressed by (6.6). To this aim, we propose a method composed of 5 blocks. The block scheme of the technique is depicted in Fig. 6.2. In particular, the first block performs the surface and bedrock detection, and surface roughness estimation from the radargram, in order to provide the required P_s and ρ_s at all positions t of the platform. The second block performs the layer detection and provides the 2WTT Λ_k and the power P_k of K continuous specular layers visible in the radargram. The depth of the layers Z_k at the position t^c of the DEP and the reflectivity of the layers Γ_k are estimated in the third block of the technique by fusing the RS and DEP data. At this point all the unknowns, i.e., P_s, P_k, ρ_s, Γ_s, Γ_k, Z_k, ε_k in (6.6) are estimated, and thus the discrete losses L_k at the depth of each layer k at the DEP position t^c can be calculated. Moreover, the considered two interface model of the ice sheet and the assumption that the layers are dominated by specular reflections (i.e., the reflectivity Γ_k of each layer is constant along the layer k) allows us to estimate their depth and consequently the corresponding power losses L_k for all traces t. We perform

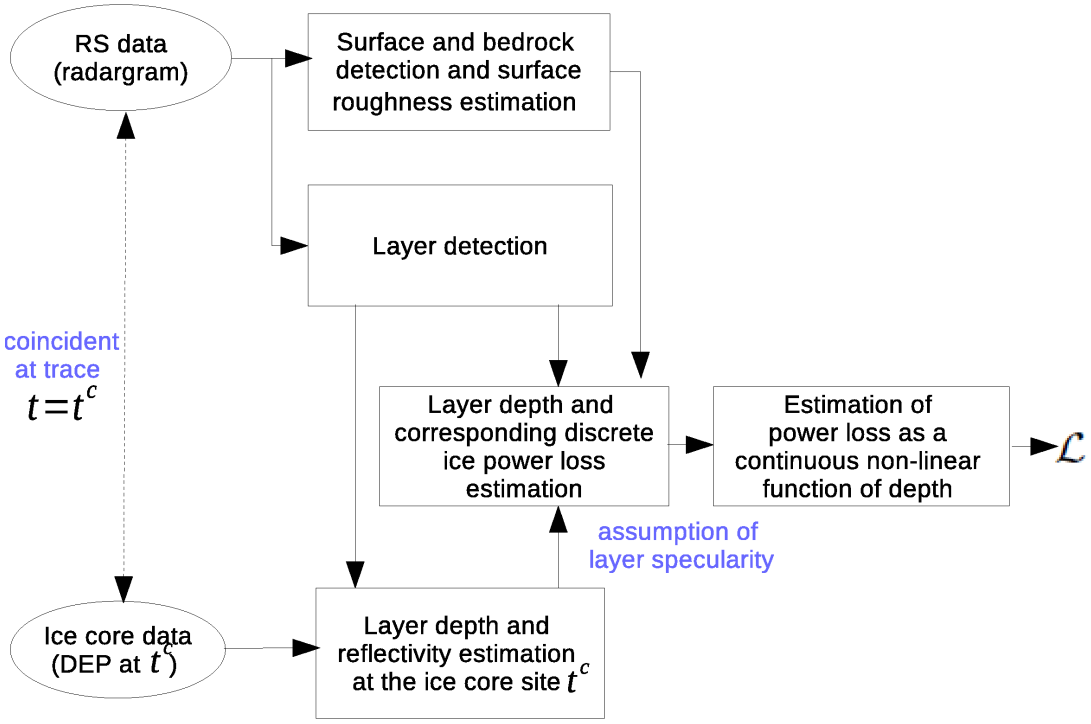

Figure 6.2: Block scheme of the proposed technique for the ice power loss estimation.

this in the fourth block of the technique. Finally, in the fifth block we estimate the power losses as a continuous non-linear function $\mathcal{L}$ of depth by fitting and extrapolating to the bedrock a theoretical function to the estimated discrete losses L_k, for all traces t.

In the following subsections, a detailed description of each of the processing steps of the method is given.

6.2.2 Step 1: Surface and bedrock detection and estimation of reflection reduction due to surface roughness

The objective of this step is the detection of surface and bedrock positions, and the estimation of the surface power P_s and of the reflection reduction ρ_s, for the entire radargram.

The surface and bedrock positions can be traced manually or according to automatic techniques, e.g., see Chapter 3, Chapter 4, [19]. Once the surface position and the related power P_s are extracted from the radargram, we use them to estimate the surface roughness parameters, i.e., the root mean square height RMSH σ_h and the correlation lenght LC, which are in turn used to estimate ρ_s. In particular, σ_h represents the vertical displacement of the surface with respect to its mean plane, whereas LC is the horizontal length over which the samples are correlated.

Under the condition that several surface vertical undulations are simultaneously illuminated by the radar (i.e., $LC \ll DF$, where DF is the first Fresnel zone (see (1.12)), the RMSH introduces a phase variation Φ which reduces the specularly reflecting power by a factor ρ_s, defined as [101]:

$$\rho_s = \exp^{-\Phi^2} B_0^2(\Phi^2/2), \tag{6.7}$$

where $B_0(\cdot)$ is the zero-order modified Bessel function, and Φ is given by:

$$\Phi = \frac{4\pi\sigma_h}{\lambda}. \tag{6.8}$$

Φ can be estimated according to Neal's approach [102] from the probability distribution of the received power returns from the surface. Accordingly, we fit a theoretical model $\mathcal{M}$ (derived in [102]) with varying parameter Φ to the real histogram $\mathcal{H}$ of the surface power collected from a statistically sufficient number n^t of neighboring traces. The best fit, which we identify by minimizing the KL measure between the distributions $\mathcal{H}$ and $\mathcal{M}$ (see (3.1)), provides Φ. It is worth noting that the Neal's method is applicable only to small-scale roughness, i.e., surfaces with a RMSH that generates a phase modulation $\Phi < 0.3$. If the estimated Φ satisfies this condition, we also verify the condition $LC \ll DF$, in order to apply (6.7) to estimate ρ_s. LC is estimated with an iterative approach from the normalized power variance v_p [102]:

$$v_p = \frac{E\{P_s^2\}}{(E\{P_s\})^2} - 1 = 2\Phi^2 \left[\frac{1}{1 + \frac{\lambda^2 H}{2\pi^2 LC^2 \tau}} - \frac{1}{1 + \frac{\lambda H}{\pi LC^2}} \right], \tag{6.9}$$

where τ is the pulse time and $E\{\cdot\}$ denotes the expectation operation.

If the two conditions (i.e., $\Phi < 0.3$ and $LC \ll DF$) hold, the surface is characterized by small-scale roughness and ρ_s can be estimated with (6.7). Otherwise, the surface is characterized by large-scale roughness (with respect to the wavelength) and other methods should be used for the estimation of σ_h, LC and ρ_s. Note that at the time of writing such methods have not been yet investigated and implemented in our technique.

6.2.3 Step 2: Layer detection

The objective of this step is the detection of the well-defined ice internal layers $k = [1..K]$ and the computation of their power P_k for all the traces t of the radargram. To this aim we use the method proposed in [26]. The method uses the phase information measured by the RS and detects the layers based on the analysis of the Doppler spectrum (for further details on the method the reader is refered to [26]). We apply this method and detect the power of the layers P_k and their position as a function of 2WTT Λ_k, along the entire

radargram. Afterwards, we select only those K layers that are passing through the ice core site and are continuous over the radargram. The layer continuity is required for the estimation of the ice power losses on all the traces of the radargram (see Sec. 6.2.5), by assuming that the layer reflectivity, which can be estimated at the ice core site (see Sec. 6.2.4), is constant along the layer.

6.2.4 Step 3: Layer depth and reflectivity estimation at the ice core site

The aim of this step is the computation of the layer depths and reflectivities. Initially, we achieve this at the ice core position $t = t^c$ by fusing the DEP data with information extracted from the RS data. Note that the DEP data is available in the depth domain, i.e., a measurement of dielectric permittivity is taken every δ_z^{DEP}[m], where δ_z^{DEP} is the vertical resolution of the DEP profile. On the contrary, the layers at the ice core are detected in the time domain, i.e., as a function of 2WTT. Thus, in order to match the layers visible in the radargram at $t = t^c$ to their position in the DEP profile, a conversion from time to depth should be performed. By doing so both the layer depth and reflectivities can be computed with high accuracy. This is performed in 3 main steps: i) conversion of the DEP depth to time domain and matching of Λ_k extracted from the radargram at the DEP site, ii) extraction of ε_{k^-} and ε_{k^+} for the computation of Γ_k with (6.2), and iii) back conversion from time to depth domain for the estimation of the layer depth Z_k, by considering the whole DEP until layer k. This sequence of operations is done for all layers $k = [1..K]$ detected in the radargram at the DEP ice core site t^c.

It is important to highlight that the layer depths are typically computed by using the range to target equation (1.1), in which a constant dielectric permittivity of ice $\varepsilon^{ice} = 3.15$ is assumed. However, with this approximation the layer depths are under- or over-estimated, leading to an incorrect layer depth matching in the DEP and consequently to an incorrect layer reflectivity estimation. On the contrary, the availability of the DEP allows for an improved estimation of the layer depth and reflectivity, as previously explained.

6.2.5 Step 4: Layer depth and corresponding discrete ice power loss estimation

The objective of this step is two-fold: i) the estimation of the layer depths on all the traces of the radargram, and ii) the estimation of the discrete one way power loss at the estimated layer depths.

The computation of the layer depths in the whole radargram is done similarly to what implemented for estimating the layer depths at the DEP site (see Sec. 6.2.4). The only difference is that for all traces $t \neq t^c$ there is no information on the dielectric profile.

Therefore, in order to estimate the layer depths Z_k, we assume that between the surface and the layer k at traces $t \neq t^c$, the dielectric profile is a scaled version of the DEP between the surface and the layer k at the ice core t^c. It is worth noting that this is a consequence of the two interface ice sheet model that we are considering (see Sec. 6.2.1). For a multilayer model, one can assume that between each two adjacent layers k and $k+1$ at traces $t \neq t^c$, the dielectric profile is a scaled version of the DEP between k and $k+1$ at the ice core t^c. Furthermore, under the assumption that the layers are characterized by specular reflections, Γ_k computed at the DEP site t^c (see Sec. 6.2.4) is constant along the layer, therefore known for all traces t. We verify the assumption on the specularity of the layers by analyzing the along-track coherence of the layers and their behavior as a function of incidence angle, as done in [26].

At this stage, the one way power loss $L_k, k = [1..K]$ can be computed as a discrete function of layer depth for each trace t by using (6.6), in which all the unknowns have been estimated as previously explained.

6.2.6 Step 5: Estimation of power losses as a continuous non-linear function of depth

The final aim of the proposed technique is the estimation of ice power losses as a continuous non-linear function $\mathcal{L}$ of depth, starting from the estimated discrete ice power losses at the layer depths $L_k, k = [1..K]$. To this aim, we propose the following trace-based approach. For each trace t, we regard the estimated discrete L_k as samples in the depth-power domain, to which we fit a theoretical non-linear function. Also, by extrapolating the function to the depth of the bedrock, we estimate the power losses throughout the ice column until the bedrock. The depth of the bedrock on all the traces of the radargram is estimated according to the approach used to estimate the layer depths (see Sec. 6.2.5), i.e., between the estimated surface and bedrock positions (see Sec. 6.2.2) at traces $t \neq t^c$, the dielectric profile is a scaled version of the DEP between the surface and bedrock positions at the ice core t_c. Regarding the fit, it is worth noting the impact of the fitting function on the estimation given the number K of layers and their distribution along the trace. In order to ensure a reliable and meaningful fit, a sufficient number K of samples should be available with an ideal uniform distribution with depth. Thus, the smaller K and the more complex the distribution of L_k with depth, the worse the fitting performances. Regarding the fitting function, we are investigating the fitting performances of more non-linear functions by considering a tradeoff between two main aspects, i.e., i) overfitting and ii) behaviour of the fitting function in the deep subsurface towards the bedrock. Indeed, the fitting function should have sufficient generalization capability, thus reduced sensitivity to outliers. On the other hand, the extrapolation of the fitting function towards

the bedrock should be constrained by the available temperature models, in order to ensure a reasonable ice power loss trend, i.e., a trend imposed by the physical characteristics of the ice.

6.3 Experimental results

At the moment of writing, the proposed ice loss estimation method has been only partially experimentally validated. In this Section we illustrate the preliminary results obtained so far.

We applied the proposed technique to RS data acquired by the MCoRDS instrument [14] and DEP data acquired at the NEEM ice core site [103] in Greenland. The RS data are acquired at low altitude, i.e., $H = 480$m above the surface, at central frequency $f_c = 195$MHz and bandwidth $B_w = 30$MHz. The data are range compressed and the range resolution is $\delta_z^{RS} = 4.3$m. The DEP data are acquired with a range resolution $\delta_z^{DEP} = 5$mm and are not temperature corrected. The proposed technique assumes RS and DEP data coincident at the ice core position. However, the investigated RS and DEP data are not perfectly coincident; the closest trace of the radargram to the ice core $t \approx t^c$ is at a distance of 1.6km. The geographic position of the input RS data and of the ice core are shown in Fig. 6.3(a), whereas the NEEM DEP profile is shown in Fig. 6.3(b). In order to ensure a sufficient number of continuous layers passing through the ice core site, we limit our preliminary analysis to a smaller portion of the input radargram, highlighted in black in Fig. 6.3(a) and illustrated as a function of 2WTT in Fig. 6.3(c). In this portion of the radargram a number of K =30 continuous layers passing through the closest trace to NEEM are detected. The first and last horizontal lines represent the positions of the surface and bedrock, respectively, whereas the intermediate 30 lines represent the positions of the specular layers detected as described in Sec. 6.2.3.

An initial analysis that we carried out regards the sensitivity of the method to the layer reflectivity, which we first estimated at the ice core site in 2 ways: i) reflectivity computed by assuming an approximate constant dielectric profile of $\varepsilon^{ice} = 3.15$ to estimate the layer depths, and ii) reflectivity computed by considering the available DEP to estimate the layer depths (see Sec. 6.2.4). Fig. 6.4(a) shows the depth offset at the ice core, obtained as the difference between the above mentioned approaches (i.e., correct depth estimated from the DEP and depth estimated by assuming constant $\varepsilon = 3.15$). As it can be seen, by assuming a constant dielectric permittivity of ice, the depth is underestimated along the whole ice column and the depth offset at the layer positions is in the range [8-13]m. This difference has a negative impact on the estimation of layer reflectivity, see Fig. 6.4(b). In this figure, the reflectivities of the layers at the estimated approximated depths

(a)

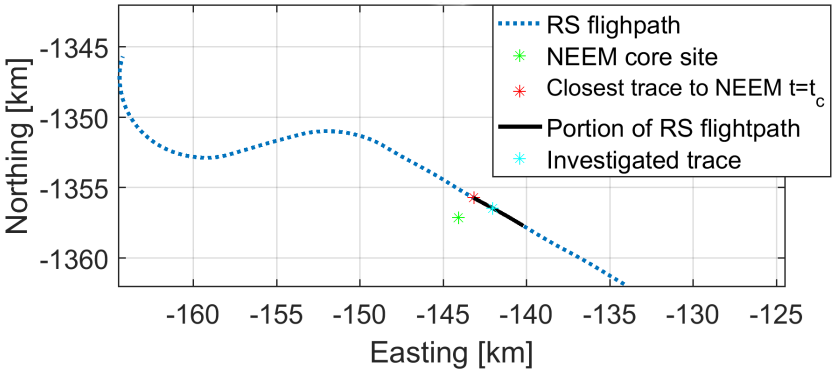

(b)

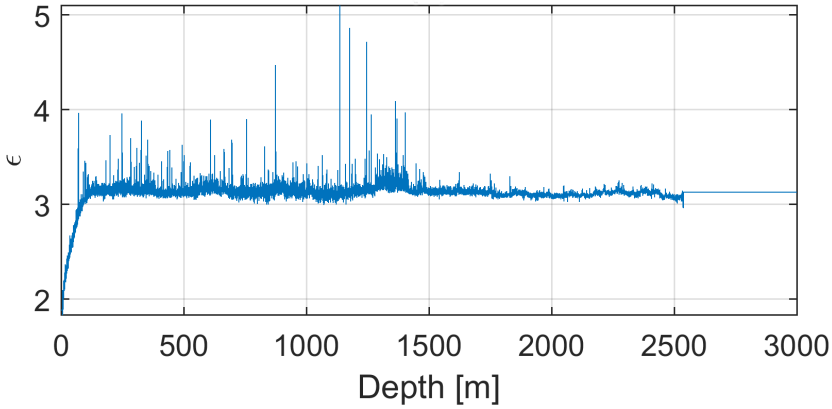

(c)

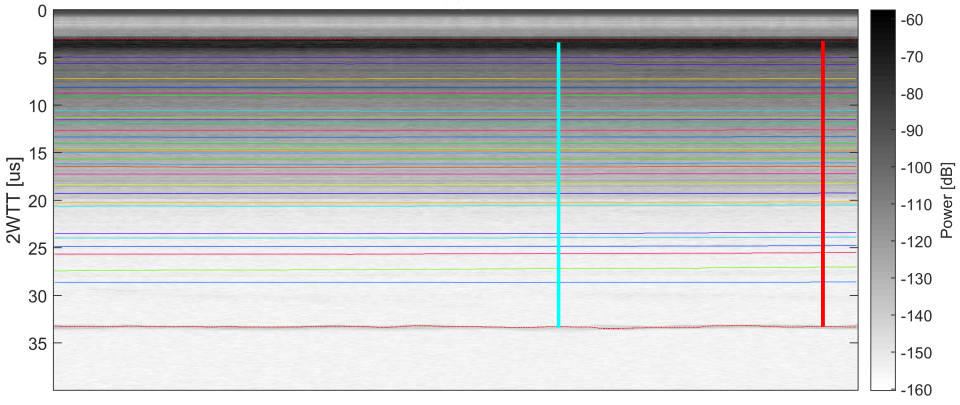

Figure 6.3: (a) Geographic position of the input RS data (blue dots), NEEM ice core (green), closest trace to NEEM $t = t_c$ (red), portion of the flightpath for which the acquired radargram contains 30 continuous layers passing through t_c), and investigated trace (cyan), (b) DEP profile at the NEEM ice core site, and (c) The portion of radargram (highlighted in black in Fig. 6.3(a)) showing the detected positions of surface, layers and bedrock with horizontal lines. The closest trace to NEEM and a generic investigated trace are shown with vertical red and cyan lines, respectively.

(circles) and at the corrected depths (stars) are reported. It is worth noting the very high variability of the reflectivity profile and consequently the very different values of reflectivity obtained at the layer depths estimated with the two approaches. This analysis confirms the importance of calculating the depth based on the available DEP, rather than using the approximated value of $\varepsilon^{ice} = 3.15$. Besides the estimation of layer depth, another important aspect in the fusion of RS and DEP data is the approach to the estimation the layer reflectivity. The layer reflectivities reported qualitatively in Fig. 6.4(b) have been estimated by simply using (6.2). However, given the different vertical resolution of the RS and DEP data, a more complex analysis that takes into account the data resolution should be carried out. Indeed, a bright reflection in the radargram can be due to various interfaces in the DEP that lie within the radar resolution cell. As an example, we estimate the reflectivity of a layer as the mean value of the contributions coming from all interfaces in the DEP within the radar resolution cell (triangles in Fig. 6.4(b)). It is again worth to note the high variability in the estimated reflectivities with the three approaches (e.g., depending on the used approach, the cyan layer at about 1500m has estimated reflectivities in the range [-50 -80]dB). This high variability in the estimated layer reflectivity represents one of the main sources of uncertainty of the method.

In order to better understand the effects of the estimated reflectivity and to illustrate the preliminary results obtained by fusing the RS and DEP data, in the following we focus on a trace characterized by small-scale roughness (i.e., $\Phi < 0.3$, estimated as described in Sec. 6.2.2). The position of this trace is highlighted with a cyan star in Fig. 6.3(a) and with a cyan vertical line in Fig. 6.3(c). The vertical power profile and the positions of the layers on the investigated trace are shown in Fig. 6.5(a). Fig. 6.5(b) reports the estimated discrete power losses obtained with (6.6) as a function of corrected depth for the trace shown in Fig. 6.5(a). The power losses obtained with the reflectivity estimated from (6.2) are reported with stars in Fig. 6.5(b), whereas those obtained with the reflectivity estimated as the mean reflectivity value within the radar resolution cells are reported with triangles in Fig. 6.5(b). There are three main aspects worth to note by analyzing Fig. 6.5(b). First, the power losses estimated with the two approaches have different values and no sistematic trend over the whole ice column. Second, since in our definition the losses are a negative quantity (see (6.6)), the positive values of the estimated discrete power losses in the shallow subsurface (i.e., within the first 700m) are not reasonable from a physical point of view. We attribute these anomalous values to possible surface slope, aircraft roll (i.e.,$\approx 2^{\circ}$) and uncertainty in the reflectivity estimation from the DEP. Third, the power losses in the deep subsurface (i.e., below 1500m) appears to fluctuate around a mean value, instead of showing a decreasing trend, as expected due to increasing temperature towards the bedrock. This can be explained by the fact that the DEP profile is not

(a)

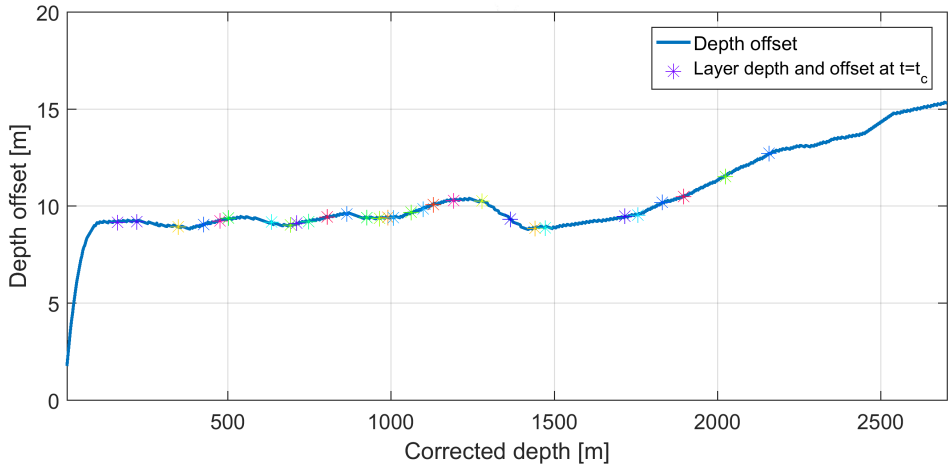

(b)

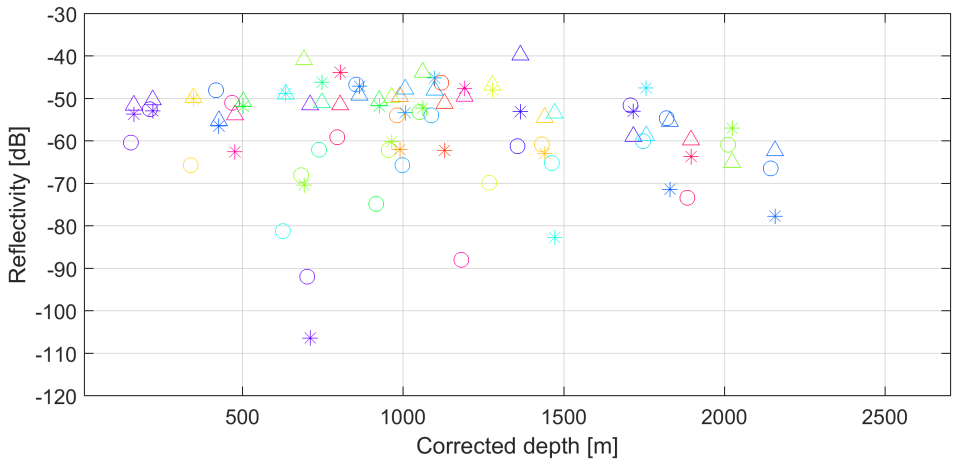

Figure 6.4: (a) Depth offset at the NEEM core site calculated as the difference between the depth estimated with the available DEP and the depth calculated assuming a constant dielectric permittivity $\varepsilon = 3.15$. As it can be seen, by assuming a constant dielectric permittivity of ice, the depth is underestimated along the whole ice column and the depth offset at the layer positions is in the range [8-13]m. (b) Estimated layer reflectivity; each different color refers to a different layer, whereas the different markers correspond to: 'o' - reflectivity computed with (6.2) at the approximated layer depth, '*' - reflectivity computed with (6.2) at the corrected layer depth, and '△' - reflectivity computed as the mean value of reflectivity inside the radar resolution cell centered at the corrected layer depth. Note the high variability in the estimated reflectivities with the three approaches (e.g., depending on the used approach, the violet layer at about 1500m has estimated reflectivities in the range [-80 -50]dB).

(a)

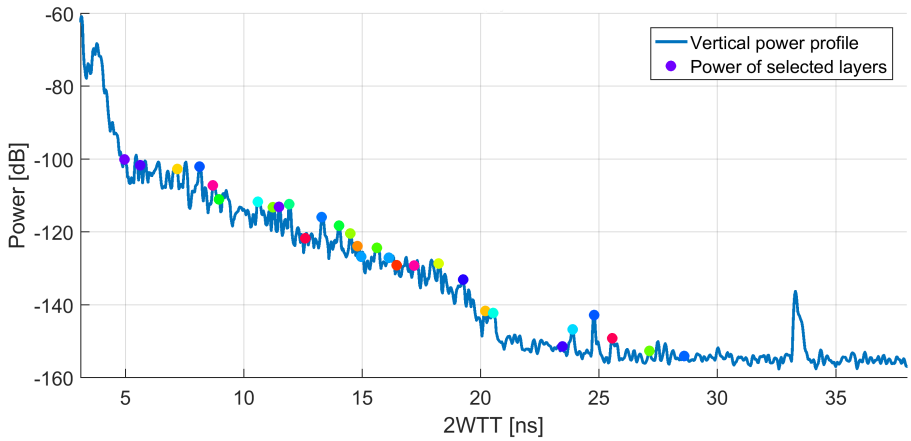

(b)

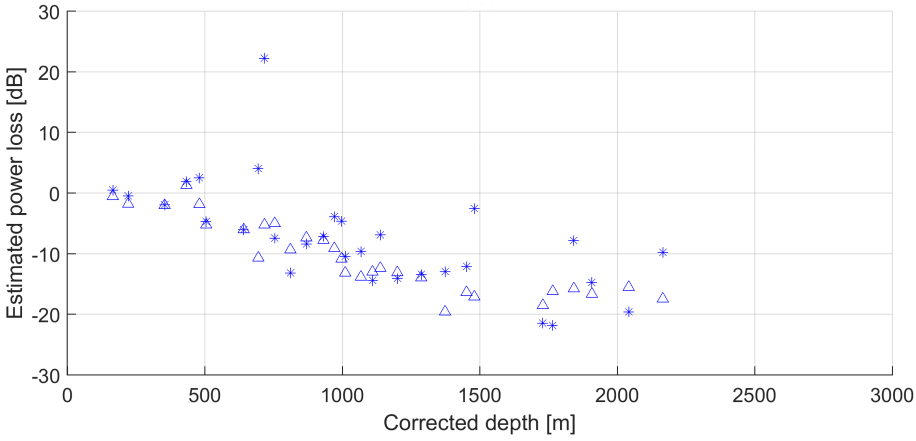

Figure 6.5: (a) Vertical profile of a generic trace (highlighted in cyan in Fig. 6.3(c)) as a function of 2WTT, and (b) Estimated discrete ice power losses as a function of corrected layer depths. The markers correspond to: '*' - ice power losses estimated on the basis of the reflectivity computed with (6.2) at the corrected layer depth, '△' - ice power losses estimated on the basis of the reflectivity computed as the mean value of reflectivity inside the radar resolution cell centered at the corrected layer depth. Note the high dependence of the estimated ice power losses on the estimated reflectivity values.

temperature corrected. The temperature correction can increase the layer reflectivity by several dBs [104], leading to estimated discrete power losses shifted downwards by a proportional amount.

The results obtained and reported for the generic trace shown in Fig. 6.5 should be considered as statistically representative for the portion of radargram shown in Fig. 6.3(c). This analysis proves that before going further into the estimation of ice power losses as a continuous function with depth, the available DEP should be temperature corrected and a stable and reliable approach should be defined and implemented for the estimation of layer reflectivity. Afterwards, the fitting performances of more non-linear functions should be investigated in order to infer the trend of power losses through the ice column and the power losses at the bedrock on the investigated traces.

6.4 Conclusion

This Chapter addressed the problem of understanding the radar wave interaction with the ice sheet. In particular, we have presented an automatic technique for the estimation of radar power losses through ice. The technique fuses RS and DEP ice core data and relies on a layer-driven approach which assumes that the layers visible in the radargram are dominated by specular reflections. As main advantages over other available techniques, the method aims to account for ice power losses due to rough surfaces, and to estimate the reflectivity and the depth of the layers visible in the radargram by properly fusing the RS data with the available DEP. This allows a more reliable estimation of power losses as a discrete function of layer depths and consequently enables a better estimation of the power losses as a continuous function with depth.

Preliminary results have been obtained by applying the technique to RS data acquired by MCoRDS and DEP data acquired at the NEEM ice core site in Greenland. In particular, we performed a sensitivity analysis on the calculation of the depth of the layers and corresponding reflectivity. We derived that depending on these factors, the discrete power losses estimated at the layer depths can have a very high variability, which can significantly affect the trend of any non-linear continuous fitting function. Thus, before analyzing the performance of such non-linear functions, a stable approach to the estimation of layer reflectivity should be defined and implemented. Such an approach should also take into account the temperature correction of the available DEP. Moreover, an analysis of the sensitivity of the method to other factors (i.e., aircraft attitude control, surface slope, number of layers) should be carried out. Afterwards, we will investigate the fitting perfomances of more ice temperature/physically constrained non-linear functions in order to understand both the global and the local trend of the ice attenuation. Finally,

we plan to apply the method to an extended dataset that covers a larger area of the ice sheet, or a more complex ice subsurface scenario in which the RS survey is closer to the border of the ice sheet, potentially both in Greenland and Antarctica.

Conclusions

This Chapter concludes the thesis by recalling the context of our research and by providing a summary of the novel contributions and a critical discussion of the related experimental results presented in the document. Finally, we provide ideas for future developments of the proposed methods.

Research context and summary of novel contributions

The impact of Cryosphere in the evolution of climate change requires enhanced studies of the ice sheets. Such studies are of great economical and societal importance, since they allow predictions of the future behavior of the global climate and an improved planning and use of available resources and technologies [105]. In this context, the aim of this thesis was to providing a contribution that can support the scientific community in the study of the ice sheet subsurface.

Radargrams acquired by radar sounder instruments operated on airborne platforms at the Earth polar regions and glaciated areas represent one of the most complete sources of information about the ice subsurface. Radargrams are georeferenced 2D profiles of the ice sheet that highlight the ice subsurface targets. Currently, there are huge archives of RS data collected during several airborne campaigns conducted at the ice sheets. Due to the wide coverage and different types of information that RS data convey (e.g., target reflected power, target position), the analysis of radargrams can lead to e great enhancement in the understanding of the ice sheets. However, during the past decades, the analysis of radargrams has been carried out mainly by means of manual investigation with limited support of semi-automated techniques. These approaches present several problems, e.g., the manual analysis is slow, intrinsically subjective and does not allow the fusion of different types of data (e.g., RS data, ALT data, ice core data). These issues suggest that the manual analysis limits the scientific return that could be potentially achieved by analysing the radargrams with more sophisticated approaches.

The importance of studying the ice sheets, the availability of large archives of airborne RS data, the expected increase in data volume from future RS missions, and the problems

raised by the manual analysis call for the development of novel automatic techniques for the analysis of radargrams. Although the automatic techniques present several advantages over the traditional manual approach, e.g., they are fast, objective and quantitative, and allow the joint integration of more types of data, so far the development of automatic techniques for the analysis of ice sheet RS data has been addressed only to a limited extent by the scientific community.

In this thesis we have provided four main novel contributions to fill the gap in the literature on the development of automatic techniques for the analysis of ice sheet RS data. In particular, the proposed methods are: 1) an automatic classification system and 2) an automatic detection technique of the ice subsurface targets, 3) an automatic method for the 3D reconstruction of the ice sheet, and 4) an automatic method for the estimation of radar power losses through ice. Such techniques address three challenges of great importance in the study of the ice sheets. In particular the first two methods regard the *identification of ice sheet subsurface targets*, the third method addresses the problem of *3D modeling of the ice sheet*, and the fourth method regards the *understanding the interaction between the radar wave and the ice sheet*.

In the first contribution of the thesis, we developed an automatic classification system of the ice subsurface targets typically present in radargrams, i.e., layers, bedrock and noise (including the EFZ). The system is made up of two main components: i) feature extraction and ii) automatic classification based on SVM. The main focus of the system is the extraction of informative features from the radargrams, useful for discriminating the samples belonging to the investigated targets. To this aim, we initially carried out a detailed study of the statistical properties of the radar signal and of the spatial distribution of the ice subsurface targets. Based on such a study, a set of seven features that model and correlate the backscattering properties of the radar signal with the spatial properties of the subsurface targets has been generated. Such features were then given as input to an automatic classifier based on SVM. The effectiveness of the proposed system, both in terms of computational efficiency, classification accuracy, and robustness to the spatial variability of the subsurface targets and heterogeneous quality of the data, has been proven on two real datasets of radargrams, with different characteristics, acquired by MCoRDS in two different regions in Antarctica. In particular, we obtained a classification accuracy greater than 97% on both datasets, which is satisfactory given the amount of data, the spatial variability of the subsurface in the investigated areas, and the fact that the system is almost completely automatic. In fact, the system requires a minimum amount of human interaction, only in the training phase of the classifier, in which the values of the few parameters are tuned to the characteristics of the data and the scale of the subsurface targets. On the other hand, after the training, the system is completely

automatic. Another advantage of the system is the fact that the algorithms composing it can be parallelized, leading to a reduced computational time, e.g., about 5 hours for the investigated datasets. Moreover, it is worth highlighting the flexibility and the learning capabilities of the system, e.g., depending on the radar frequency and resolution, different target classes with associated patterns can be identified in radargrams (e.g., high resolution data allows the identification of crevasses) and the system can be tuned to recognize them; one first needs to set the number of classes, appropriately model the properties of the classes in the feature extraction phase and then train the classifier to recognize such classes. Finally, the presented system can be easily tuned for analyzing different RS datasets, since it involves a small number of parameters in the overall classification algorithm, i.e., the dimension of the sliding window for the computation of the features and the value of the threshold used for extracting the relational feature.

In the second contribution of the thesis, we developed an unsupervised automatic technique for the detection and the estimation of ice subsurface target properties. The technique is based on a model of the ice sheet subsurface which assumes the presence of the EFZ. This is a reasonable assumption since several studies have confirmed the presence of the EFZ in extensive areas of the ice sheets. The technique relies on an algorithm for emphasizing the strong backscattering subsurface targets, and on an image segmentation algorithm for the detection of the borderlines of the ice surface, the last returns of the layers, and the first and last returns of the bedrock. This output combined with the parameters of the RS acquisition system help in estimating the properties of the subsurface targets, e.g., layered area thickness, bedrock scattering area, EFZ extension. The effectiveness of the proposed automatic detection technique has been proven on a real dataset acquired by MCoRDS in Antarctica. Satisfactory results have been obtained both quantitatively in terms of missed and false alarms, and qualitatively in terms of fitting perfomances of the detected borderlines to manually derived borders of the layers and bedrock areas.

As it can be seen, the two above-mentioned techniques regard the *identification of ice subsurface targets*. One common aspect of the proposed methods is their efficiency for the analysis of the ice subsurface at large scale. Also, both techniques rely on the analysis of the statistical properties of the radar signal. According to this analysis, in the investigated datasets the samples belonging to all target areas (i.e., layers, EFZ, bedrock, noise) follow a Gamma distribution. Moreover, the Gamma distributions of the EFZ and noise areas are very similar. This result confirms also from a statistical point of view the absence of targets in the EFZ, as hypothized and then demonstrated in the literature by analysing different types of subsurface data (e.g., RS, line-scan data, DEP). On the other hand, the main difference between the proposed methods is the flexibility and the

robustness of the automatic classification system to the variability of data. This is due to both the effectiveness of the extracted features and the employed learning approach. The automatic detection algorithm is conceptually simpler at the cost of less flexibility. In fact, the detection performance is ensured only if the assumption of EFZ existence holds for the entire along-track extension of the radargram. As a main advantage of the automatic detection algorithm, we recall the fact that, unlike the classification system, it is an unsupervised method, thus requiring very limited human intervention.

In the third contribution of the thesis, we developed an automatic technique for the local 3D reconstruction of the ice sheet. With respect to other works which regard the *3D modeling of the ice sheets*, the proposed method jointly uses RS and ALT data to estimate 3D maps of the ice surface, bedrock interface and ice thickness, with the highest overall quality and at the most reliable scale, derived and validated automatically given the input data. The method relies on the use of the OK method for interpolating the surface and bedrock elevation extracted from the RS data. The overall quality of interpolation is verified by investigating the uncertainty maps provided by the OK method, which is run with different parameter sets. The most reliable scale is identified by comparing interpolated surface elevation maps at different scales against consistently rescaled ALT data, considered as reference. Such scale is then used to interpolate the bedrock elevation samples, and finally to estimate the ice thickness by subtracting the estimated surface and bedrock elevation maps. The main contribution of this work with respect to the related literature is the joint use of the RS and ALT data for the optimization of the interpolation, the automatic identification of the most reliable scale, and the analysis and use of the uncertainty maps provided by the OK method. The proposed technique has been validated on a subset of RS data acquired by MCoRDS and ALT data acquired by the GLAS/ICESat instrument over a portion of the Byrd Glacier in Antarctica. The results obtained point out that the most reliable scale is at 1250m. This means that at 1250m, we obtained the lowest mean absolute error between the ice surface elevation map generated by interpolating the rescaled RS measurement with OK algorithm and the rescaled reference ALT data. Moreover, we obtained that at this scale the ice surface and bedrock interface are best represented by the Spherical and Exponential models, respectively. This confirms the higher variability in elevation of the bedrock samples with respect to the surface samples, which can be verified also qualitatively by inspecting the corresponding rescaled bedrock and surface elevation scatterplots in local neighborhoods. This analysis is very usefull for understanding the presence of complex scenarious in the subsurface, e.g., relevant bedrock topography. Also, the defined approach can be used for the 3D reconstruction of the ice internal layers or of the EFZ.

In the fourth and last contribution of the thesis, we developed an automatic technique

for the estimation of power losses through ice. This method regards the broad context of *understanding the interaction between the radar wave and the ice sheet*. With respect to other available works in the literature, which estimate the ice loss rate by assuming an approximated linear trend of the ice losses versus depth, the proposed technique aims to estimate the ice power losses as a continuous non-linear function of depth and location, accounting thus for temperature variations in the ice subsurface. The method fuses coincident RS and DEP ice core data and initially estimates the ice power losses as a discrete function of ice layer depth. Then, a theoretical continuous non-linear function is fitted to the discrete losses and extrapolated to the bedrock. The choice of the fitting function takes into account both the distribution of the estimated discrete losses in the depth-power domain and constraints imposed by available ice subsurface temperature models. This results in a more reliable estimation of the losses on wide areas, which is fundamental for a better understanding and modeling of the processes taking place within the ice sheet and at the basal interface. Although the method has been defined, at the moment of writing it has not been fully implemented and validated. However, the preliminary results obtained by applying the technique to real RS data and DEP core data acquired at the NEEM ice core in Greenland encourage further research. In particular, we performed a sensitivity analysis of the method to the estimation of layer depth and corresponding layer reflectivity. We derived that depending on these factors, the discrete power losses estimated at the layer depths can have a very high (e.g., even ≈30dB) variability, which can significantly affect the trend of any non-linear continuous fitting function. Thus, before analyzing the performance of such non-linear functions, a stable approach to the estimation of layer reflectivity should be defined and implemented. Such an approach should also take into account the temperature correction of the available DEP. Moreover, an analysis of the sensitivity of the method to other factors (i.e., aircraft attitude control, surface slope, number of layers) should be carried out. Only afterwards, the fitting performance of more ice temperature/physically constrained non-linear functions can be investigated in order to derive both the global and the local trend of the ice attenuation.

Concluding remarks and future developments

The studies and the methods along with the results described in this thesis regard the analysis of ice sheet RS data. The use of such techniques can become an efficient connection between two communities, i.e., the radar sounding and the glaciological community, which address the analysis of ice subsurface from different perspectives.

In particular, the first two proposed automatic methods for the identification of the ice subsurface targets, i.e., layers, bedrock, noise (including the EFZ), can be used for instance

in studies that can further focus on the interpretation of the detected layered area only, by applying other techniques for the identification of individual layers. Furthermore, the information about the EFZ onset in the radargrams can indicate changing archeology that shall be accounted for in the modeling of ice sheet dynamics. Also, one can analyze the shape of the EFZ for a better understanding of its formation. Finally, the identification of the whole bedrock backscattering area can be used in geological studies for assessing the type of material the bedrock is made of, or to understand the reasons for which the bedrock is thicker and thinner or it completely disappears at some coordinates. Moreover, the detection of the first return of the bedrock (i.e., the basal interface) helps estimating the bedrock topography, as done in the third method described in the thesis (i.e., the 3D reconstruction of the ice sheet subsurface), or inferring information about the basal conditions and processes, e.g., by using the fourth method described in the thesis (i.e., estimation of radar power losses through ice). The last return of the bedrock marks the depth below which the losses through the subsurface (ice and bedrock) have completely attenuated the trasmitted power. Thus it can be used to derive the absorption properties of the bedrock.

Future developments regarding the methods described in this thesis should address the following points:

- Definition of an approach to the unsupervised and adaptive selection of the parameters of the presented techniques and use of adaptive rather than rectangular windows for denoising and computation of features, for better taking into account the peculiarities of the data.
- Definition and extraction of more discriminative features for radargram classification and development of an appropriate postprocessing technique for removing the misclassified samples.
- Incorporation in the 3D reconstruction method of possible input data uncertainty values and modeling of possible anisotropic trends of the surfaces.
- Definition and implementation of a stable approach to the reliable estimation of layer reflectivity by fusing RS and DEP data, and consequently study of physically constrained models for ice power loss estimation and validation on larger and more complex datasets.
- Further tuning and validation of the proposed techniques by applying them to datasets with different characteristics, acquired both in Antarctica and Greenland.

List of Publications

Journal Papers

[1] Ilisei, A.-M. and Bruzzone, L. ,"A Model-Based Technique for the Automatic Detection of Earth Continental Ice Subsurface Targets in Radar Sounder Data," *IEEE Geoscience and Remote Sensing Letters*, vol. 11, no. 11, pp. 1911-1915, 2014.

[2] Ilisei, A.-M. and Bruzzone, L., "A System for the Automatic Classification of Ice Sheet Subsurface Targets in Radar Sounder Data," *IEEE Transactions on Geoscience and Remote Sensing*, vol. 53, no. 6, pp. 3260–3277, 2015.

[3] Ilisei, A.-M. and Bruzzone, L. ,"Automatic Local 3D Reconstruction of the Ice Sheet by Using Radar Sounder and Altimeter Data," *IEEE Transactions on Geoscience and Remote Sensing*, Submitted in February 2016.

International Conferences

[1] Ilisei, A.-M., Ferro, A. and Bruzzone, L., "A technique for the automatic estimation of ice thickness and bedrock properties in radar sounder data acquired at Antarctica," *Proceedings of the IEEE International Geoscience and Remote Sensing Symposium (IGARSS)*, 2012.

[2] Ilisei, A.-M. and Bruzzone, L., "Automatic classification of subsurface features in radar sounder data acquired in icy areas," *Proceedings of the IEEE International Geoscience and Remote Sensing Symposium (IGARSS)*, 2013.

[3] Ilisei, A.-M. and Bruzzone, L., "Integration of radar sounder and altimeter data for the 3D reconstruction of ice sheets," *Proceedings of the IEEE International Geoscience and Remote Sensing Symposium (IGARSS)*, 2015.

[4] Ilisei, A.-M. and Bruzzone, L., "Multiresolution fusion of radar sounder and altimeter data for the generation of high resolution DEMs of ice sheets," *Proceedings of SPIE, the International Society for Optical Engineering*, 2015.

[5] Bruzzone, L., Plaut, J., Alberti, G., Blankenship, D., Bovolo, F., Campbell, B., Castelletti, D., Gim, Y., Ilisei, A. M., Kofman, W., Komatsu, G., Mckinnon, W., Mitri, G., Moussessian, A., Notarnicola, C., Orosei, R., Patterson, G. W., Pettinelli, E., and Plettemeier, D., "Jupiter ICY moon explorer (JUICE): Advances in the design of the Radar for Icy Moons (RIME)," *Proceedings of the IEEE International Geoscience and Remote Sensing Symposium (IGARSS)*, 2015.

[6] Bruzzone, L., Plaut, J., Alberti, G., Blankenship, D., Bovolo, F., Campbell, B., Castelletti, D., Gim, Y., Ilisei, A. M., Kofman, W., Komatsu, G., Mckinnon, W., Mitri, G., Moussessian, A., Notarnicola, C., Orosei, R., Patterson, G. W., Pettinelli, E., and Plettemeier, D., " The Radar for Icy Moon Exploration (RIME) on the JUICE mission," *American Geophysical Union (AGU) Fall Meeting*, 2015.

[7] Ilisei, A.-M., Li, J., Gogineni, S., and Bruzzone, L., "Estimation of Radar Power Losses in Ice by Using Radar Sounder and Ice Core Data," *Proceedings of SPIE, the International Society for Optical Engineering*, Submitted in April 2016.

Acknowledgements

Bibliography

[1] J. Li, J. Paden, C. Leuschen, F. Rodriguez-Morales, R. Hale, E. Arnold, R. Crowe, D. Gomez-Garcia, and P. Gogineni, "High-altitude radar measurements of ice thickness over the Antarctic and Greenland ice sheets as a part of Operation IceBridge," *IEEE Transactions on Geoscience and Remote Sensing*, vol. 51, no. 2, pp. 742–754, 2013.

[2] "Cryosphere and climate," http://www.wcrp-climate.org/cryosphere-climate.

[3] V. Bogorodsky, C. Bentley, and P. Gudmandsen, *Radioglaciology*, D. H. D. Reidel Publishing Company, Ed., 1984.

[4] T. Ono, A. Kumamoto, Y. Yamaguchi, A. Yamaji, T. Kobayashi, Y. Kasahara, and H. Oya, "Instrumentation and observation target of the Lunar Radar Sounder (LRS) experiment on-board the SELENE spacecraft," *Earth, Planets, Space*, vol. 60, pp. 321–332, 2008.

[5] R. Seu, R. Phillips, D. Biccari, R. Orosei, M. A., G. Picardi, A. Safaeinili, B. Campbell, J. Plaut, L. Marinangeli, S. Smrekar, and D. Nunes, "SHARAD sounding radar on the Mars Reconnaissance Orbiter," *J. Geophys. Res.*, vol. 112, 2007.

[6] R. Jordan et al., "The Mars Express MARSIS sounder instrument," *Planetary and Space Science*, vol. 57, pp. 1975–1986, 2009.

[7] L. Bruzzone, J. Plaut, G. Alberti, D. Blankenship, F. Bovolo, B. Campbell, D. Castelletti, Y. Gim, A.-M. Ilisei, W. Kofman, G. Komatsu, W. McKinnon, G. Mitri, A. Moussessian, C. Notarnicola, R. Orosei, G. Patterson, E. Pettinelli, and D. Plettemeier, "JUpiter ICy moon explorer (juice): Advances in the design of the radar for Icy Moons (RIME)," in *IEEE International Geoscience and Remote Sensing Symposium (IGARSS)*, 2015, pp. 1257–1260.

[8] P. Baüer et al., "MIMOSA: Mapping of antarctic Ice and Monitoring of SubArctic," 1998, proposal for Earth Opportuniy Mission ESA AO.

[9] A. Herique, W. Kofman, P. Baüer, F. Remy, and L. Phalippou, "A spaceborne ground penetrating radar: MIMOSA," in *IEEE International Geoscience and Remote Sensing Symposium (IGARSS)*, vol. 1, 1999, pp. 473–475.

[10] L. Bruzzone et al., "*GLACiers and Icy Environments Sounding*," 2010, proposal to ESA Earth Explorer Call.

[11] C. Oliver and S. Quegan, "*Understanding Synthetic Aperture Radar Images*," *SciTech Publishing*, 2004.

[12] I. Cumming and F. Wong, *Digital Processing of Synthetic Aperture Radar Data: Algorithms and Implementation*, ser. Artech House remote sensing library. Artech House, 2005, no. v. 1.

[13] A. Ferro, A. Pascal, and L. Bruzzone, "A novel technique for the automatic detection of surface clutter returns in radar sounder data," *IEEE Transactions on Geoscience and Remote Sensing*, vol. 51, no. 5, pp. 3037–3055, May 2013.

[14] F. Rodriguez-Morales, S. Gogineni, C. Leuschen, J. Paden, J. Li, C. Lewis, B. Panzer, D. Gomez-Garcia Alvestegui, A. Patel, K. Byers, R. Crowe, K. Player, R. Hale, E. Arnold, L. Smith, C. Gifford, D. Braaten, and C. Panton, "Advanced multifrequency radar instrumentation for polar research," *IEEE Transactions on Geoscience and Remote Sensing*, vol. 52, no. 5, pp. 2824–2842, 2014.

[15] M. Peters, D. Blankenship, S. Carter, S. Kempf, D. Young, and J. Holt, "Along-track focusing of airborne radar sounding data from West Antarctica for improving basal reflection analysis and layer detection," *IEEE Transactions on Geoscience and Remote Sensing*, vol. 45, no. 9, pp. 2725–2736, 2007.

[16] C. Hernandez, V. Krozer, J. Vidkjaer, and J. Dall, "POLARIS: ESA's airborne ice sounding radar front-end design, performance assessment and first results," in *IEEE MTT-S International Microwave Symposium Digest*, 2009, pp. 393–396.

[17] A. Buis, "NASA Mars Research Helps Find Buried Water on Earth," http://www.nasa.gov/topics/earth/features/kuwait20110914.html, 2011.

[18] J. Dall, "Ice sheet anisotropy measured with polarimetric ice sounding radar," in *IEEE International Geoscience and Remote Sensing Symposium (IGARSS)*, 2010, pp. 2507–2510.

[19] C. Gifford, G. Finyom, M. Jefferson, M. Reid, E. Akers, and A. Agah, "Automated polar ice thickness estimation from radar imagery," *IEEE Transactions on Image Processing*, vol. 19, no. 9, pp. 2456–2469, 2010.

[20] N. Karlsson, D. Dahl-Jensen, P. Gogineni, and J. Paden, "Tracing the depth of the Holocene ice in North Greenland from radio-echo sounding data," *Annals of Glaciology*, vol. 54, no. 64, pp. 44–50, 2013.

[21] O. Eisen, "Inference of velocity pattern from isochronous layers in firn, using an inverse method," *Journal of Glaciology*, vol. 54, no. 187, pp. 613–630, 2008.

[22] E. Waddington, T. Neumann, M. Koutnik, H. Marshall, and D. Morse, "Inference of accumulation-rate patterns from deep layers in glaciers and ice sheets," *Journal of Glaciology*, vol. 53, no. 183, pp. 694–712, 2007.

[23] D. Crandall, G. Fox, and J. Paden, "Layer-finding in radar echograms using probabilistic graphical models," in *21st International Conference on Pattern Recognition (ICPR)*, 2012, pp. 1530–1533.

[24] L. Sime, R. Hindmarsh, and H. Corr, "Instruments and Methods Automated processing to derive dip angles of englacial radar reflectors in ice sheets," *Journal of Glaciology*, vol. 57, no. 202, pp. 260–266(7), 2011.

[25] "A semi-automatic approach for estimating near surface internal layers from snow radar imagery," in *IEEE International Geoscience and Remote Sensing Symposium (IGARSS)*, 2013.

[26] J. MacGregor, M. Fahnestock, G. Catania, J. Paden, S. Gogineni, S. K. Young, S. Rybarski, A. Mabrey, B. Wagman, and M. Morlighem, "Radiostratigraphy and age structure of the Greenland Ice Sheet," *Journal of Geophysical Research: Earth Surface*, vol. 120, no. 2, pp. 212–241, 2015.

[27] C. Panton, "Automated mapping of local layer slope and tracing of internal layers in radio echograms," *Annals of Glaciology*, vol. 55, no. 67, pp. 71–77, 2014.

[28] C. Gifford and A. Agah, "Subglacial water presence classification from polar radar data," *Engineering Applications of Artificial Intelligence*, vol. 25, no. 4, pp. 853–868, 2012.

[29] G. Oswald and S. Gogineni, "Recovery of subglacial water extent from Greenland radar survey data," *Journal of Glaciology*, vol. 54, no. 184, pp. 94–106, 2008.

[30] R. Drews, "Layer disturbances and the radio-echo free zone in ice sheets," *The Cryosphere*, vol. 3, no. 2, pp. 195–203, 2009.

[31] G. Freeman, A. Bovik, and J. Holt, "Automated detection of near surface Martian ice layers in orbital radar data," in *IEEE Southwest Symposium on Image Analysis Interpretation (SSIAI)*, 2010, pp. 117–120.

[32] A. Ferro and L. Bruzzone, "Automatic extraction and analysis of ice layering in radar sounder data," *IEEE Transactions on Geoscience and Remote Sensing*, vol. 51, no. 3, pp. 1622–1634, 2013.

[33] A. Ferro and L. Bruzzone, "Analysis of radar sounder signals for the automatic detection and characterization of subsurface features," *IEEE Transactions on Geoscience and Remote Sensing*, vol. 50, no. 11, pp. 4333–4348, 2012.

[34] S. Delbo, P. Gamba, and D. Roccato, "A fuzzy shell clustering approach to recognize hyperbolic signatures in subsurface radar images," *IEEE Transactions on Geoscience and Remote Sensing*, vol. 38, no. 3, pp. 1447–1451, 2000.

[35] P. Gamba and S. Lossani, "Neural detection of pipe signatures in ground penetrating radar images," *IEEE Transactions on Geoscience and Remote Sensing*, vol. 38, no. 2, pp. 790–797, 2000.

[36] H. Youn and C. Chen, "Automatic GPR target detection and clutter reduction using neural network," *Proc. SPIE 4758, Ninth International Conference on Ground Penetrating Radar*, pp. 579–582, 2002.

[37] P. Gamba and V. Belotti, "Two fast buried pipe detection schemes in Ground Penetrating Radar images," *International Journal of Remote Sensing*, vol. 24, no. 12, pp. 2467–2484, 2003.

[38] E. Pasolli, F. Melgani, and M. Donelli, "Automatic analysis of GPR images: A pattern-recognition approach," *IEEE Transactions on Geoscience and Remote Sensing*, vol. 47, no. 7, pp. 2206–2217, 2009.

[39] M. Lythe and D. Vaughan, "BEDMAP: A new ice thickness and subglacial topographic model of Antarctica," *Journal of Geophysical Research: Solid Earth*, vol. 106, no. B6, pp. 11 335–11 351, 2001.

[40] P. Fretwell et al., "Bedmap2: improved ice bed, surface and thickness datasets for Antarctica," *The Cryosphere*, vol. 7, no. 1, pp. 375–393, 2013.

[41] J. Bamber, "A new ice thickness and bed data set for the Greenland ice sheet 1. Measurement, data reduction, and errors," *J. Geophys. Res*, vol. 106, no. 33, pp. 773–33, 2001.

[42] J. Bamber, J. Griggs, R. Hurkmans, J. Dowdeswell, S. Gogineni, I. Howat, J. Mouginot, J. Paden, S. Palmer, E. Rignot, and D. Steinhage, "A new bed elevation dataset for Greenland," *The Cryosphere*, vol. 7, no. 2, pp. 499–510, 2013.

[43] s. Gogineni, J. Yan, J. Paden, C. Leuschen, J. Li, F. Rodriguez-Morales, D. Braaten, K. Purdon, Z. Wang, W. Liu, and J. Gauch, "Bed topography of Jakobshavn Isbrae, Greenland, and Byrd glacier, Antarctica," *Journal of Glaciology*, vol. 60, no. 223, pp. 813–833, 2014.

[44] M. Huss and D. Farinotti, "Distributed ice thickness and volume of all glaciers around the globe," *Journal of Geophysical Research: Earth Surface (2003-2012)*, vol. 117, no. F4, 2012.

[45] M. Huss and D. Farinotti, "A high-resolution bedrock map for the Antarctic Peninsula," *The Cryosphere*, vol. 8, no. 4, pp. 1261–1273, 2014.

[46] J. Roberts, R. Warner, D. Young, A. Wright, T. van Ommen, D. Blankenship, M. Siegert, N. Young, I. Tabacco, A. Forieri, A. Passerini, A. Zirizzotti, and M. Frezzotti, "Refined broad-scale sub-glacial morphology of Aurora Subglacial Basin, East Antarctica derived by an ice-dynamics-based interpolation scheme," *The Cryosphere*, vol. 5, no. 3, pp. 551–560, 2011.

[47] R. Warner and W. Budd, "Derivation of ice thickness and bedrock topography in data-gap regions over Antarctica," *Annals of Glaciology*, vol. 31, no. 1, pp. 191–197, 2000.

[48] D. Rippin, J. Bamber, M. Siegert, D. Vaughan, and H. Corr, "Basal topography and ice flow in the Bailey/Slessor region of East Antarctica," *Journal of Geophysical Research: Earth Surface*, vol. 108, no. F1, 2003.

[49] M. Morlighem, E. Rignot, H. Seroussi, E. Larour, H. Ben Dhia, and D. Aubry, "A mass conservation approach for mapping glacier ice thickness," *Geophysical Research Letters*, vol. 38, no. 19, 2011.

[50] M. Morlighem, E. Rignot, J. Mouginot, H. Seroussi, and E. Larour, "High-resolution ice-thickness mapping in South Greenland," *Annals of Glaciology*, vol. 55, no. 67, pp. 64–70, 2014.

[51] A. Gades, C. Raymond, H. Conway, and R. Jacobel, "Bed properties of Siple Dome and adjacent ice streams, West Antarctica, inferred from radio-echo sounding measurements," *Journal of Glaciology*, vol. 46, no. 152, pp. 88–94, 2000.

[52] D. Winebrenner, B. Smith, G. Catania, H. Conway, and C. Raymond, "Radio-frequency attenuation beneath Siple dome, West Antarctica, from wide-angle and profiling radar observations," *Annals of Glaciology*, vol. 37, no. 1, pp. 226–232, 2003.

[53] J. MacGregor, D. Winebrenner, H. Conway, K. Matsuoka, P. Mayewski, and G. Clow, "Modeling englacial radar attenuation at Siple Dome, West Antarctica, using ice chemistry and temperature data," *Journal of Geophysical Research: Earth Surface*, vol. 112, no. F3, 2007.

[54] R. Jacobel, B. Welch, D. Osterhouse, R. Pettersson, and J. MacGregor, "Spatial variation of radar-derived basal conditions on Kamb Ice Stream, West Antarctica," *Annals of Glaciology*, vol. 50, no. 51, pp. 10–16, 2009.

[55] C. Schroeder, D. Grima and D. Blankenship, "Evidence for variable grounding-zone and shear-margin basal conditions across Thwaites Glacier, West Antarctica," *Geophysics*, vol. 81, no. 1, pp. WA35–WA43, 2015.

[56] T. Jordan, J. Bamber, C. Williams, J. Paden, M. Siegert, P. Huybrechts, O. Gagliardini, and F. Gillet-Chaulet, "An ice-sheet wide framework for englacial attenuation and basal reflection from ice penetrating radar data," *The Cryosphere Discussions*, vol. 2016, pp. 1–37, 2016.

[57] G. Robin, S. Evans, and J. Bailey, "Interpretation of radio echo sounding in polar ice sheets," *Philosophical Transactions of the Royal Society of London. Series A, Mathematical and Physical Sciences*, vol. 265, no. 1166, pp. 437–505, 1969.

[58] W. Miners, E. Wolff, J. Moore, R. Jacobel, and L. Hempel, "Modeling the radio echo reflections inside the ice sheet at Summit, Greenland," *Journal of Geophysical Research: Solid Earth*, vol. 107, no. B8, 2002.

[59] J. MacGregor, J. Li, J. Paden, G. Catania, G. Clow, M. Fahnestock, S. Gogineni, R. Grimm, M. Morlighem, S. Nandi, H. Seroussi, and D. Stillman, "Radar attenuation and temperature within the Greenland Ice Sheet," *Journal of Geophysical Research: Earth Surface*, vol. 120, no. 6, pp. 983–1008, 2015.

[60] K. Matsuoka, D. Morse, and C. Raymond, *Journal of Geophysical Research: Earth Surface*, vol. 115, no. F2, 2010.

[61] A.-M. Ilisei and L. Bruzzone, "A system for the automatic classification of ice sheet subsurface targets in radar sounder data," *IEEE Transactions on Geoscience and Remote Sensing*, vol. 53, no. 6, pp. 3260–3277, 2015.

[62] P. Gogineni, "CReSIS Radar Depth Sounder Data," http://data.cresis.ku.edu/, 2012, Digital Media., Lawrence, Kansas, USA.

[63] CReSIS, https://data.cresis.ku.edu/data/rds/2010_Antarctica_DC8/CSARP_mvdr/20101104_06/, 2011.

[64] CReSIS, https://data.cresis.ku.edu/data/rds/2011_Antarctica_TO/CSARP_mvdr/, 2013.

[65] K. Matsuoka, J. MacGregor, and F. Pattyn, "Predicting radar attenuation within the Antarctic ice sheet," *Earth and Planetary Science Letters*, vol. 359, pp. 173–183, 2012.

[66] S. Fujita, H. Maeno, S. Uratsuka, T. Furukawa, S. Mae, Y. Fujii, and O. Watanabe, "Nature of radio echo layering in the antarctic ice sheet detected by a two-frequency experiment," *J. Geophys. Res., 104(B6)*, pp. 13 013–13 024, 1999.

[67] D. Millar, "Radio-echo layering in polar ice sheets and past volcanic activity," *Nature*, no. 5822, pp. 441–443, 1981.

[68] E. Rignot, J. Mouginot, and B. Scheuchl, "Ice flow of the Antarctic Ice Sheet," *Science*, vol. 333, no. 6048, pp. 1427–1430, 2011.

[69] P. Nienow and B. Hubbard, *Surface and Englacial Drainage of Glaciers and Ice Sheets*. John Wiley and Sons, 2005, vol. 4, pp. 2575–2586.

[70] G. Robin and D. Millar, "Flow of ice sheets in the vicinity of subglacial peaks," *Annals of GLacioLogy*, vol. 3, pp. 290–294, 1982.

[71] K. Matsuoka, T. Furukawa, S. Fujita, H. Maeno, S. Uratsuka, R. Naruse, and O. Watanabe, "Crystal orientation fabrics within the Antarctic ice sheet revealed by a multipolarization plane and dual-frequency radar survey," *J. Geophys. Res.*, vol. 108, no. B10, 2003.

[72] R. Bell, F. Ferraccioli, T. Creyts, D. Braaten, H. Corr, I. Das, D. Damaske, N. Frearson, T. Jordan, K. Rose, and M. Studinger, M.and Wolovick, "Widespread persistent thickening of the East Antarctic Ice Sheet by freezing from the base," *Science*, vol. 331, no. 6024, pp. 1592–1595, 2011.

[73] M. Siegert, "Antarctic subglacial lakes," *Earth-Science Reviews*, vol. 50, pp. 29–50, 2000.

[74] D. Daniels, *Ground Penetrating Radar, 2nd Edition*, ser. Ground Penetrating Radar. Institution of Engineering and Technology, 2004, vol. 1.

[75] C. Forbes, M. Evans, N. Hastings, and B. Peacock, *Multivariate Distributions*. John Wiley and Sons, Inc., 2010.

[76] J. Lin, "Divergence measures based on the Shannon entropy," *IEEE Transactions on Information Theory*, vol. 37, no. 1, pp. 145–151, 1991.

[77] S. Moysey, R. Knight, and H. Jol, "Texture-based classification of ground-penetrating radar images," *Geophysics*, vol. 71, no. 6, pp. K111–K118, 2006.

[78] T. Algra, "Compression of raw SAR data using entropy-constrained quantization," in *IEEE International Geoscience and Remote Sensing Symposium*, vol. 6, 2000, pp. 2660–2662.

[79] C. Cortes and V. Vapnik, "Support-vector networks," in *Machine Learning*, 1995, pp. 273–297.

[80] G. Camps-Valls and L. Bruzzone, *Kernel Methods for Remote Sensing Data Analysis*. John Wiley and Sons, Inc, 2009.

[81] L. Bottou, C. Cortes, J. Denker, H. Drucker, I. Guyon, L. Jackel, Y. LeCun, U. Muller, E. Sackinger, P. Simard, and V. Vapnik, "Comparison of classifier methods: a case study in handwritten digit recognition," in *Conference on Pattern Recognition, 1994. Vol. 2 - Conference B: Computer Vision amp; Image Processing, Proceedings of the 12th IAPR International*, vol. 2, 1994, pp. 77–82.

[82] U. Kressel, "Advances in kernel methods," B. Scholkopf, C. J. C. Burges, and A. J. Smola, Eds. MIT Press, 1999, ch. Pairwise Classification and Support Vector Machines, pp. 255–268.

[83] A. Ben-Hur and J. Weston, "A users guide to support vector machines," Tech. Rep., 2012.

[84] CReSIS, ftp://ftp.cresis.ku.edu/data/rds/rds_readme.pdf, 2013.

[85] R. Congalton, "A review of assessing the accuracy of classifications of remotely sensed data," *Remote sensing of environment*, vol. 37, no. 1, pp. 35–46, 1991.

[86] I. Tsang, J. Kwok, P. Cheung, and N. Cristianini, "Core vector machines: Fast SVM training on very large data sets." *Journal of Machine Learning Research*, vol. 6, no. 4, 2005.

[87] J. Greenwood and D. Durand, "Aids for fitting the gamma distribution by maximum likelihood," *Technometrics*, 1960.

[88] A.-M. Ilisei and L. Bruzzone, "A model-based technique for the automatic detection of Earth continental ice subsurface targets in radar sounder data," *IEEE Geoscience and Remote Sensing Letters (GRSL)*, vol. 11, no. 11, pp. 1911–1915, 2014.

[89] A.-M. Ilisei and L. Bruzzone, "Automatic local 3D reconstruction of the ice sheet by using radar sounder and altimeter data," 2016, in review since February 2016.

[90] N. Cressie, *Statistics for spatial data*. Wiley series in probability and mathematical statistics. J. Wiley & Sons, 1993.

[91] J. DiMarzio, "GLAS/ICESat 500m Laser Atimetry Digital Elevation Model of Antarctica," 2007.

[92] D. Wehner, *High-resolution Radar*, ser. Artech House radar library. Artech House, 1995.

[93] M. Skolnik, *Radar Handbook, Third Edition*. McGraw-Hill Education, 2008.

[94] G. Bohling, "Introduction to geostatistics and variogram analysis," 2005.

[95] S. Vieira, R. Carvalho, M. Ceddia, and A. Gonzalez, "Detrending non stationary data for geostatistical applications," *Bragantia*, vol. 69, pp. 1 – 8, 2010.

[96] N. Cressie, "Fitting variogram models by weighted least squares," *Journal of the International Association for Mathematical Geology*, vol. 17, no. 5, pp. 563–586, 1985.

[97] X. Zhang, J. Van Eijkeren, and A. Heemink, "On the weighted least-squares method for fitting a semivariogram model," *Computers and Geosciences*, vol. 21, pp. 605–608, 1995.

[98] R. Keys, "Cubic convolution interpolation for digital image processing," *IEEE Transactions on Acoustics, Speech and Signal Processing*, vol. 29, no. 6, pp. 1153–1160, 1981.

[99] T. Hastie, R. Tibshirani, and J. Friedman, *The Elements of Statistical Learning: Data Mining, Inference, and Prediction*. Springer New York, 2013.

[100] C. Matzler and U. Wegmuller, "Dielectric properties of freshwater ice at microwave frequencies," *Journal of Physics D: Applied Physics*, vol. 20, no. 12, p. 1623, 1987.

[101] M. Peters, D. Blankenship, and D. Morse, "Analysis techniques for coherent airborne radar sounding: Application to West Antarctic ice streams," *Journal of Geophysical Research: Oceans*, vol. 110, no. 6, pp. 1–17, 2005.

[102] C. Neal, "Radio echo determination of basal roughness characteristics on the Ross Ice Shelf," *Annals of Glaciology*, vol. 3, pp. 216–221, 1982.

[103] S. Rasmussen et al., "A first chronology for the North Greenland Eemian Ice Drilling (NEEM) ice core," *Climate of the Past*, vol. 9, no. 6, pp. 2713–2730, 2013.

[104] G. Paren and G. Robin, "Internal reflections in polar ice sheets," *Journal of Glaciology*, vol. 14, no. 71, 1975.

[105] N. Stern, *Stern Review: The economics of climate change*. HM treasury, 2006, vol. 30.